Low Frequency Electric Field Imaging

by

Hugh E. Chung

A Dissertation Presented in Partial Fulfillment
of the Requirements for the Degree
Doctor of Philosophy

Defended July 2017 by the
Graduate Supervisor Committee:

David Allee, Chair
Douglas Cochran
James Aberle
Stephen Phillips

ARIZONA STATE UNIVERSITY

August 2017

ABSTRACT

Electric field imaging allows for a low cost, compact, non-invasive, non-ionizing alternative to other methods of imaging. It has many promising industrial applications including security, safely imaging power lines at construction sites, finding sources of electromagnetic interference, geo-prospecting, and medical imaging. The work presented in this dissertation concerns low frequency electric field imaging: the physics, hardware, and various methods of achieving it.

Electric fields have historically been notoriously difficult to work with due to how intrinsically noisy the data is in electric field sensors. As a first contribution, an in-depth study demonstrates just how prevalent electric field noise is. In field tests, various cables were placed underneath power lines. Despite being shielded, the 60 Hz power line signal readily penetrated several types of cables.

The challenges of high noise levels were largely addressed by connecting the output of an electric field sensor to a lock-in amplifier. Using the more accurate means of collecting electric field data, D-dot sensors were arrayed in a compact grid to resolve electric field images as a second contribution. This imager has successfully captured electric field images of live concealed wires and electromagnetic interference.

An active method was developed as a third contribution. In this method, distortions created by objects when placed in a known electric field are read. This expands the domain of what can be imaged because the object does not need to be a time-varying electric field source. Images of dielectrics (e.g. bodies of water) and DC wires were captured using this new method.

The final contribution uses a collection of one-dimensional electric field images, i.e. projections, to reconstruct a two-dimensional image. This was achieved using algorithms based in computed tomography such as filtered backprojection. An algebraic approach was also used to enforce sparsity regularization with the L1 norm, further improving the quality of some images.

ACKNOWLEDGMENTS

First and foremost, I would like to thank my principal investigator, Dr. David Allee. None of this would have been possible without his mentorship which started when I was just a sophomore undergraduate. His passion for his work has truly been an inspiration for me in my research. I would also like to thank my committee members Drs. Douglas Cochran, James Aberle, and Stephen Phillips for their guidance in this dissertation.

I would like to thank my colleagues George Kunnen, Joseph Smith, and Zachary Drummond for helping me develop into the researcher I am today. Special thanks to the engineering team at the Flexible Electronics and Display Center, particularly John Stowell and Steve Rednour, for all their contributions.

A lot of heavy lifting and lab measurements were also accomplished thanks in no small part to the many seniors who did their capstone projects through the lab: Weidong Ye, Sandeep Vora, Keegan Scowen, Jake Sciacca, Alex Lucas, Anthony Wilson, John Gorrie, Clementina Reynolds, Matt Oman, Michael McMaster, Angelo Delluomo, Oscar Vasquez, Alvin Su, Mitchell Cook, Tyler Angell, and Richard Lin.

I would also like to thank our sponsors at the Army Research Lab, particularly David Hull and Stephen Vinci, under the Cooperative Agreement W911NG-04-2-0005 and the FlexTech Alliance under contract RFP14-170 for funding this research.

Last, and certainly not least, I would like to thank my friends and most importantly my family. Thank you to Eugene Chung, my little (though taller) brother, who has always kept me grounded and my loving mom and dad, Min and Young Chung, for their unconditional love and support.

TABLE OF CONTENTS

Page

CHAPTER Page

CHAPTER Page

CHAPTER Page

LIST OF TABLES

LIST OF FIGURES

Figure Page

Figure Page

Figure Page

Figure Page

Figure Page

Figure Page

Figure Page

Chapter 1

INTRODUCTION

1.1 Background

The ability to measure electric fields is invaluable in a world becoming ever more dependent on electronic devices. It already constitutes a multi-trillion-dollar industry that has grown at an average rate of 12.6% per year [1] and is projected to steadily grow [2], [3]. Electric field sensing has many advantages including its low cost, compact size, high sensitivity, non-contact form factor, and ability to penetrate non-conducting materials [4], [5], making it prevalent in a wide array of commercial and industrial applications.

Even in nature, species such as *Eigenmannia virescens* and *Mormyriformes* have a sixth sense through detecting electric fields [6]. These species of fish use electric fields as a form of vision in the dark and murky waters they reside in by using their tail as a current source to induce a voltage. They then electrolocate nearby objects which have a different conductivity from that of the surrounding water [6], [7], [8], Figure 1. Elasmobranchs (sharks, skates, and rays) have also been shown to detect electric fields with an ability known as electroreception. Some sharks have proven to detect electric fields as small as 5 nV/cm, rivaling the capabilities of some premier physics laboratories [9]. They use this ability to locate food and mates which each generate unique electric field signatures based off their body structure and swimming mechanisms [10].

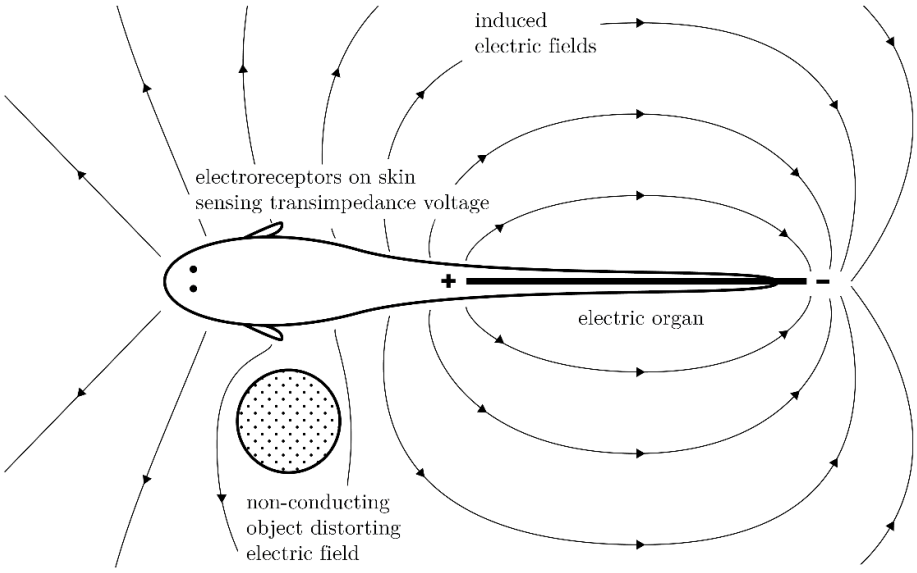

Figure 1: Diagram of a fish using electric field sensing to locate a dielectric object.

Despite the many benefits, electric fields have notoriously been finicky and difficult to measure accurately. This is partly because electric fields are omnipresent and exhibit significant fringing, adding high levels of non-linearity to any models and calculations. For this reason, electric field sensing is often relegated to binary-like, detection applications or problems with very well-defined boundary conditions.

1.2 Current Applications for Electric Field Sensing

Electric field proximity sensors are the most proliferate and are used in automobiles for proper airbag deployment [11], robotics for vision [7], [12], and home automation. Not only does proximity sensing with electric fields provide a cost-effective solution to novel and more intuitive interfaces [13], [14], it also allows greater power savings as devices can

rest in sleep mode until a human user presence is detected [15]. Capacitive sensing is a similar derivative which also utilizes electric fields [16].

Electric field sensors have also been used to sense conductive properties of objects. These include salinity sensors which measure the increase in conductivity as salt levels rise [17] and sensors which are integrated into robotic arms at recycling centers to automatically ensure plastic bottles do not contain water before disposal [18].

Medical imaging techniques have used electric fields such as electrical impedance tomography (EIT) [6], [19] and electroencephalogram/electrocardiogram (EEG/ECG) sensors [20]. In EIT a ring of electrodes is wrapped around a body part, and a current is applied between pairs of electrodes to measure the resulting voltages. Tomographic algorithms then reconstruct a cross-sectional image of the impedance map. EEG/ECGs use compact electric field sensors integrated with amplification, bandpass, and analog-to-digital stages to capacitively couple with the skin to non-invasively produce signals of brain and heart activity, respectively.

Very large-scale applications have also proven to be appropriate for electric field sensing such as the mature practice of geophysical prospecting [6], [21]. To locate large deposits of oil and ore in the earth's crust, prospectors first place two driving electrodes into the ground at a relatively far distance to establish a voltage difference. Two closely placed sensing electrodes are read along the line of the two driving electrodes to form a voltage gradient map based off known measurements of the earth's resistivity, Figure 2. Deviations from the uniform gradient are then indicators of deposits and reservoirs. An alternative method applies a voltage on a probe lowered into an oil well to measure the current.

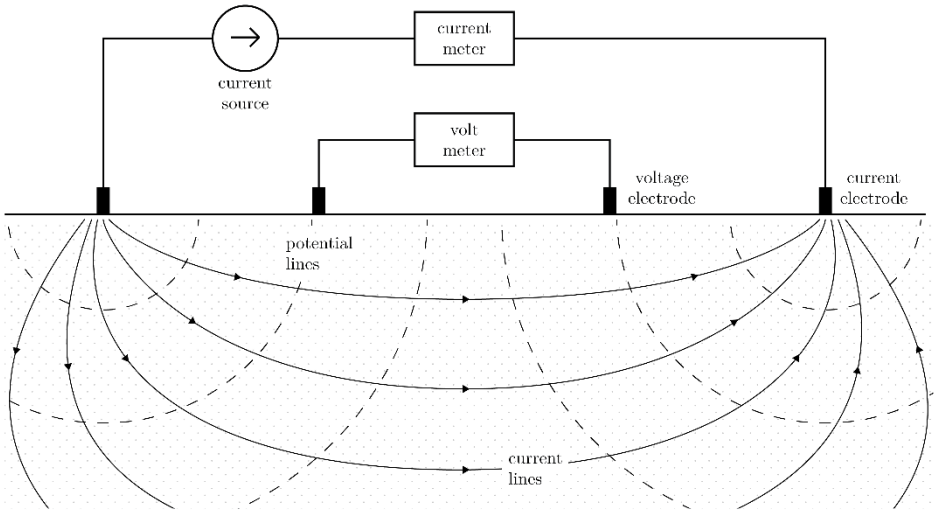

Figure 2: Diagram of a typical geophysical prospecting setup.

Environmental electric fields also are measured for large-scale weather analysis such as the quasi-static electric fields above storm clouds to predict thunderstorms [22], [23]. Additionally, seismologists analyze the atmospheric electric fields [24], [25] such as those collected before the infamous 2002 M6.8 earthquake in Taiwan [26] to better understand environmental conditions in hopes of finding better measures for earthquake prediction and disaster preparedness.

1.3 Research Motivation

The main objective of this research is to use electric fields for imaging applications. This includes directly imaging the electric fields themselves as well as using electric fields to develop a visual form of perception, similar to the behavior of the described aquatic

species. Appropriate means of measuring and utilizing electric fields can be more effectively developed by first characterizing how electric fields behave and how pervasive they are. Electric fields in or near the very low frequency (VLF) range will be of primary interest due to their accessibility, ability to better penetrate objects, and quasi-static nature to leverage lower order approximations.

The ability to image electric fields opens the potential to address many new problems. It can complement the tools used in security applications, such as searching for concealed electronics in a discreet, portable, and cost-effective manner [27]. Target users include Travel Security Administration (TSA) airport security employees and Explosive Ordnance Disposal (EOD) personnel searching for hidden bombs in a post-disaster scenario, e.g. the Boston Marathon Bombing [28].

Electric field imaging can also enhance safety. Imaging electrical wiring behind walls at construction sites can prevent injuries and undue damages [29]. Medical imaging with electric fields also provides a safe, non-ionizing alternative [30] to the more commonly employed carcinogenic x-rays [31].

In industry, electric field imaging can help not only detect but pinpoint sources of electromagnetic interference (EMI) for circuit designers by mapping out the electronic activity of circuits. This is a common but very time consuming, arduous, and expensive task when using traditional methods [32].

1.4 Previous Work

In addition to the current commercial applications mentioned in the previous sections, there is a large body of electric field sensing research in academia [6], [7], [12], [33], [34], [35]. It should be noted that a portion of the work in this dissertation includes and/or is built off work documented in my Master's thesis [36], the main related deliverable being a new passive method of electric field imaging. The details will be included and described throughout the dissertation.

The foundation of both my Master's and Doctoral work was first largely laid out by David Hull and his Electric Field Sensing Group at the Army Research Laboratory. This includes his comprehensive models and reviews of various electric field sensors [37] and their performances in a series of military-based applications [38], [39]. Before delving into electric field imaging, it is important to cover a basic understanding of electric field sensing as the performance of the imager will be directly correlated to the performance of each sensor.

Passive methods of electric field sensing characterized by Hull include potential sensors, vector electric field sensors, and electric charge induction sensors which are also known as D-dot sensors. These sensors respectively operate by measuring the voltage at specific points in space, the voltage difference between various points in space to form a 3-D field, and the time derivative of the electric field. Passive methods of electric field sensing are capable of detecting high-velocity bullets [38], [40] and even classifying helicopters at extremely low frequencies [39].

The systematic review of these passive sensors guided the decision to focus on D-dot sensors for the research in this dissertation as they are highly sensitive, compact, cost-effective, and elegant in design. This allowed for easy fabrication and quick turnaround on setting up experiments and acquiring data.

Perhaps the most notable work in academia that first used the term ‘electric field imaging’ was by J. Smith in his Ph.D. dissertation [6]. In it, he describes an array of transceiver electrodes to solve geometric inverse problems, particularly regarding human motion. While this is not imaging the electric fields directly, it uses electric fields as the medium to form perception.

Concomitant with the research presented in this dissertation, NASA has developed an electric field imaging system which directly measures the magnitude and direction of electrostatic fields [30], [41]. The technology uses an array of sensors which measure voltage differences at multiple points within the sensor from which magnitude and direction can be derived from inversion algorithms.

1.5 Contributions

This dissertation presents an electric field imaging system that directly images electric field strengths. The electric field sensor utilized in this research is the D-dot sensor for reasons already mentioned.

1.5.1 Characterizing Electric Field Noise in Cables

The foundational understanding of electric field behavior was predicated on the work of the first contribution, a comprehensive overview of electric field noise coupling into various long-distance cables with various grounding configurations. Each cable had a different shielding mechanism allowing the review to evaluate which was most effective at minimizing capacitive noise while the grounding configurations allowed assessment of how to minimize inductive coupling.

1.5.2 Passive Electric Field Imaging

The second contribution concerns the imager itself. Like other imaging approaches, an array of sensors was assembled, enabling each sensor to act as a pixel in the image. A lock-in amplifier was used in conjunction with the D-dot sensor to achieve a high signal-to-noise ratio (SNR). The imaging hardware was fabricated on both printed circuit board (PCB) and a flexible substrate and was the first direct electric field imaging system of its kind. With the imager, electric field images of concealed wires and EMI from a DC-DC buck converter were resolved.

1.5.3 Active Electric Field Imaging

The D-dot sensor requires a time-varying charge source to register a reading. Therefore, a D-dot cannot directly read static electric fields or objects that do not generate

electric fields. The third main contribution addresses this shortcoming with an active imaging method. This approach uses an electrode to generate a known electric field and reads distortions created by objects in the known field. The distortions can then be inverted to provide a meaningful interpretation.

1.5.4 Inverse Electric Field Imaging

The inversion algorithms constitute the final contribution of this research. The algorithm is based on computed tomography in which electric field projections are taken at various angles to reconstruct an image of a higher dimension, e.g. one-dimensional projections to a two-dimensional image. Both a filtered backprojection algorithm and algebraic reconstruction with sparsity enforcing regularization algorithm were tested. The latter allowed for higher quality images with fewer angles with certain images.

1.6 Organization

This dissertation is loosely divided into five main sections:

Section		**Chapters**
1	Theory and Basics	1-4
2	Passive Imaging	5-8
3	Active Imaging	9

Chapter 2 covers basic electromagnetic principles, including Maxwell's Equations. It then delves into greater detail of the electrostatic theory behind the D-dot sensor in particular. Chapter 3 demonstrates the effect of some of these electrostatic principles with real data of noise in various cables. Each cable has unique shielding and is tested over long distances in a controlled laboratory setting. The effects of various grounding configurations are also explored. Chapter 4 presents results from derivatives of these experiments when conducted under high-voltage power lines.

Chapter 5 marks the beginning of the discussion of electric field imaging, starting with the hardware assembled for Gen 1. The Gen 1 imager was a one-dimensional array fabricated on PCB. It demonstrated the feasibility of the electric field imaging array and set the foundations of the hardware needed in the system as a whole but had several fundamental flaws addressed in future generations.

Chapter 6 presents an extension of the Gen 1 imager in the form of a fully two-dimensional active matrix array, also on PCB. The results of this design are discussed, specifically the high leakage in the access transistors which effectively negates the second dimension of the imager. The subsequent Chapter 7 also presents a two-dimensional active matrix array, but on a flexible substrate InGaZnO thin-film transistors (TFTs) which address the shortcomings of its PCB counterpart.

Chapter 8 presents the first fully functional imaging system which abandons the active matrix architecture but rather dedicates an amplifier to each pixel. The PCB array

captured the first valuable set of two-dimensional images despite being a one-dimensional array. This was achieved by mechanically stepping the array between measurements, dubbing this imager iteration the “stepper array.”

Chapter 9 extends on the stepper array with a fully two-dimensional array with dedicated amplifiers. Eliminating the need to mechanically step the imager allowed for a much more streamlined and practical approach to obtaining images. This led to the development of new ways to image such as the active method. The active method images distortions objects create in a known electric field, expanding the space of objects that can be imaged beyond electric field sources. The images of distortions can then be processed in a way to extract meaningful representations.

Chapter 10 covers the theory of the computed tomography algorithm and its application to electric field images obtained with the active method. Several implementations based off the principles of computed tomography were tested with simulated electric field data.

Chapter 11 concludes the dissertation with a synopsis of the research and a few final remarks. This includes future work in electric field imaging and its greater context to achieve grand big picture goals.

Chapter 2

ELECTROSTATIC THEORY AND THE D-DOT SENSOR

2.1 Maxwell's Equations

An overview of basic electromagnetics is desirable to better understand the character of electric fields and the mechanisms to sense them. Maxwell's equations (Equation 2.1 –2.5) cover the fundamentals of electricity and magnetism, giving a high-level mathematical understanding of relationships in a field.

$$\nabla \times \mathbf{E} = -\frac{\partial \mathbf{B}}{\partial t} \qquad (2.1)$$

$$\nabla \times \mathbf{H} = \boldsymbol{J}_f + \frac{\partial \mathbf{D}}{\partial t} \qquad (2.2)$$

$$\nabla \bullet \mathbf{D} = \rho_f \qquad (2.3)$$

$$\nabla \bullet \mathbf{B} = 0 \qquad (2.4)$$

$$\nabla \mathbf{J}_f = -\frac{\partial \rho_f}{\partial t} \qquad (2.5)$$

In the equations, **E** is the electric field, **B** is the magnetic field, **D** is the electric displacement, **H** is the magnetic field strength, ρ_f is the charge density, and $\mathbf{J_f}$ is the current density. In isotropic media, $\mathbf{D} = \epsilon\mathbf{E}$, $\mathbf{B} = \mu\mathbf{H}$, and $\mathbf{J_f} = \sigma\mathbf{E}$ where ϵ is the permittivity, μ is

the permeability, and σ is the conductivity. These equations will frequently be referenced in the electrostatic derivations.

2.2 Very Low Frequency and Quasi-static Conditions

The research in this dissertation concerns electric field sensing in or near the VLF range which is defined by the International Telecommunication Union (ITU) to be between 3-30 kHz [42]. Some experiments utilize frequencies lower in the spectrum and fall into the extremely low frequency (ELF) and super low frequency (SLF) range and some a little more into the low frequency range (LR), but all remain relatively close (e.g. ~100 Hz and 45 kHz). Regardless, the characteristics of interest are consistent despite these relatively small deviations from the range. Therefore, for the sake of simplicity, all experiments will be referenced as operating in VLF. ITU themselves often do not list frequency bands below the VLF range so it is not unreasonable to lump the nomenclature together [43].

The choice for utilizing VLF is that, unlike MHz and GHz waves, it has the significant advantage in its ability to better penetrate objects [44], i.e. minimize attenuation through a medium. This is why submarines use VLF waves as a means of underwater communication: they are better equipped to penetrate the medium of water [45]. VLF waves are also utilized to penetrate the earth's crust for subterranean mapping from large scale geophysical prospecting for ore and oil to even consumer metal detectors for beach-goers and treasure seekers [46]. Furthermore, some of the applications of interest operate in VLF including the 60 Hz and 50 Hz power grid utility frequency standards respectively in the Americas/parts of Asia and most other parts of the world [47].

To better understand the characteristics and effects VLF waves have in a physical system, as opposed to those at higher frequencies, two new parameters are introduced in time-rate, α, and scaled time, $\tau = \alpha t$. This creates a family of fields directly associated with frequency. If the time dependent Maxwell's equations (namely Equations 2.1, 2.2, and 2.5) are rewritten with this scaled time parameter, the equations can be respectively manipulated to:

$$\nabla \times \mathbf{E} = -\alpha \frac{\partial \mathbf{B}}{\partial \tau} \qquad (2.6)$$

$$\nabla \times \mathbf{H} = \boldsymbol{J}_f + \alpha \frac{\partial \mathbf{D}}{\partial \tau} \qquad (2.7)$$

$$\nabla \mathbf{J}_f = -\alpha \frac{\partial \rho_f}{\partial \tau} \qquad (2.8)$$

In the power series expansion of **E** in α around $\alpha = 0$

$$\mathbf{E}\ x, y, z, \tau, \alpha\ = \alpha^i \sum_{i=0}^{\infty} \mathbf{E}_i\ x, y, z, \tau \qquad (2.9)$$

where

$$\mathbf{E}_k\ x, y, z, \tau\ = \frac{1}{k!} \left[\frac{\partial^k \mathbf{E}\ x, y, z, \tau, \alpha}{\partial \alpha^k} \right]_{\alpha=0} \qquad (2.10)$$

the lower order terms sufficiently describe the low frequency behavior for a small enough α [6]. When the solution is sufficiently described by the zeroth and first order terms of this series, it is quasi-static [48]. A rule of thumb that suggests α is sufficiently small to be quasi-static is if the wavelength is 10 times larger than the longest physical structure in

the setup [49]. Since operating in VLF corresponds to wavelengths of 10s-100s of kilometers, and the structures in the experimental setups in this dissertation never go beyond the range of meters, the values of α are comfortably small enough.

Substituting the expanded forms of **E** and **B** into Equation 2.1 and combining all terms on one side yields

$$\nabla\times\mathbf{E}_0 + \sum_{i=0}^{\infty} \alpha^i \left(\nabla\times\mathbf{E}_i + \frac{\partial\mathbf{B}_{i-1}}{\partial\tau}\right) = 0 \qquad (2.11)$$

This requires each term to equal zero for all values of α. Therefore, each coefficient of all the powers of α must each equal zero. The remaining electric field equations can be derived similarly. Since the problem at hand is quasi-static, the zeroth and first order terms of Maxwell's equations will be derived. The zeroth order set is

$$\nabla\times\mathbf{E}_0 = 0 \qquad (2.12)$$

$$\nabla\times\mathbf{H}_0 = \mathbf{J}_{f0} \qquad (2.13)$$

$$\nabla \bullet \mathbf{J}_{f0} = 0 \qquad (2.14)$$

and the first order set is

$$\nabla\times\mathbf{E}_1 = -\frac{\partial\mathbf{B}_0}{\partial\tau} \qquad (2.15)$$

$$\nabla\times\mathbf{H}_1 = \mathbf{J}_{f1} + \frac{\partial\mathbf{D}_0}{\partial\tau} \qquad (2.16)$$

$$\nabla \bullet \mathbf{J}_{f1} = -\frac{\partial\rho_{f0}}{\partial\tau} \qquad (2.17)$$

The first order term of **E** relates to the zeroth term of **B** and vice versa. When observing Equation 2.16, it can be concluded that a zeroth order electric field induces a first order magnetic field proportional to the time derivative of the electric field. Therefore, a zeroth order electric field implies a zeroth order charge and by Equation 2.17, the time derivative of the charge induces a first order current. The remaining equations do not involve α but can be expressed as follows:

$$\nabla \bullet \epsilon \mathbf{E}_k = \rho_{fk} \qquad (2.18)$$

$$\nabla \bullet \mu \mathbf{H}_k = 0 \qquad (2.19)$$

2.3 Capacitance

Relating capacitance to electric fields helps in understanding how a sensor transduces the electric field to a readable current. The zeroth order electric field can be represented as a scalar potential. By Equations 2.16 and 2.19, of this field induces a first order current, yielding the well-known capacitance relationship

$$I = C \frac{dV}{dt} \qquad (2.20)$$

In the circumstance of two conductors, *i* and *j*, the capacitance of one due to the other is as follows:

$$\frac{Q_i}{V_j} = C_{ij} \qquad (2.21)$$

in which Q_i is the static charge on conductor i. If more than two conductors are involved, by linearity, the total charge induced by other conductors is the sum of their individual induced capacitances described by

$$Q_i = -\int_{S_i} \epsilon \mathbf{n} \bullet \nabla \phi_0 da = \sum_j C_{ij} V_j \qquad (2.22)$$

where S_i is the surface of i, and **n** is the normal of S_i. This further means that the first order currents are related to zeroth order charge and thus current entering a receiver, I_i, is determined by the time derivative of Qi

$$I_i = \frac{dQ_i}{dt} = \frac{d}{dt}\sum_j C_{ij} V_j = \sum_j C_{ij} \frac{dV_j}{dt} \qquad (2.23)$$

Therefore, currents are first order phenomena but are only used to measure capacitance while the zeroth order property is geometrically dependent [6].

2.4 The D-dot Sensor

D-dot sensors, also known as electric charge induction sensors, measure current proportional to the time derivative (dot) of the electric flux density (D), hence the name, by monitoring the current between multiple conducting electrodes [50]. The ground-field D-dot design transforms an electric field into a voltage by using one channel, of which the

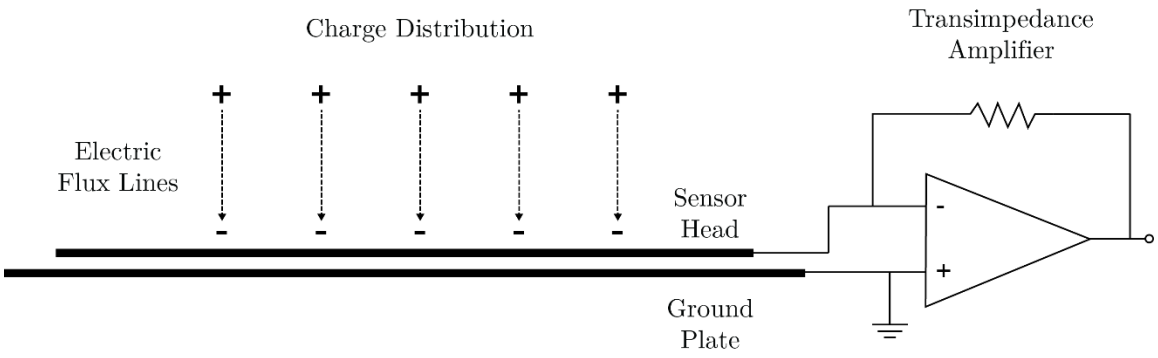

Figure 3: A snapshot in time of a schematic of the flat ground-field D-dot design.

sensor must be over a ground plane [51]. The design used in experiments described in this dissertation uses two flat conducting plates, Figure 3, though other geometries may be better suited for other applications. They are very sensitive and have, as mentioned, successfully detected high velocity bullets [38], [40] which induce charge on the order of pCs [38], [52]. Furthermore, D-dot sensors are simple in design, compact, and cost effective, allowing for rapid turnaround in fabrication and testing for effective small batch development for the electric field imaging array.

Electric flux is the flow of an electric field through a given area. Electric flux lines are a construct that can be used to visualize the direction and strength of the electric vector fields. In this visual, electric flux lines terminate on opposite charges in the surrounding environment. The D-dot sensor head, the top plate in the two-flat conducting plate design, provides an area for some of these flux lines terminate. This conducting plate is held at a virtual ground with an operational amplifier, which provides the equal and opposite charge necessary for the electric flux lines to terminate.

Underneath the conducting plate where electric flux lines terminate is a layer of insulation and a bottom conducting plate which is used as a reference to ground. For the

experiments in this research, it was desirable to reduce the distance between the bottom and top plate as much as possible to avoid fringing.

Electric flux terminating on the metallic plate of the sensor induces charge and the time-varying electric flux results in small currents flowing on and off the plate to provide the required charge. If the charge distribution above the sensor changes, the number of flux lines terminating on the upper plate changes. Since the D-dot sensor is held at a virtual ground, the small required change in charge results in a current flowing through a large feedback resistor in the operational amplifier, generating a time-varying voltage, the amplitude of which is proportional to the strength of the electric field impinging on the upper plate.

2.5 Wire Over a D-dot Sensor

Based off the principles from the equations already derived, an electrostatic model can be developed for the D-dot sensor. A very simple setup to model is a charged wire with a VLF time-varying voltage above a D-dot sensor because of the simplicity of dimensionality (1-D objects over 2-D plate in largely orthogonal projections). It also has meaningful applications such as measuring electric fields from power lines and circuitry. Since the model assumes VLF, the analysis is quasi-static and some basic characteristics can easily be demonstrated such as the signal strength being directly proportional to the frequency, sensor area, and field strength.

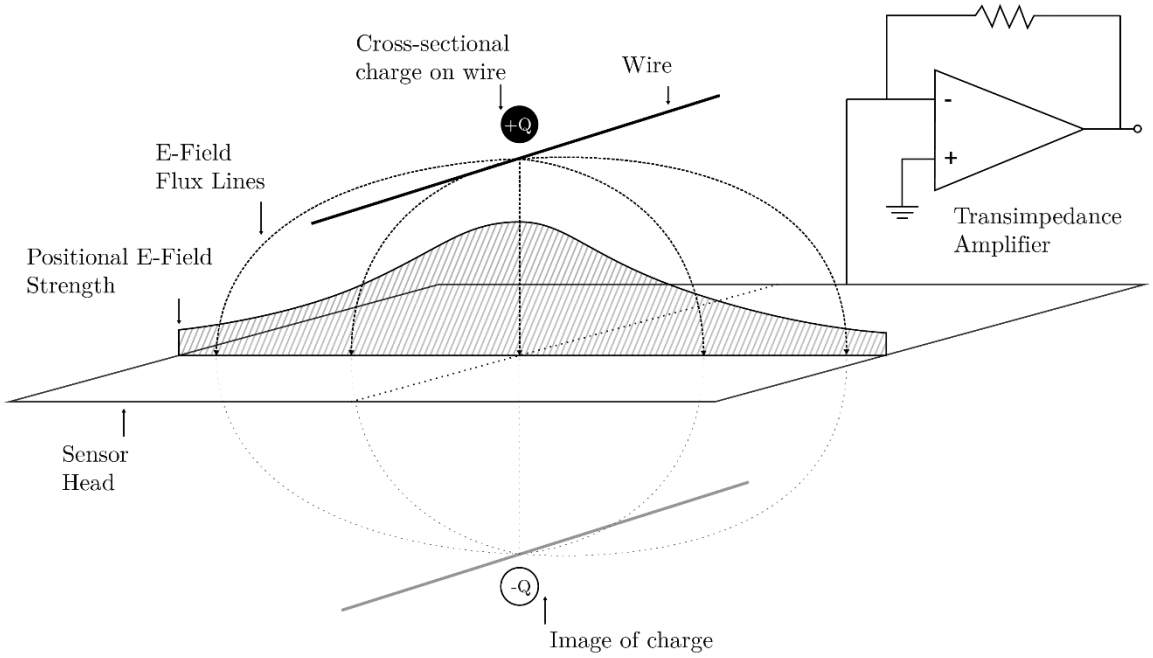

Figure 4: Diagram of the analytic model of a sample of electric flux lines radiating from a wire over a D-dot sensor using the method of images.

First, the electric field perpendicular to the D-dot sensor, $\mathbf{E}_{\perp}$, generated by the wire is described by

$$\mathbf{E}_{\perp} = \frac{\lambda}{\pi \epsilon h} \qquad (2.24)$$

where λ is the charge per unit length of the wire described by

$$\lambda = \frac{2\pi V t}{\ln\left(\frac{2h}{a}\right)} \qquad (2.25)$$

Here, ϵ is the permittivity of free space, h is the distance (or height) between the wire and the sensor, V is the voltage applied on the wire, and a is the radius of the wire. The voltage term can be further broken down to

$$V\,t\ = V\sin\ 2\pi ft \qquad (2.26)$$

and its derivative

$$V'\ t\ = 2\pi fV\cos\ 2\pi ft \qquad (2.27)$$

to better portray the time and frequency, f, aspects of the signal in the wire.

Substituting the above equations into the definition of the D-dot output current yields the expression

$$i_{Ddot} = A_{pixel}\frac{d}{dt}\epsilon E_{\perp} = A_{pixel}\frac{4\pi f\epsilon V'\ t}{h\ln\left(\frac{2h}{a}\right)} \qquad (2.28)$$

where A_{pixel} is the area of the D-dot sensor head. While the signal strength is proportional to the electrode area, it has been observed that the sensor is sufficiently sensitive to detect electric fields with relatively small D-dot sensors (e.g. 1 cm x 1 cm) both in simulation and real-world experiments.

The derivation assumes that the radius of the wire, a, is much smaller than the height so that the center of the wire can be treated as the location of the wire. The current generated at the D-dot is again the time derivative of the electric flux density and is proportional to the area of the sensor, Equation 2.28. As a frame of reference, for a minimum detectable D-dot current of 0.5 pA, a 1 cm^2 sensor can detect a 0.5 mm radius wire energized with a 5 V, 97 Hz signal as far as 1.2 m away.

The distribution of electric field magnitudes across a ground plate can be modeled by using the method of images. By taking a cross-section of the setup, it is reasonable to treat the slice of the wire over a conducting surface as a point charge in two dimensions.

$$E_r = 2\pi rh = \frac{\lambda h}{\epsilon} \quad \text{(Gauss Law)} \tag{2.29}$$

$$r = \sqrt{h^2 + \left| x - x_0 \right|^2} \tag{2.30}$$

By the method of images, the electric field along the surface is equal to calculating the net effect of polar charges equal in magnitude and distance from the surface location.

$$E_z = \frac{E_r h}{r} = \frac{\lambda h}{\epsilon 2\pi \left(h^2 + \left| x - x_0 \right|^2 \right)} \tag{2.31}$$

$$E = 2E_z \quad \text{(by symmetry)} \tag{2.32}$$

Using Gauss Law and simple algebra, the electric field strength can be calculated by

$$E = \frac{\lambda h}{\epsilon \pi (h^2 + \left| x - x_0 \right|^2)} + (\gamma) \tag{2.33}$$

in which x_0 is the offset of the point of interest and γ accounts for random noise.

Theoretically, the electric field vectors should be orthogonal to the surface of the sensor. The D-dot sensors, however, have some height and are not perfectly uniform so slight fringing is expected, especially along the edges. However, these deviations are minor and the dominant value is still the orthogonal component.

2.6 Connection to Imaging

Thus far, the electrostatic theory behind electric field sensing has been covered. From the overview, we can take advantage of the fact that the signal strength is proportional to the field strength and that the field is non-uniformly distributed in space. By implementing an array of D-dot sensors, each sensor can produce a signal proportional to the electric field strength in its locus. By discretizing electric field strength by means of a spatial mesh, an image can be resolved.

Chapter 3

ELECTRIC FIELD NOISE IN CABLES

This chapter presents a detailed study of external noise coupling into various cables in an electric field sensing system. The experiments were conducted in a highly controlled laboratory setting and determine how many bits of resolution are lost as a function of the type of cable used. Both capacitively (electric field) and inductively (magnetic field) coupled noise were considered in preparation for field tests under high-voltage power lines, covered in Chapter 4.

3.1 Background

External noise that is capacitively or inductively coupled into an electric field sensing system degrades sensitivity and limits performance. This is particularly of concern when the sensor and pre-amplifier are some distance from the data acquisition unit since the long cable needed to connect them forms a parasitic antenna. Different grounding configurations can also create ground loops which may inductively couple noise. An understanding of which type of cable, shielding, and grounding method minimizes noise coupling with significantly improve the performance of electric field sensing systems.

3.2 Experimental Setup for Capacitive Noise Coupling

A pair of 10'x1' parallel plates (8.25 cm apart) was driven with the Krohn-Hite 4402B ultra-pure sinewave oscillator [53] to create a uniform electric field. A 97 Hz, 7 V_{rms} voltage was applied to the plates resulting in a 120 V/m peak electric field. At one end, a 5" x 3" D-dot sensor was placed on the bottom plate and connected to a DLPCA 200 transimpedance amplifier [54]. The output of the amplifier was transmitted through a 3 m cable of choice with the necessary Bayonet Neill-Concelman (BNC) adapters into a data acquisition unit for processing.

A 16 bit NI-DAQ was used and connected via USB to a battery powered laptop where we are able to store and manipulate the data. The NI-DAQ, all connecting wires,

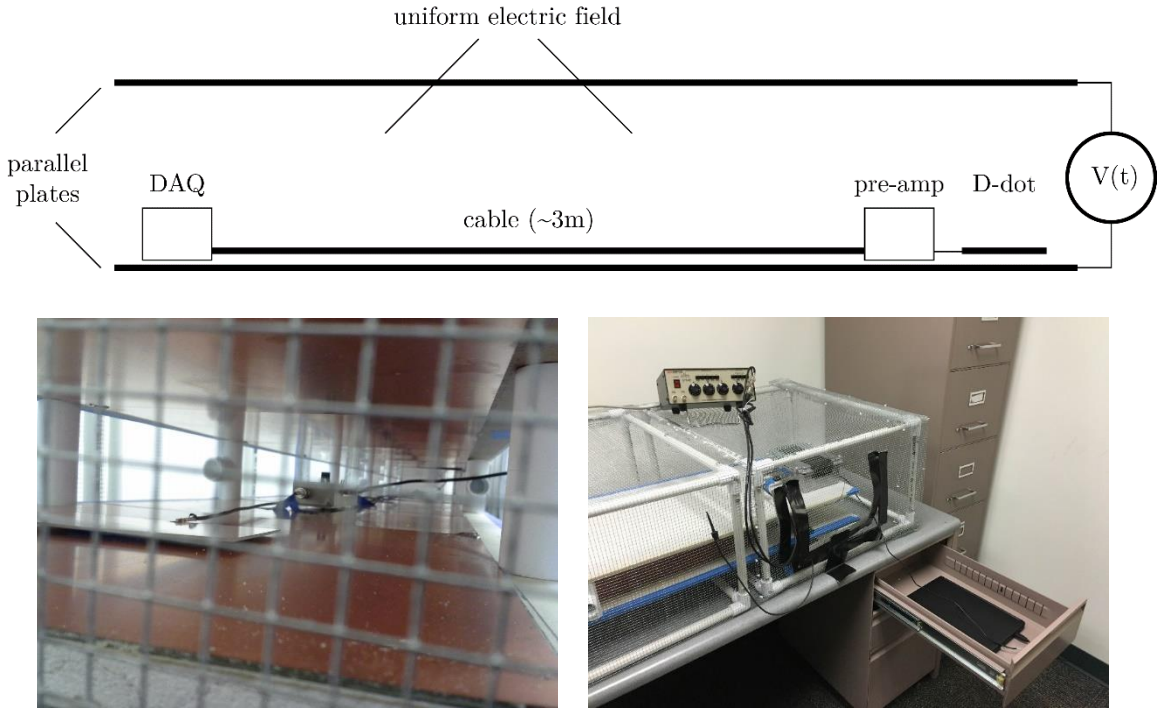

Figure 5: Diagram of test setup (top) along with photos of test setup from the D-dot end (bottom-left) and driving/reading end (bottom-right).

and driver circuitry were placed in a grounded metal box. This removed noise coupling into the exposed connections to the data acquisition unit and significantly improved repeatability of the results.

All components but the laptop and signal generator were placed inside a Faraday cage. For a given cable, measurements were taken with the full system connected, as well as with the D-dot sensor disconnected from the system. This allowed for observation of the noise being capacitively coupled into the cable. One set of measurements was also taken with the cable disconnected from the data acquisition unit. The BNC input to the data acquisition unit was covered with a 50 Ω termination to simulate the characteristic impedance of the cables being used. This measurement did not need to be taken for each cable type, as it does not depend on the cable.

3.2.1 Modifications

There were several adapters needed to convert the BNC output of the transimpedance amplifier to the various other cables carrying the signal, Figure 6. Also, adapters were needed to convert the cable back to a BNC before the signal could go back into the data acquisition unit box. This did not apply to the triax cable, as the data acquisition box also had a triax input. It should be noted that these adapters may be a source of noise. For example, the Ethernet to BNC adapter had an internal resistance of approximately 7 Ω. Table 6 lists all of the cable types, and the modifications each of them required.

Table 1: Description of modifications needed for each cable type.

Cable Type	Modifications Needed
Coax	None.
Twisted Pair	Two BNC to two wire adapters were used for each. On both ends, the signal from the BNC was attached to the blue wire inside the twisted pair cable. However, on one end, the BNC ground was attached to both the white wire inside the twisted pair cable, and to the shielding material. On the other end, the BNC ground was just attached to the white wire to avoid ground loops. The end with the BNC ground attached to the shielding layer in the twisted pair was connected to the transimpedance amplifier for consistency and to reduce resistance between the shielding layer and the actual ground.
Cat 5e, 6, 7	Two adapters which converted a BNC to an Ethernet were used. These take the signal and ground from the BNC, and run them through two of the wires on the cables. These do leave the shielding on the cables floating. While performing well, they did have ~7 Ω of resistance.
Audio	Two BNC to audio adapters were required. These adapters were higher quality than the BNC to Ethernet adapters, and had negligible resistance.
Triax	One BNC to triax adapter was needed. However, a BNC to triax adapter shorts the inner and outer shield of the triax together, defeating the purpose of triax. The adapter was modified to connect the BNC signal to the triax signal, connect the BNC ground to the outer shield of the triax, and to leave the inner shield floating. The inner shield was driven by buffer circuitry from the other end using a BUF-634.

Figure 6: Photo of terminations and adapters used - From left to right, there is the open BNC termination, the 50 Ω BNC termination, the BNC to triax adapter, the BNC to ethernet adapter, the BNC to audio adapter, and the BNC to two wire adapter, which was used for the twisted pair cable.

3.2.2 Noise and Variance Minimization Efforts

A considerable reduction of electrical noise was observed when the fluorescent lights were turned off and the room was isolated by fully closing the metal door. Powering down and unplugging all electronic devices (e.g. computers, printers) also made a significant impact on the signal to noise and distortion ratio (SNDR). Note that the transimpedance amplifier and signal generator were still connected through a power outlet. Furthermore, the laptop was on and, while battery powered, was potentially radiating electromagnetic noise. The effects of the laptop were controlled by placing it in a metal drawer before data was collected. The transimpedance amplifier was heavily shielded by design and the signal generator was placed outside the Faraday cage.

Furthermore, the gain of the transimpedance amplifier was turned down from 10^9 to 10^8. While this reduces signal amplitude below maximum, it allowed for a more controlled gain without saturating for the variety of setups. With the higher gain, we found that we were saturating under some setups making comparisons difficult.

With the electric field signal at 97 Hz, a 1024 samples/second rate was determined to be suitable for the time-frequency tradeoff as it is a power of two and is broad enough to capture the signal and its harmonics. Therefore, the maximum frequency is 512 Hz by the Nyquist theorem. The transient data was windowed with a Hanning window to accommodate for discontinuities at the ends and then run through a Fast Fourier Transform (FFT). The 97 Hz frequency bin was noted as our signal for all of the measurements.

In order to minimize the variance in our results, several trials were taken. Every time an experiment was run, 5 transient responses were collected using a MATLAB script. All the values were then reported in an average plot for the transient response, and for the FFT. The trials were repeated several times, until a result occurred repeatedly, and consistently.

3.2.3 Types of Measurements

The signal was measured with 1) the complete sequence of D-dot sensor – preamplifier – cable – data acquisition unit – laptop and 2) again without the D-dot sensor. For both configurations, measurements were made with 3) a single ground at the preamplifier and 4) with two grounds at the preamplifier and the DAQ forming a ground loop. Finally, 5) a measurement was made with no cable, preamplifier or D-dot sensor.

Table 2: All setup combinations for noise measurements.

Test Configuration	Points of Grounding	Termination Type
Full Sequence	Transimpedance Amp	None
Full Sequence	Transimpdeance Amp + DAQ	None
D-dot disconnected	Transimpdeance Amp	Open
D-dot disconnected	Transimpdeance Amp + DAQ	Open
Only DAQ + Laptop	DAQ	50 Ω

The rationale behind grounding both the transimpedance amplifier and the DAQ was that it may be necessary in the field despite it creating a ground loop. The 50 Ω termination was used for the final setup to simulate what the DAQ would see if connected to a cable.

3.3 Capacitive Coupling Results

The SNDR values for each experiment were calculated borrowing methods used to characterize analog to digital converters. The signal power consisted of the summation of the 97 Hz bin and the 6 frequency bins to either side (for a total of 13 bins). The noise consisted of the remaining bins minus the first 12 frequency bins (to eliminate DC offset and 1/f noise) and any bins within a +/- 40 bin range from the 97 Hz bin (to prevent skirts in the signal counting as noise). The SNDR is then calculated by finding the ratio of the signal energy to noise energy.

To find the average of the five trials, the raw complex FFT sums of both the signal and noise components were averaged before finding the ratio of powers. The experimental results can be found in Table 3. Since the setup with 3 disconnects was independent of the cable type (as it had no cable connected) it is presented separately in Table 4.

Table 3: Principal results of capacitive coupling experiments.

	Full Detection Chain		With D-dot Disconnected	
Cable	**Avg SNDR**	**Avg SNDR (with GND loop)**	**Avg SNDR**	**Avg SNDR (with GND loop)**
Coax	52.24	53.32	-10.95	-10.94
TP	34.98	28.21	-9.79	-11.26
Cat 5e	23.07	22.76	-10.36	-10.5
Cat 6	56.3	54.71	-9.81	-10.25
Cat 7	55.59	57.9	-9.87	-11.66
Audio	55.8	57.3	-10.62	-10.74
Triax	56.23	58.74	-12.9	-9.37

Table 4: Average SNDR for the 3 disconnect setup (DAQ unit).

	Avg SNDR	**Avg SNDR (with GND loop)**
Coax Box	3.19	-5.73
Triax Box	-12.19	-13.71

The cable with the highest SNDR for the fully connected system, and with no ground loop was the Cat 6 cable. This cable was followed closely by the triax, the audio, and the Cat 7 cables. These cables were within 0.7 decibels of each other, so they are all

very close in performance. Keep in mind the Cat 6 and 7 cables had a less expensive adapter, with 7 Ω resistance from end to end. The difference between triax, audio and Cat 6, 7 cables appears to be statistically insignificant and one should be chosen based on cost.

Next was the coaxial cable with slightly poorer performance. It had an SNDR 4.06 decibels lower than the Cat 6, showing that the coax cable will have noticeably more noise capacitively coupled into it than the cables mentioned earlier. Another 17 decibels behind the coax cable was the twisted pair cable. This shows that the twisted pair cable is far noisier than all the cables mentioned earlier. This is surprising, the twisted pair cable was expected to have similar performance to the coax cable, as they have a similar shielding structure. This leads to the speculation that the adapters used on the twisted pair cable were a large source of noise. Trailing the twisted pair cable by 12 dB is the noisiest cable of all, the Cat 5e cable.

When the cables were tested again with a ground loop, some of their SNDR values increased, while others decreased. In either case, the value did not fluctuate much, and the changes were almost insignificant. It is believed that the impact of the ground loop effect varied depending on the cable under test. In some cases, the benefits of having a direct connection to ground at various critical points in the system outweighed any noise that may have inductively coupled in through the ground loop.

3.4 Experimental Setup for Inductive Noise Coupling

Shielding VLF magnetic fields can be particularly challenging. While a metallic box or Faraday cage readily shields electric fields, 5 cm of aluminum is necessary for 52

dB of attenuation of a 60 Hz magnetic field [55]. The goal of these set of experiments was to determine which of the aforementioned cables are most resistant to inductively induced noise when measuring VLF electric fields with a D-dot sensor. This served as a bit of a stress test to measuring ground loops in the field.

The experimental setup consists of Helmholtz coils to generate a magnetic field and parallel metallic plates to generate an electric field. The parallel metallic plates are placed in the center of the Helmholtz coils. The entire setup is placed in a grounded metal can serving as a Faraday shield. The same 5" x 3" D-dot sensor is placed on the grounded side of the parallel metallic plates and connected to the DLPCA-200 ultra-low noise transimpedance amplifier [54] adhered to the inside of the metallic can. The cable under test then runs through the center of the Helmholtz coils and out of the can, Figure 7. Again, the NI-DAQ 16 bit digital to analog converter digitizes the signal which is captured by a laptop computer.

Since a thorough study was done on capacitive coupling, the higher resolution 16 bit Krohn-Hite signal generator [53] was reserved to generate the 137 Hz magnetic field.

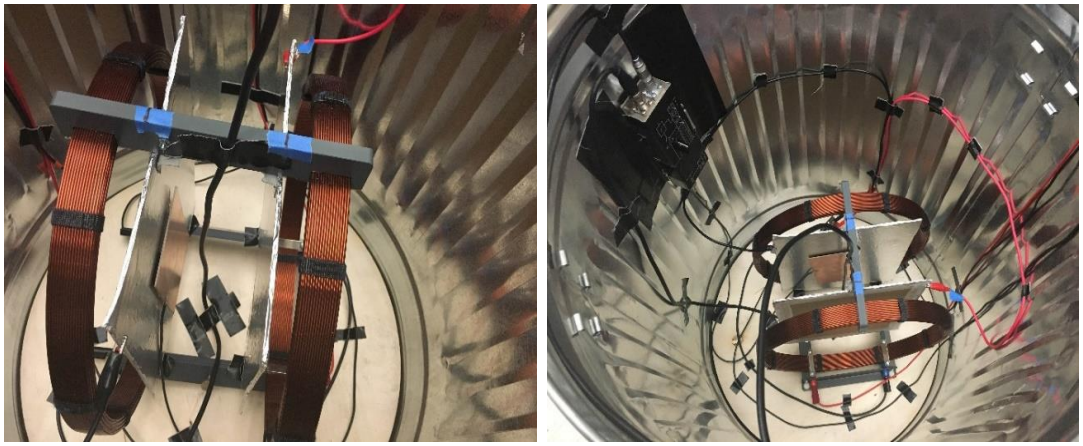

Figure 7: Photos of the experimental setup.

The signal was fed through the BOP amplifier to drive the Helmholtz coil. The Helmholtz coil is driven with 0.40 A resulting in a magnetic flux density at the center of 0.3 mT. The strength of the magnetic field in the center was confirmed with a gaussmeter.

The lower resolution 14 bit Agilent signal generator [56] provided the 97 Hz 18 V_{pp} sine wave to generate the electric field between the parallel plates. With the plates 8.25 cm apart, the resulting electric field was 7.71 V_{rms}/m. These metallic plates were formed with aluminum foil on cardboard to reduce the Eddy currents generated by the overlapping magnetic field. Such currents would induce their own magnetic fields distorting the applied magnetic field.

The D-dot sensor will pick up a strong signal from the 97 Hz electric field. The strong magnetic field at 137 Hz will penetrate the cables to varying degrees. The only other signals that would be present would be background noise such as cell phones, radio stations, electric machinery in the building, and the 60 Hz utility frequency which may penetrate the Faraday cage. In addition, any nonlinearities may result in harmonics of these frequencies. Finally, there is ultimately some level of quantization noise from the analog to digital converter.

3.5 Inductive Coupling Results

A quick summary of the performance of each cable is presented in Table 5. Spectral samples for each cable are presented in Figure 8.

Table 5: Qualitative results of each cable in the inductive noise coupling setup.

Cable Type	Qualitative Results
Coax	Quiet transient signal and the FFT spectrum is excellent, similar to the audio cable. The 137 Hz signal is at ~-70 dB and the 60 Hz signal is not noticeable even though the noise floor is very low.
Twisted Pair	Quiet transient signal and the FFT spectrum has a low noise floor but not as low as the best cables. The 137 Hz signal is at ~-70 dB and the 60 Hz signal is present at -80 dB. Very few harmonics can be seen.
Cat 5e	Very noisy transient signal with the resulting noise floor at least 35 dB higher than the audio cable. The 60 Hz and 137 Hz peaks are even higher than in the audio cable but less prominent due to the extremely high noise floor. There is also a prominent harmonic at 240Hz.
Cat 6	Marginally better transient signal than Cat 5e but still very noisy with the resulting FFT noise floor at least 30 dB higher than the audio cable. The 137 Hz magnetic signal peak is high but the 60 Hz signal is less noticeable. The primary electric signal at 97 Hz is weaker. There are prominent harmonics at 240 Hz and 360 Hz.
Cat 7	Significantly better transient signals compared to other Cat cables with the resulting FFT noise floor approaching that of the audio cable. The 137 Hz magnetic signal peak is high and the 60 Hz signal is quite evident at -85 dB. There is a prominent signal near 200 Hz of unknown origin. Power harmonics at 180 Hz and 300 Hz are also visible.
Audio	The FFT clearly has a magnetic signal penetrating the cable at 137 Hz in addition to the primary electric signal at 97 Hz. There is a weak 60 Hz also penetrating the cable. Otherwise the noise floor is uniform without noticeable harmonics above the ~-115 dB noise floor.
Triax	Quiet transient signal and the FFT spectrum has a low noise floor. The 137 Hz signal is higher at ~-60 dB and the 60 Hz signal is present at -80 dB.

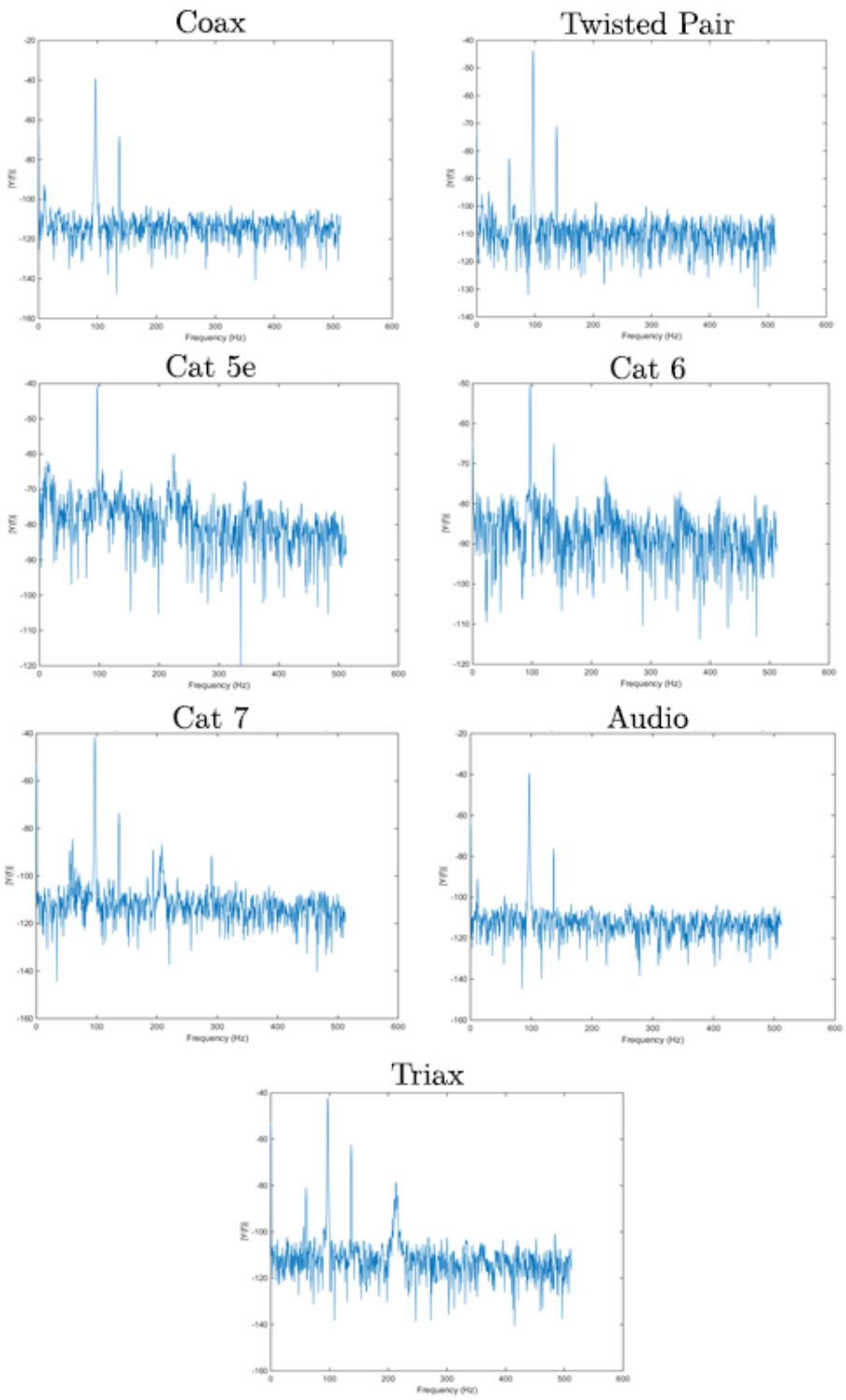

Figure 8: Sample single-sided amplitude spectra of coax, twisted pair, Cat 5e, 6, 7, audio, and triax cables (from left to right) in the inductive noise coupling setup.

Boxplots were compiled in R to compare the data from the 5 averaged runs for each cable. When comparing the 137 Hz magnetic peak, best rejection was achieved with the audio and Cat 7 cables, Figure 9. However, the best rejection of 60 Hz noise due to both electric and magnetic fields is audio and coax cables, Figure 10. Note for both of these plots, there is a steady improvement in the rejection performance from the Cat 5e to 7 cables, consistent with the increasing shielding.

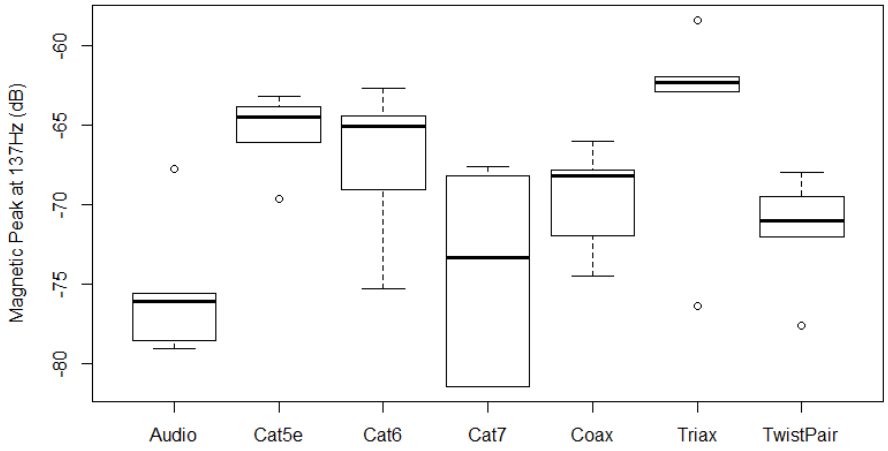

Figure 9: Boxplot comparing 137 Hz magnetic signal peak for each cable.

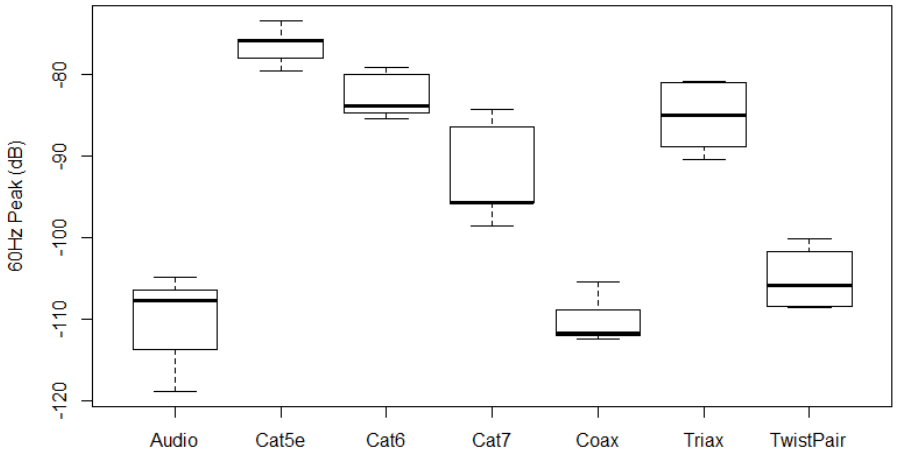

Figure 10: Boxplot comparing 60 Hz noise peak for each cable.

The audio, coax and Cat 7 cables have the lowest noise floor followed closely by the triax and twisted pair, Figure 11. Cat 5e and 6 had very poor noise floors. The best performing cables for magnetic shielding and low noise floor are the audio and Cat 7 cables, Figure 12. However, they do not have the strongest primary signal peak for the 97 Hz electric field. The highest 97 Hz signal is for the Cat 5e and 6 cables followed by the coax cable. This may be due to relatively poor shielding characteristics overall.

Since the cable runs through the Helmholtz coils and between the parallel plates generating the electric field, additional 97 Hz signal may be leaking into the cable enhancing the primary signal detected with the D-dot sensor. This effect may explain the slightly superior SNDR of the coax cable followed closely by the audio cable, Figure 12. The extra 97 Hz signal in the Cat 5e and 6 cables did not make up for the excess noise also coupled into the cables.

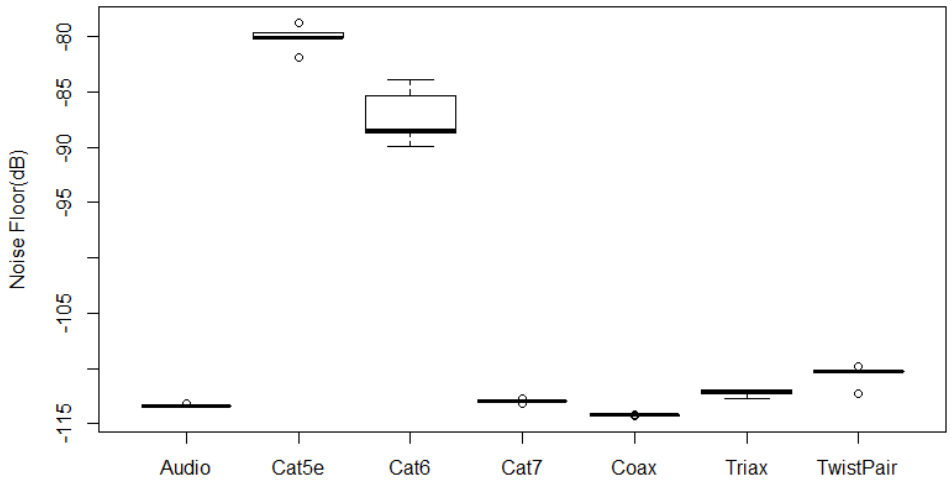

Figure 11: Boxplot comparing noise floors for each cable.

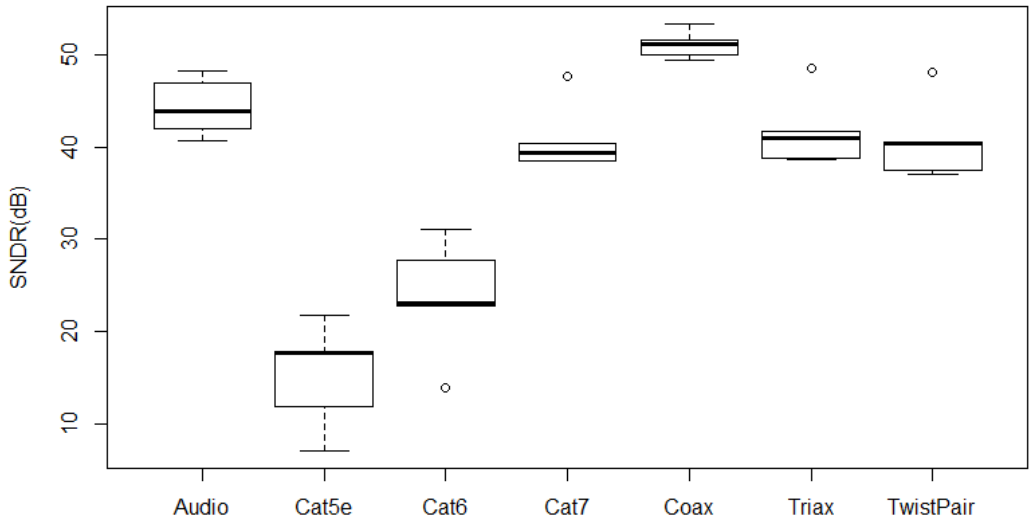

Figure 12: Boxplot comparing the SNDR for each cable.

Chapter 4

ELECTRIC FIELD NOISE FROM HIGH-VOLTAGE POWER LINES

The penetration of 60 Hz electric and magnetic fields from 500 kV and 13.8 kV power lines into various cables is experimentally measured in the field. The cables studied include the cables in the previous chapter as well as the LEMO cable. Extensive tests were conducted to estimate a statistical distribution of cable performance. Cables were placed both parallel and perpendicular to the power line. Various grounding configurations were investigated including multiple grounds forming a ground loop through the earth.

4.1 Background

Measurement of low frequency electric and magnetic fields are important for non-invasive load monitoring of power lines for grid stability and a variety of other applications. Such monitoring is particularly important for energy management for micro-grids at forward operating bases. As demonstrated in the previous chapter, external noise that is capacitively or inductively coupled into the system at places other than the sensor head degrades the sensitivity and limits performance.

In addition, grounding both the sensor and the remote electronics results in a large ground loop. Significant loop currents can be induced in the presence of strong magnetic fields near sources such as high-voltage power lines. An understanding of which type of

cable, shielding and grounding method minimizes capacitive and inductive noise coupling will significantly enhance the performance of power line monitoring systems.

Here, electric and magnetic noise coupling is measured from 500 kV and 13.8 kV power lines into various cables with perpendicular and parallel orientations and with various grounding configurations.

4.2 Experimental Setup

The measurements were made under 500 kV and 13.8 kV power lines over a flat desert ground. The environment had no trees which would otherwise act as electrical shorts distorting the electric fields. The field distribution was modeled with a custom program, ARL Plums, inputting the tower dimensions and separation. The electric fields at the ground are plotted in Figure 13. The asymmetry in the fields for the 500 kV line reflects the asymmetry in the power lines with two phases on one side and one phase on the other.

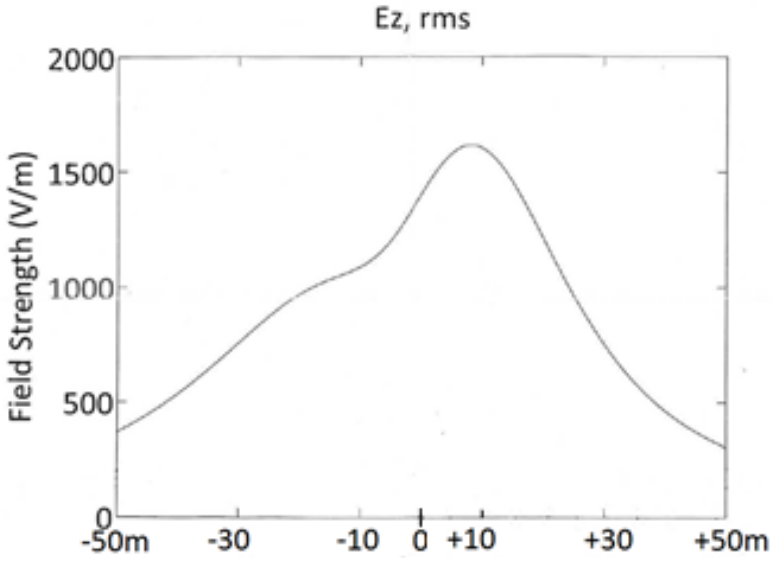

Figure 13: Electric field distribution for a 500 kv power line modeled with ARL PLUMS.

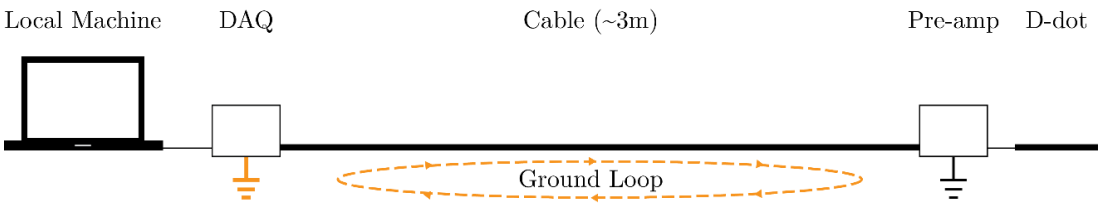

Figure 14: Diagram of experimental setup and the creation of a ground loop when a ground is added at the data acquisition unit (highlighted in orange).

The experimental setup mimics the measurement of electric fields with a D-dot sensor but with the D-dot sensor removed, Figure 14. The D-dot sensor is replaced with a shielded coaxial open load to a low noise transimpedance amplifier. An approximately 9' commercial cable of one of the different types connects the preamplifier to a 16 bit NI-DAQ analog to digital converter. The data acquisition unit was encased in an aluminum box with appropriate connectors to the cable. This shielding box reduced field penetration to the input connections of the data acquisition unit. A laptop computer captured and stored the digitized data. The removal of the D-dot sensor would ideally reduce the measured signal to zero, but field leakage into the various components, primarily the long cable, would result in a measurable 60 Hz signal indicative of the quality of the cable shielding.

Measurements were taken with a single ground connection at the pre-amplifier, with a single ground connection at the data acquisition unit, and with ground connections at both locations. The last configuration results in a ground loop that can pick up inductive signal from the power lines. Measurements were made with the cable under test oriented both parallel and perpendicular to the power line.

Two seconds of transient data, at 1024 samples/second, was windowed with a Hanning window followed by an FFT. The SNDR was the calculated consistent with the method described in the previous chapter. Because the field test was not as controlled as

the laboratory, each testing configuration collected 25 transient responses (up from 5) to accommodate for higher variance. The signal to noise energy was calculated and stored along with observations about the test setup. The resulting data is represented in boxplots generated in R.

The cables tested included coaxial, triax, audio, LEMO, shielded twisted pair, Cat5e, Cat6, Cat7. All were approximately 3 m long with the exception of the LEMO cable which was 6.05 m. The exact lengths and cost per length are given in Table 6. The audio, LEMO, twisted pair, and Cat 7 Ethernet cables are shielded twisted pair structures of varying quality and cost. The Cat 5e and Cat 6 Ethernet cables are twisted pair but do not have a shielding sheath.

The same corresponding adapters were used to convert the BNC output of the transimpedance amplifier to the various cables carrying the signal and to convert the cable back to a BNC to connect to the data acquisition unit. This did not apply to the triax and LEMO cables, as the data acquisition box also had those connectors.

Table 6: All cables used in testing along with their exact lengths and cost per meter.

Cable Type	Length (m)	Cost ($/m)
Coax	3.07	0.82
Triax	3.12	62.18
Audio	3.10	4.71
Shielded Twisted Pair	3.00	4.29
Cat 5e	3.58	0.60
Cat 6	3.05	2.54
Cat 7	3.05	3.60
LEMO	6.05	n/a

4.3 Results of 500 kV Power Line

An initial set of experiments were conducted with the cables placed directly under and parallel to the 500 kV power line with the sensor disconnected. The system was grounded to earth in one place at the preamplifier. Typical spectra of the transient signal for coax, LEMO and Cat 5e Ethernet cables are shown in Figure 15.

Ideally, there should be no 60 Hz signal detected since the sensor is removed. The coax cable is notably quiet with no 60 Hz signal present. The LEMO cable also has no noticeable 60 Hz penetration but does have several other frequencies 10 to 20 dB above the noise floor. Consistent with laboratory measurements, Cat 5e has substantial 60 Hz signal, approximately 25 dB above the noise floor.

Comparing the SNDR for all cables, Figure 16, the three Ethernet cables stand out for poor shielding of 60 Hz signals, consistent with their lack of a grounded shield around the twisted pairs. Although the Cat 7 has a shield, the Ethernet to coax connectors left the shield floating. Similar results were obtained for the cables placed perpendicular to the power line, Figure 16b. A third set of data was taken with the cables coiled with an

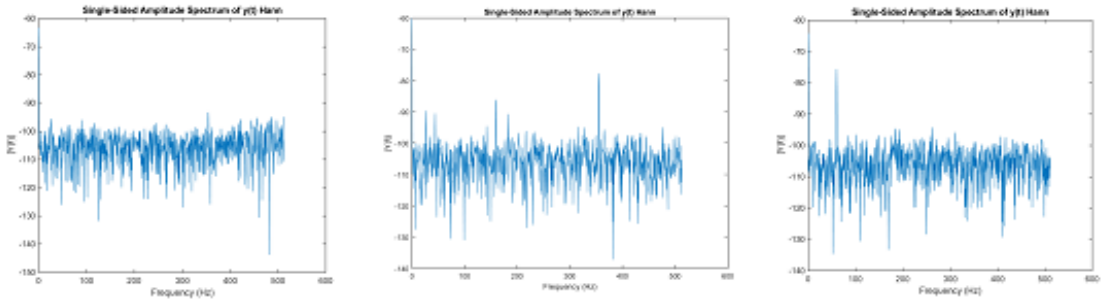

(a) (b) (c)

Figure 15: Single-side amplitude spectra of transient signals coupled into a) Coax, b) LEMO and c) Cat 5e Ethernet cables under 500 kV power line.

approximate diameter of 30 cm, Figure 16c. Here the shielding ability of the triax and twisted-pair are degraded in addition to the Ethernet cables.

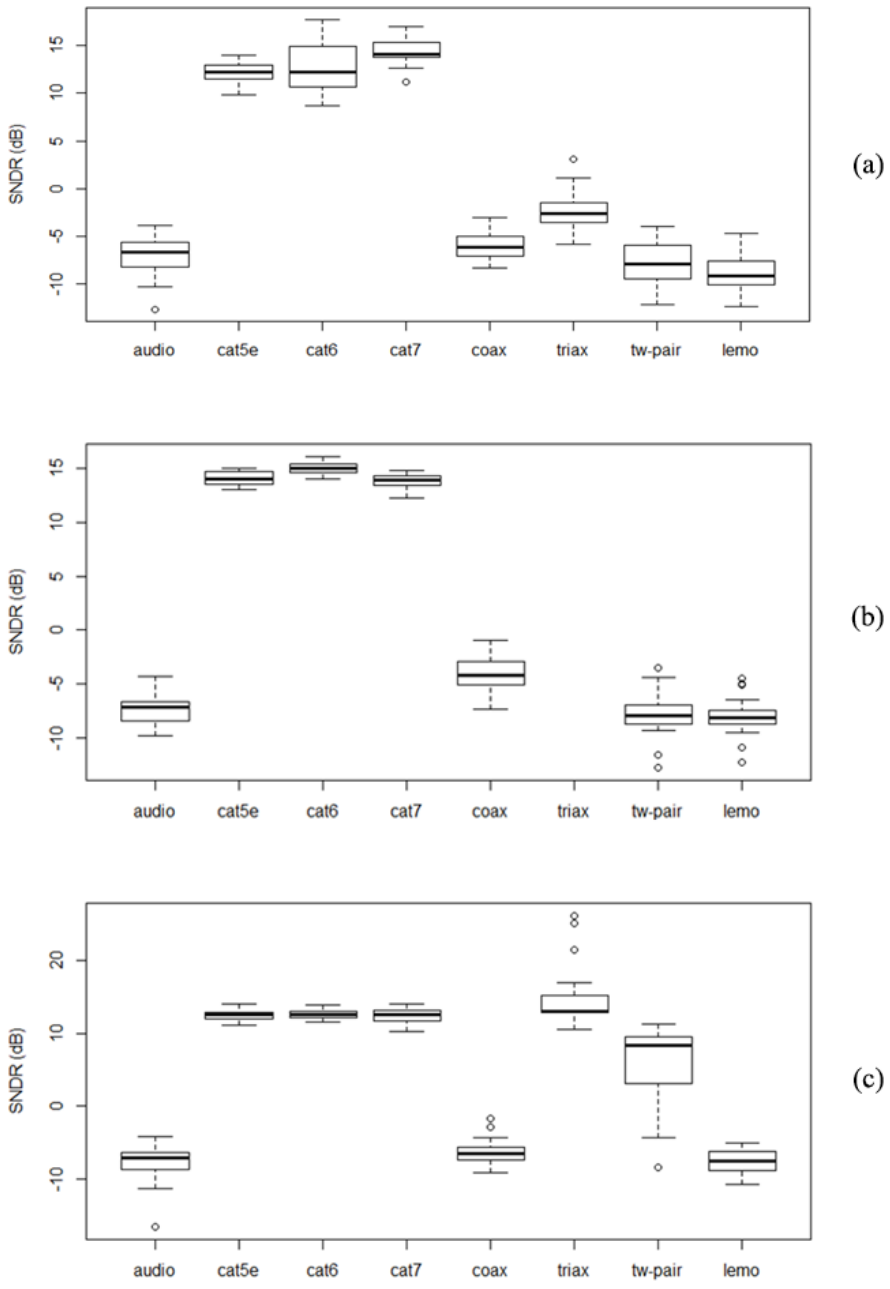

Figure 16: Boxplots of SNDR for 25 measurements with each cable placed a) parallel, b) perpendicular, and c) coiled under the 500 kV power line. The sensor is removed and a low SNDR indicates less 60 Hz penetration of the cable.

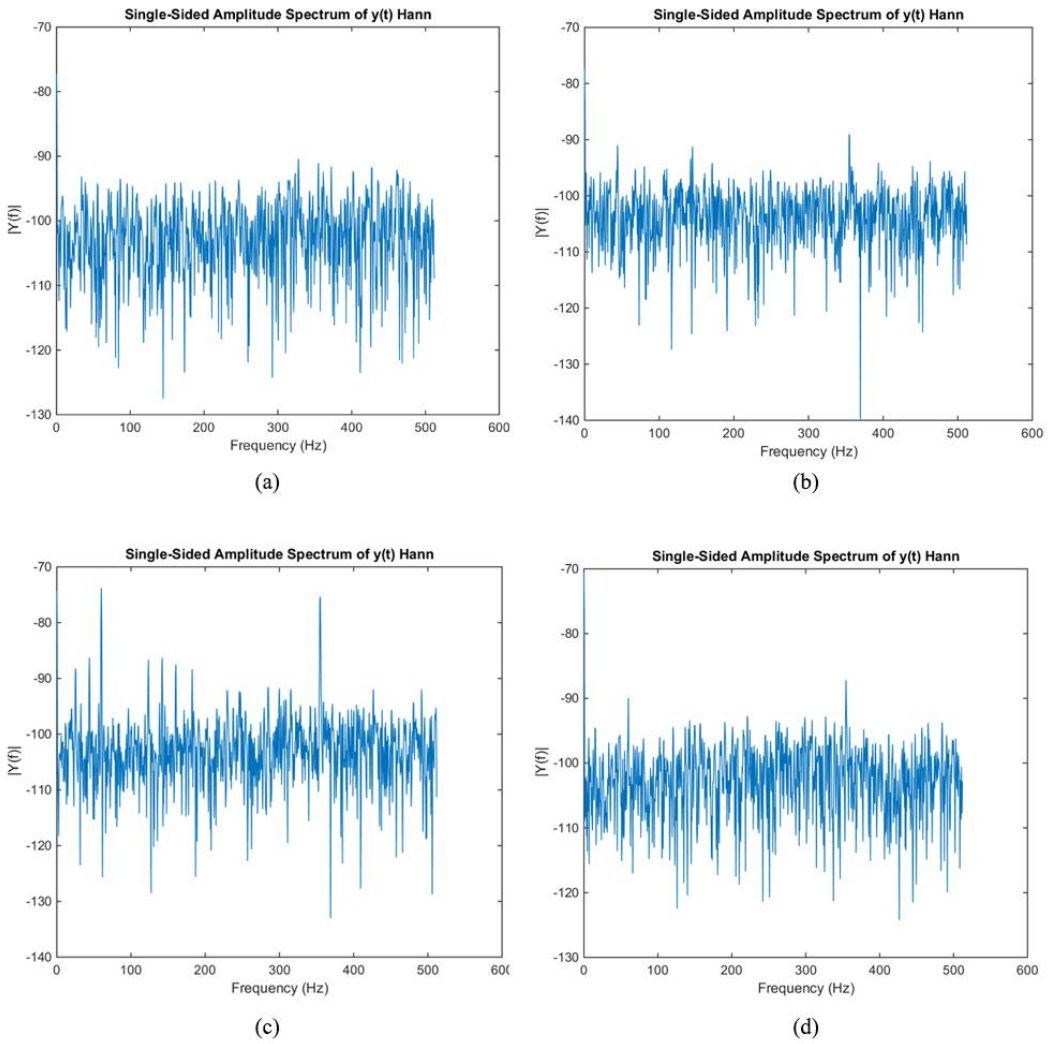

Figure 17: Single-sided amplitude spectra of transient signals coupled into a shielded twisted pair cable under 500 kV power line with a ground at a) pre-amplifier, b) data acquisition unit, c) both at pre-amplifier and data acquisition unit with the shield sharing the signal path, and d) with differential signaling where the ground loop flows only through the shield.

Next, various grounding configurations were tested for audio, twisted pair and LEMO cables. The cables were placed directly under and parallel to the 500 kV power line. Typical spectra of the transient signal are shown for the shielded twisted pair cable, Figure 17. With a single ground at the pre-amplifier, there is no noticeable penetration of 60 Hz or any other frequency above the ground floor. When a single earth ground is placed at the

data acquisition unit, there is still no 60 Hz signal present, but three frequency spurs extend approximately 10 dB above the noise floor. However, when both grounds are present with the shielding sharing the ground side of the signal path, there is substantial 60 Hz penetration along with numerous strong harmonics and other frequencies. Finally, fully differential signaling was implemented where both grounds are in place but the twisted pair

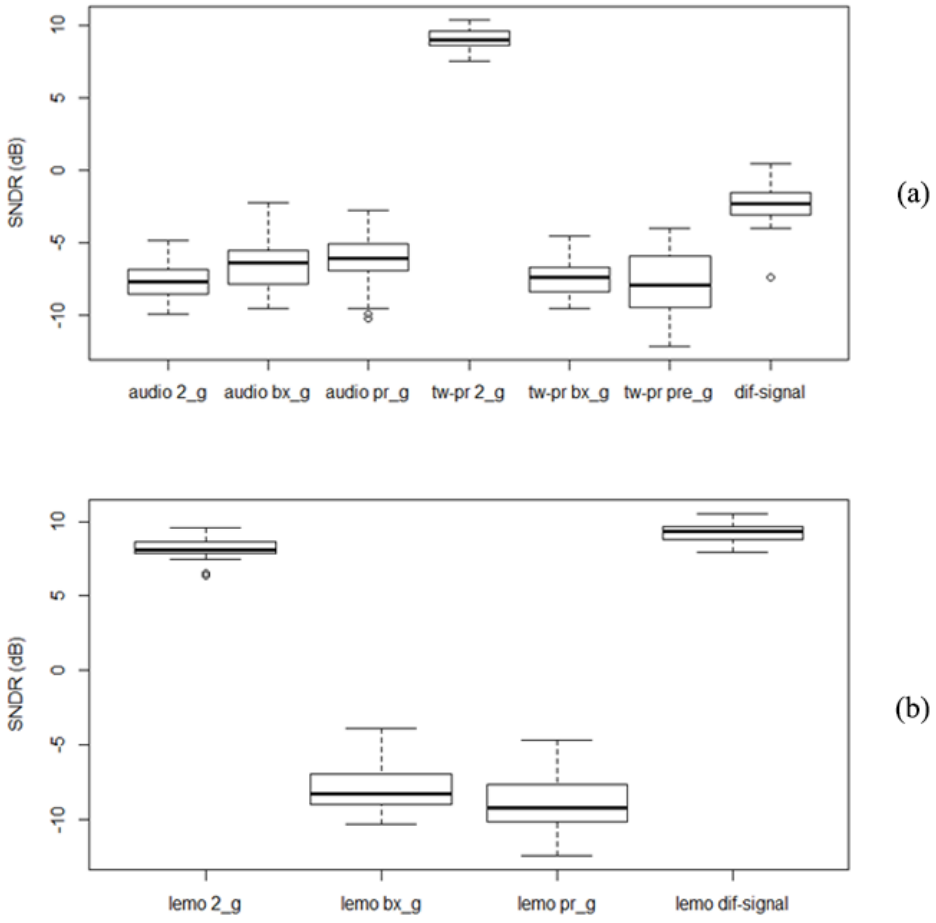

Figure 18: SNDR boxplots for audio, shielded twisted pair and LEMO cables with various grounding configurations. '2_g' indicates two earth grounds at both the pre-amplifier and the data acquisition unit, 'bx_g' indicates one ground at the data acquisition unit, 'pr_g' indicates one ground at the pre-amplifier, and 'dif-signal' indicated differential signaling where the ground loop flows only through the shield. These measurements were made under a 500 kV line.

carrying the signal path is completely separate from the ground loop through the shield. The spectrum is much improved with reduced 60 Hz penetration and reduced frequency spurs, however the spectrum is still not as quiet as either case with a single earth ground.

The boxplot of the signal to noise ratios for the audio, twisted pair and LEMO cables are shown in Figure 18 for the various grounding configurations. The lowest 60 Hz signal penetration occurred with a single earth ground at the pre-amplifier or the data acquisition unit for the twisted pair and LEMO cables. However, the SNDR for the audio cable was roughly the same even for two earth grounds.

4.3.1 13.8 kV Power Line

A second set of experiments were conducted with the cables placed directly under and parallel to a 13.8 kV power line with the sensor disconnected. The system was

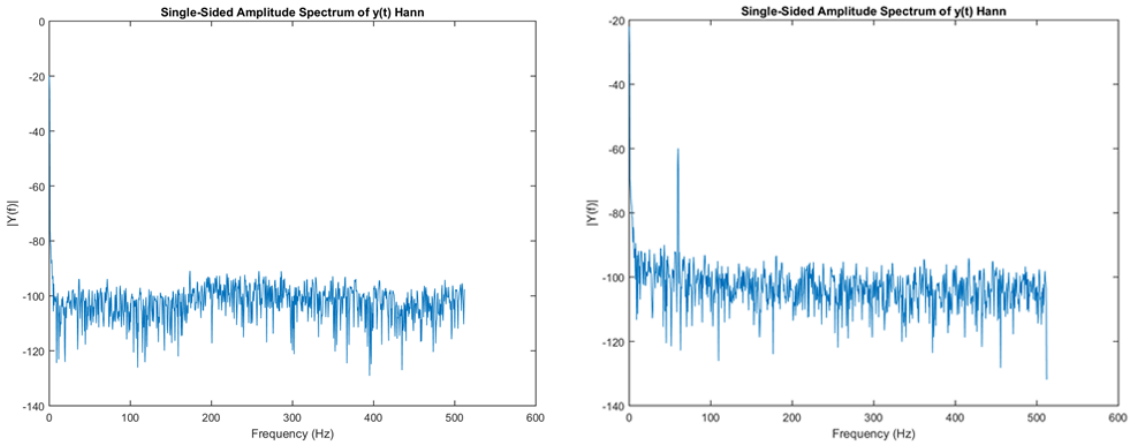

(a) (b)

Figure 19: Single-sided amplitude spectra of transient signals coupled into a) LEMO and b) audio cables under 13.8 kV power lines.

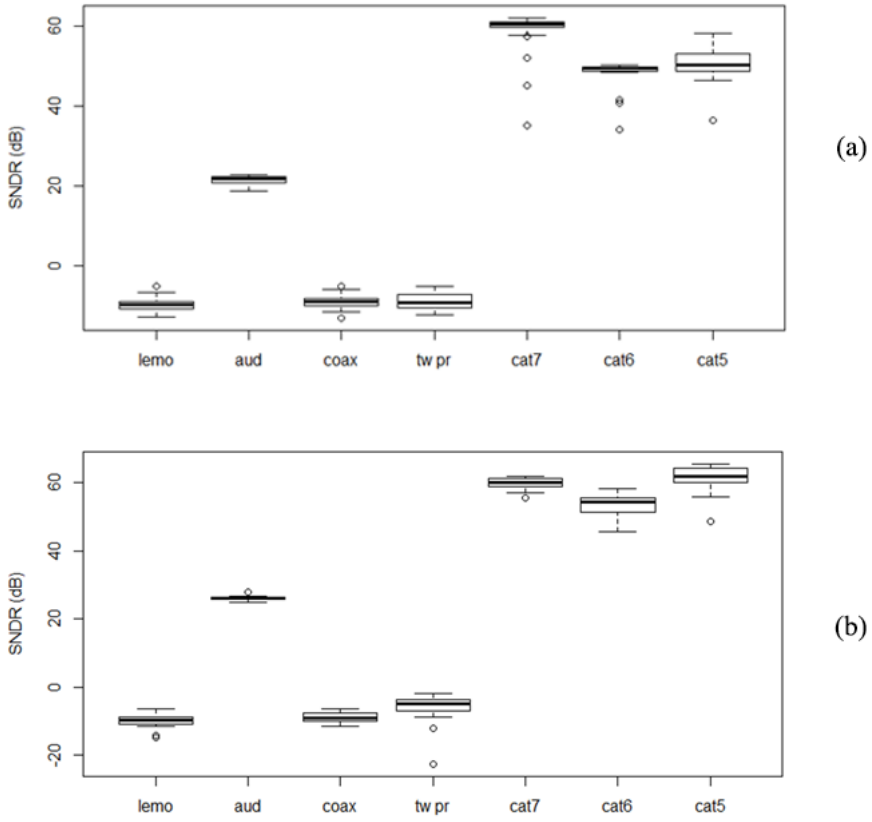

Figure 20: Boxplots of SNDR for 25 measurements with each cable placed a) parallel, and b) perpendicular under the 13.8 kV power line. A low SNDR indicates small penetration of 60 Hz fields.

grounded to earth only at the preamplifier. Typical FFTs of the transient signal for the LEMO and audio cables show negligible 60 Hz signal for LEMO but significant 60 Hz signal for the audio cable, Figure 19. Again, comparing the SNR for all of the cables with box plots, Figure 20a, the best performing cables were LEMO, coax and twisted pair. A similar result was obtained when the cables were placed perpendicular to the power line.

Various grounding configurations were then tested for the LEMO cable. The cables were placed directly under and parallel to the 13.8 kV power line. For this measurement,

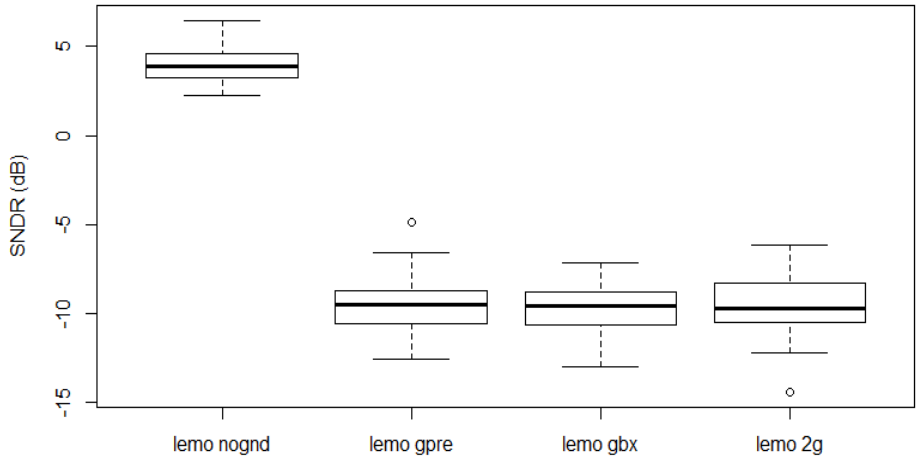

Figure 21: SNDR boxplots for the LEMO cable with various grounding configurations. ‘2g’ indicates two earth grounds at both the pre-amplifier and the data acquisition unit, ‘gbx’ indicates one ground at the data acquisition unit, ‘gpre’ indicates one ground at the pre-amplifier, and ‘nogndʼ indicated no earth ground. These measurements were made under a 13.8 kV line.

there was no detectable difference in the SNDR for a single ground or two grounds forming a ground loop. However, the importance of having an earth ground is clearly seen by the approximately 15 dB increase in 60 Hz signal penetration when the system ground was not connected anywhere to earth, Figure 21.

Chapter 5

FIRST GENERATION ELECTRIC FIELD IMAGER

Thus far, the primary focus has been on the characteristics of electric field sensors, specifically the D-dot sensor. This chapter demonstrates how those sensors were arrayed to create the first-generation electric field imaging system. The results pinpointed key functional aspects of the imaging system that were corrected in subsequent generations.

5.1 Gen I Imager

The imaging system is comprised of three main hardware components: 1) the D-dot array, 2) multiplexing unit, and 3) lock-in amplifier. Additional equipment, as well as custom software drivers, is needed for designing and running a test setup but these three components cover the core functions.

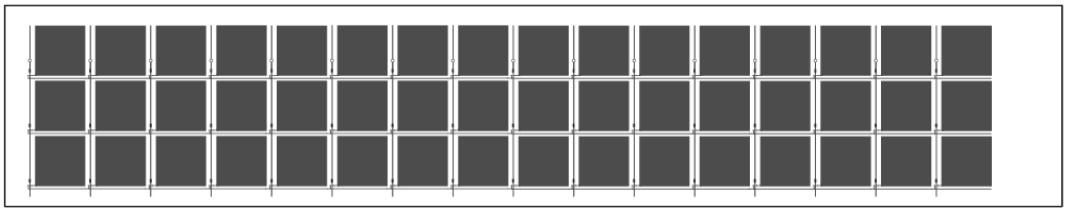

Figure 22: Original layout of a two-dimensional D-dot sensor array fabricated on a two-layer PCB. Although a two-dimensional layout, it was first utilized as a one-dimensional array.

5.1.1 The D-dot Array

The D-dot array was fabricated on a PCB in which each sensor head, i.e. pixel, was simply a 1 cm x 1 cm coating of the top layer metal. The board, Figure 22, was originally intended to be used as a two-dimensional 3 x 16 active matrix array. However, to temporarily forgo the longer process of a third-party mounting small access transistors into the active matrix architecture, read lines were initially connected directly to just the first row of pads. While this effectively reduced the board to a one-dimensional array, it allowed for quick preliminary measurements to verify key theoretical hypotheses including the "Wire over a D-dot" model from Chapter 2.

As noted in previous chapters, the D-dot sensor uses a transimpedance amplifier to hold the top receiving plate to a virtual ground and amplify the signal to a readable level. For Gen I, all 16 D-dot sensors were multiplexed to one low-noise DLPCA 200 transimpedance amplifier [54]. Each pad was directly soldered to unshielded read lines which were then connected to their respective channels into a multiplexer. It should be noted that this multiplexer must be analog. Aside from the fact that a digital multiplexer only outputs a high or low voltage, it is unidirectional and would thus not be able to hold the plate to a virtual ground.

5.1.2 The Multiplexing Unit

Each D-dot sensor signal is read individually through a multiplexing unit. Most of the experiments described in this dissertation used the Agilent 34921A multiplexer, an add-

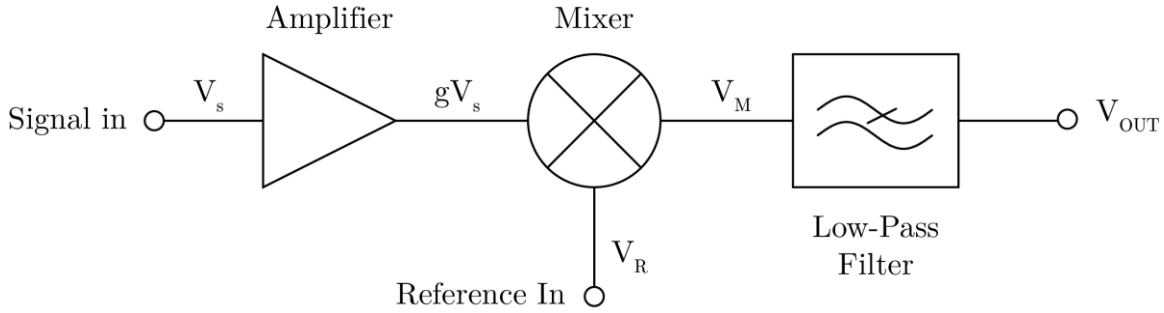

Figure 23: Diagram of a simplified one-channel lock-in amplifier.

on to the Agilent 34980A Multifunction Switch/Measure unit. This module uses mechanical switches and can be operated manually or automated [57]. The signal output from the multiplexer must then be processed to isolate the signal of interest. This is accomplished through a lock-in amplifier to attain measurable information.

5.1.3 The Lock-in Amplifier

The lock-in amplifier, extracts the component of the signal corresponding to a particular frequency of interest with a high SNR. This is achieved by first multiplying the signal with a sinusoid at a reference frequency and its quadrature to demodulate the signal to DC. It is then passed through a low-pass filter (within a bandwidth of one to a few Hz) to extract the signal strength as a scalar value. This high SNR, analog method dramatically increases the probability of detection of very weak signals which would otherwise be buried in noise. The majority of the experiments in this dissertation utilized the Stanford Research SR830 lock-in amplifier [58].

To better understand the mechanism behind the lock-in amplifier, we can first observe the simpler single-channel lock-in amplifier, Figure 23. The input signal

$$V_S = K\cos\ 2\pi ft + \phi_S \qquad (5.1)$$

and reference signal

$$V_R = \cos\ 2\pi ft + \phi_R \qquad (5.2)$$

are multiplied together by a mixer

$$\begin{aligned} V_M &= K\cos\ 2\pi ft + \phi_S\ \cos\ 2\pi ft + \phi_R \\ &= \frac{1}{2}Kg\ [\cos\ \phi_S - \phi_R\ + \cos(2\pi 2ft + \phi_S + \phi_R)] \end{aligned} \qquad (5.3)$$

The output is composed of two components: an element at a frequency of zero (DC) and an element at twice the reference frequency. The low-pass filter then removes the latter term leaving

$$V_{out} = \frac{1}{2}Kg\cos\ \phi_S - \phi_R \qquad (5.4)$$

The output, Equation 5.4, is proportional to the signal amplitude, K. This is also under the assumption that the reference and the input signal are perfectly in phase, i.e. $\phi_S = \phi_R$. However, this is hardly ever a safe assumption to make, even within highly controlled environments, and will lead to misaligned calculations of the signal strength.

To address the phase shift, robust lock-in amplifiers utilize two mixers, Figure 24. One mixes the signal with the reference while the other mixes the signal with the quadrature of the reference, i.e. the reference signal with a 90-degree phase shift.

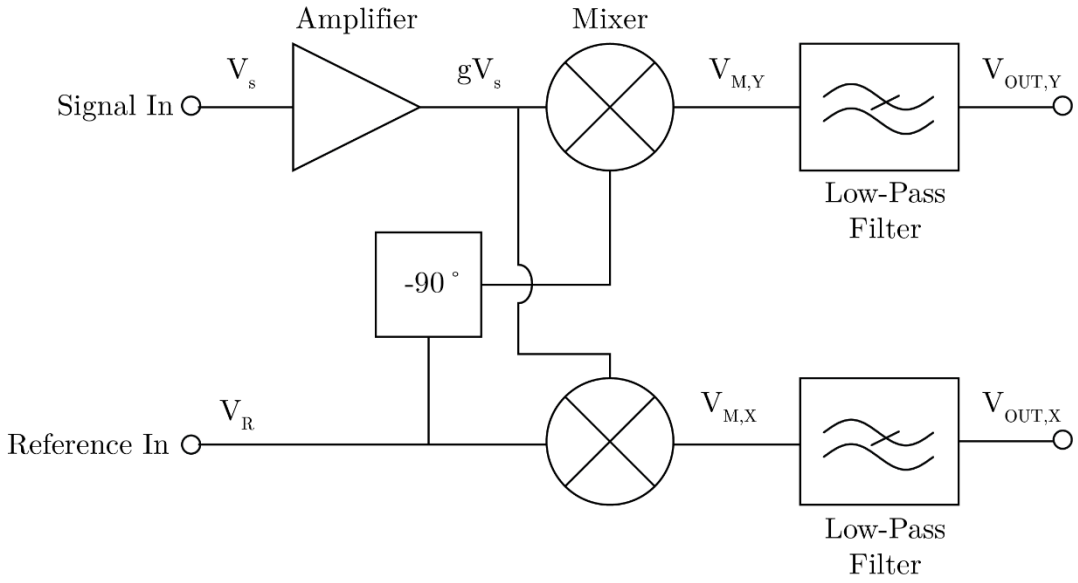

Figure 24: Diagram of a simplified dual lock-in amplifier.

Following a similar derivation, the two outputs between the reference and its quadrature are

$$V_{out,X} = \frac{1}{2} Kg \cos(\phi_S - \phi_R) \qquad (5.5)$$

$$V_{out,Y} = \frac{1}{2} Kg \sin\ \phi_S - \phi_R \qquad (5.6)$$

Taking advantage of the trigonometric property $(\sin\ ^2 + \cos\ ^2 = 1)$, both outputs can be squared, summed, and square rooted to yield

$$V_{out} = \sqrt{V_{out,X}^2 + V_{out,Y}^2} = \frac{1}{2} Kg \qquad (5.7)$$

which will always be proportional to the strength of the signal of interest regardless of phase shift.

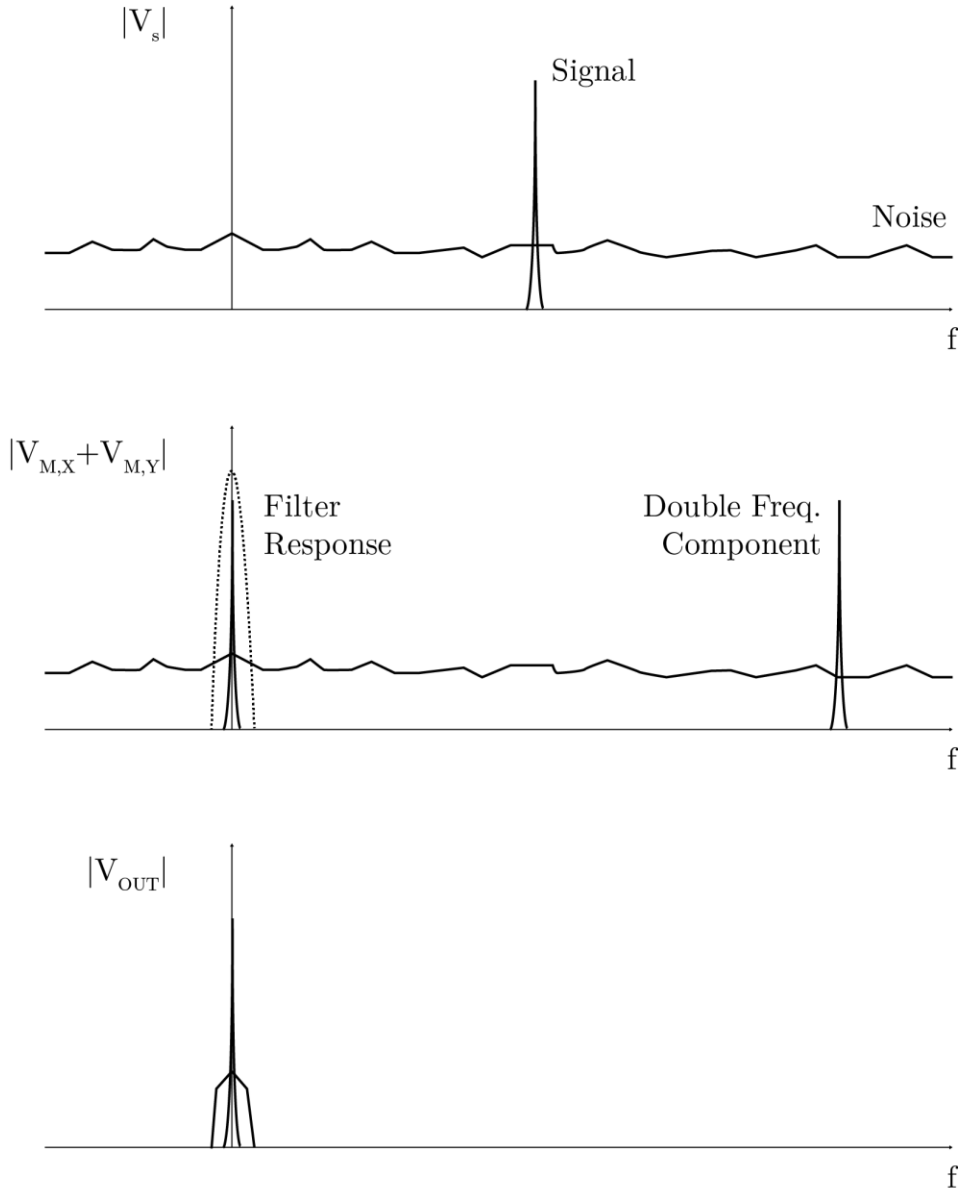

Figure 25: Diagram showing the spectra of various signals at different stages of the lock-in amplifier.

The low-pass filter not only retrieves the signal of interest but also eliminates any components within the small band around the signal, removing a significant amount of noise, Figure 25. If spikes other than the double frequency component were present, they would dramatically distort the signal without the low-pass filter.

5.2 Test Setup

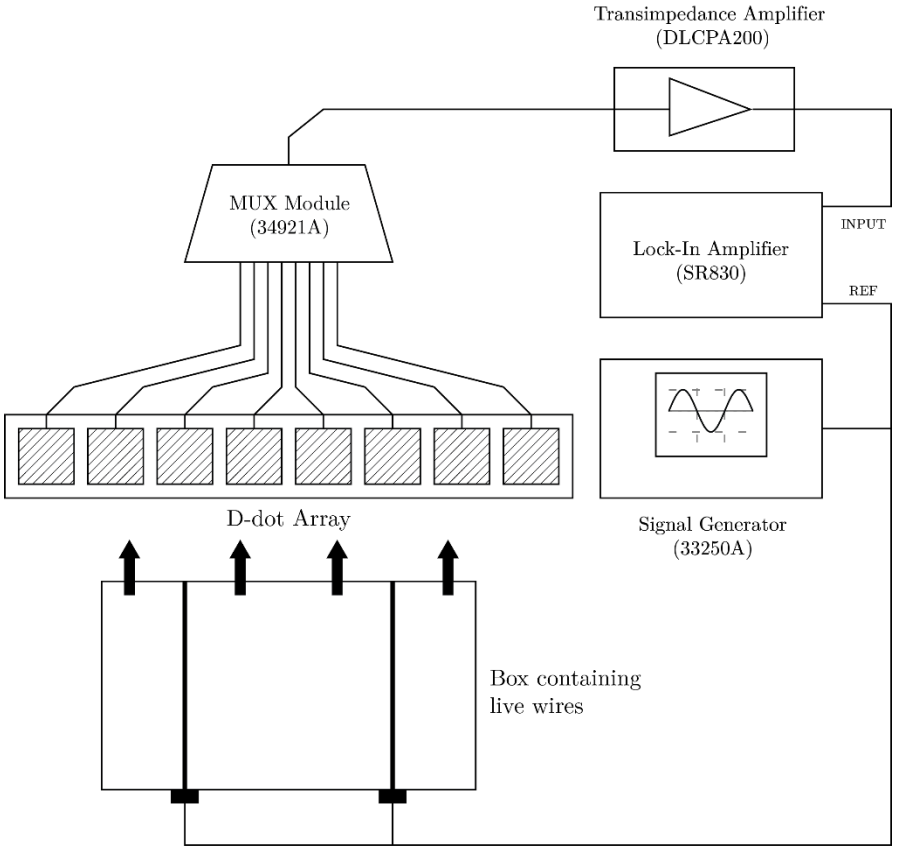

Figure 26: Diagram of the one-dimensional array test setup.

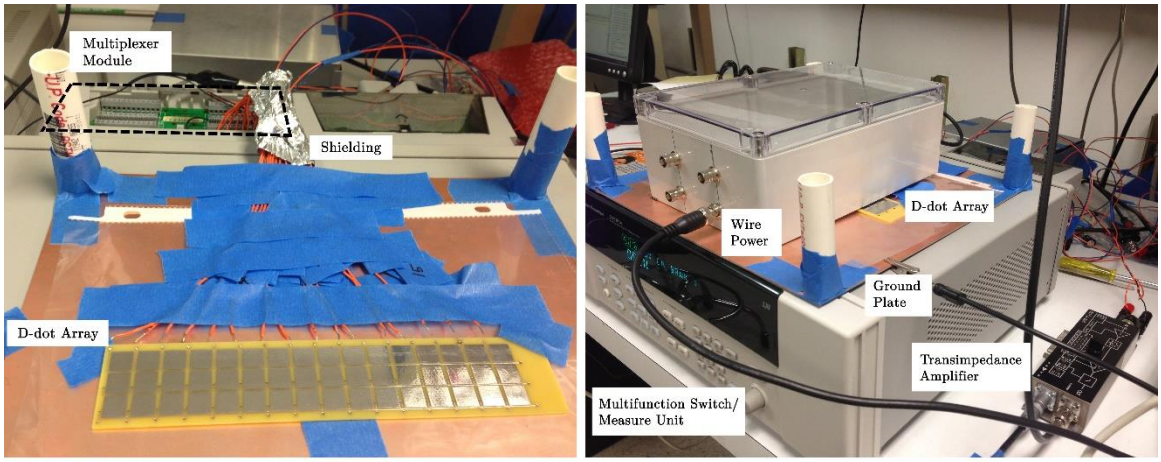

Figure 27: (a) Close-up photo of the D-dot sensor array in a one-dimensional configuration. (b) Photo of array with active wires and amplifying/readout circuity.

The first set of experiments concerned imaging the cross-sectional electric fields of two parallel 16-gauge wires charged with a 20 Vpp AC signal at both 97 and 970 Hz. Aside from being VLF, 97 Hz was chosen because it is a prime number and is unlikely to interfere or compound with environmental fields such as the 60 Hz utility frequency. The value 970 Hz is then simply an easy-to-calculate multiple of 97 Hz, allowing for quick verification of theoretical calculations, namely that the signal strength is directly proportional to frequency.

The signals were generated with an Agilent 33250A Function/Arbitrary Waveform Generator [56]. While the signal from this signal generator is not as pure as the analog Krohn-Hite 4402B [53], it served sufficiently as these experiments focused on the main signal of interest and did not require the ultra-low noise conditions described in Chapter 3. Furthermore, the signal generator was split to the lock-in amplifier to provide the reference frequency, Figure 26.

The two-wire setup was ideal for a one-dimensional array since it was isotropic in one dimension and would also allow for characterization of multi-wire setups. The wires were fashioned inside a plastic box 5 cm apart from one another and 2 cm above the array. The wires were directly hovering over approximately the 7^{th} and 11^{th} pixel from the left. A plastic box was specifically chosen since the material would have minimal attenuation effects, particularly at VLF, allowing the fields to effectively penetrate the enclosure.

5.3 Theoretical Results

Using both the electrostatic principles covered in Chapter 2 and ANSYS simulations, theoretical models were built. For simplicity, we will begin with a quick review of the derivation for a single wire, which can then be extrapolated to multi-wire scenarios.

5.3.1 Single Wire Over D-dot

Equation 2.28 demonstrated how the signal strength of the D-dot sensor is directly proportional to the frequency and voltage amplitude of the signal in the wire as well as the area of the D-dot sensor head itself. The cross-sectional electric field distribution along one axis on the surface of the plate was also derived in Equation 2.33. The distributions for wires at increasing heights are graphed in Figure 28.

This model assumes that there is one large D-dot sensor head and that the calculations of the electric field strength on various points on the D-dot sensor are derived

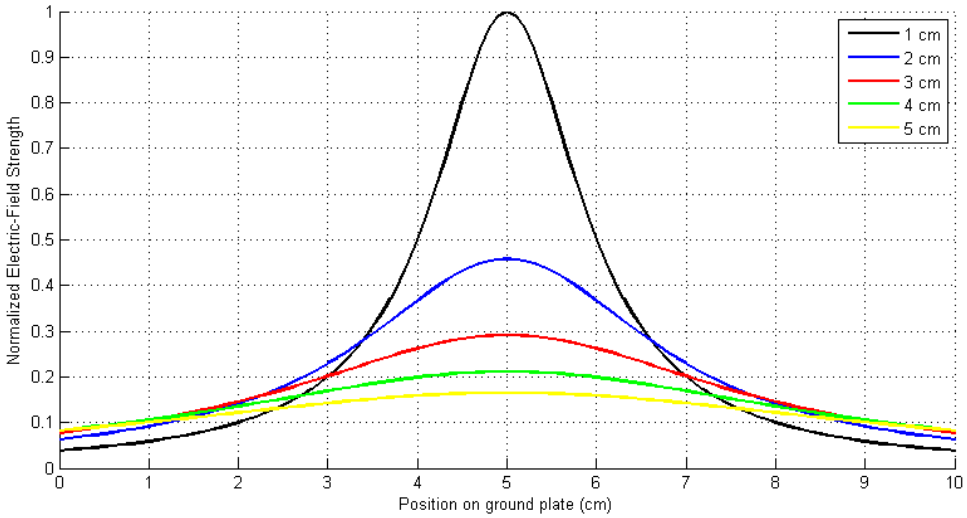

Figure 28: Normalized electric field distributions for wires at various distances from the D-dot sensor.

from an infinitely small area of dA. If the sensor head is, instead, discretized into a grid of pixels in which the integral electric field strength in each pixel is binned, we can take one row of the calculations and connect it to the results of the test setup. This does imply that the signal strength for each sensor will be smaller since it is proportional to the electrode area, and so it must be assured that the area does not become too small where it lies below the noise floor of our instrumentation.

5.3.2 Multiple Wires Over D-dot

Mathematically determining the resolution possible by calculating the electric field from multiple wires above a ground plane is another calculation of interest. This derivation is more nuanced because each line charge also depends on the voltage on all of the other

wires. A similar derivation has already been conducted to calculate the electric field around high-voltage power lines [59].

In the scenario of two wires above a ground plane, Figure 29, the voltage on line k, $V_{line,k}$, is a function of both line charges Q_k and Q_m.

$$V_{line,k} = p_{kk}Q_k + p_{km}Q_m \qquad (5.8)$$

Likewise, the voltage on line m, $V_{line.m}$ is a function of both line charges.

$$V_{line,m} = p_{mk}Q_k + p_{mm}Q_m \qquad (5.9)$$

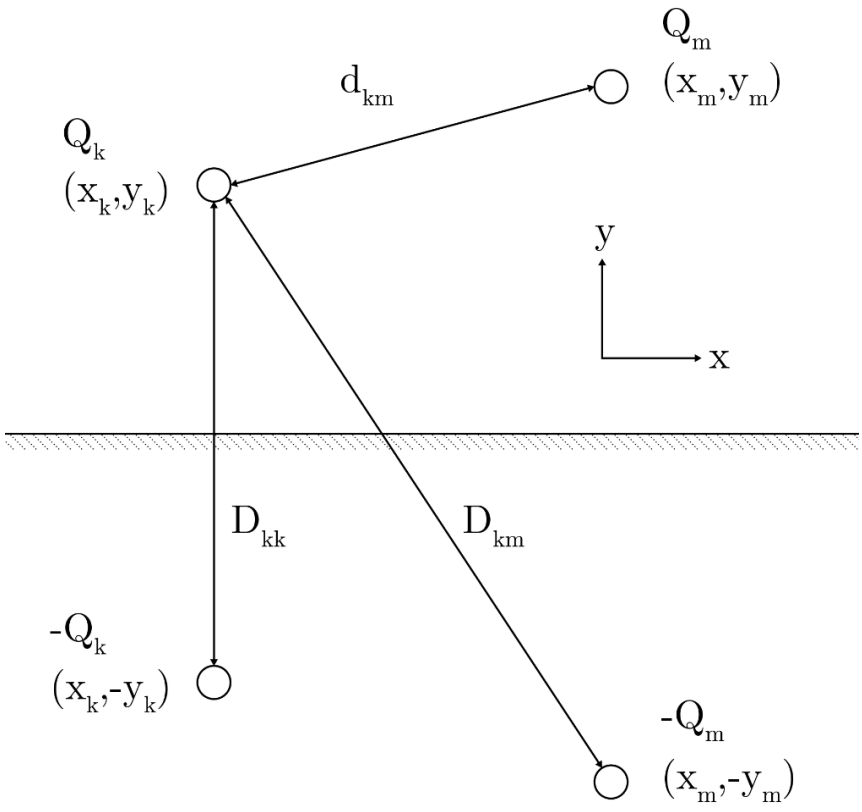

Figure 29: Diagram to determine the electric field for two wires above a ground plane.

The distance between conductor i and the image conductor j is D_{ij} and the distance between two real conductors i and j is d_{ij}. When i equals j, d_{ij} is the wire radius.

These relations can be derived from electrostatics and can be extended to any number of wires above a ground plane. The simultaneous equations become the matrices and vectors

$$p_{ij} = \frac{1}{2\pi\epsilon} \ln\left(\frac{D_{ij}}{d_{ij}}\right) \qquad (5.10)$$

$$d_{ij} = a \quad \text{when} \quad i = j \qquad (5.11)$$

where $\mathbf{V}_{line}$ and $\mathbf{Q}$ are the line voltage and line charge vectors respectively and $\mathbf{P}$ is the potential coefficient matrix.

$$\mathbf{V}_{line} = \mathbf{PQ} \qquad (5.12)$$

The line charges are determined by inverting the potential coefficient matrix:

$$\mathbf{Q} = \mathbf{P^{-1}V}_{line} \qquad (5.13)$$

Once the line charges are determined, the electric field at point x is the vector sum of the electric fields from all wires including the image wires:

$$\mathbf{E}_x = \sum_n \frac{\mathrm{Q}_n}{2\pi\epsilon \mathbf{r}_{nx}} \qquad (5.14)$$

The equations were simulated and plotted with MATLAB to visualize the field strengths, Figure 30. The simulations covered a 20 cm x 20 cm area in which two wires

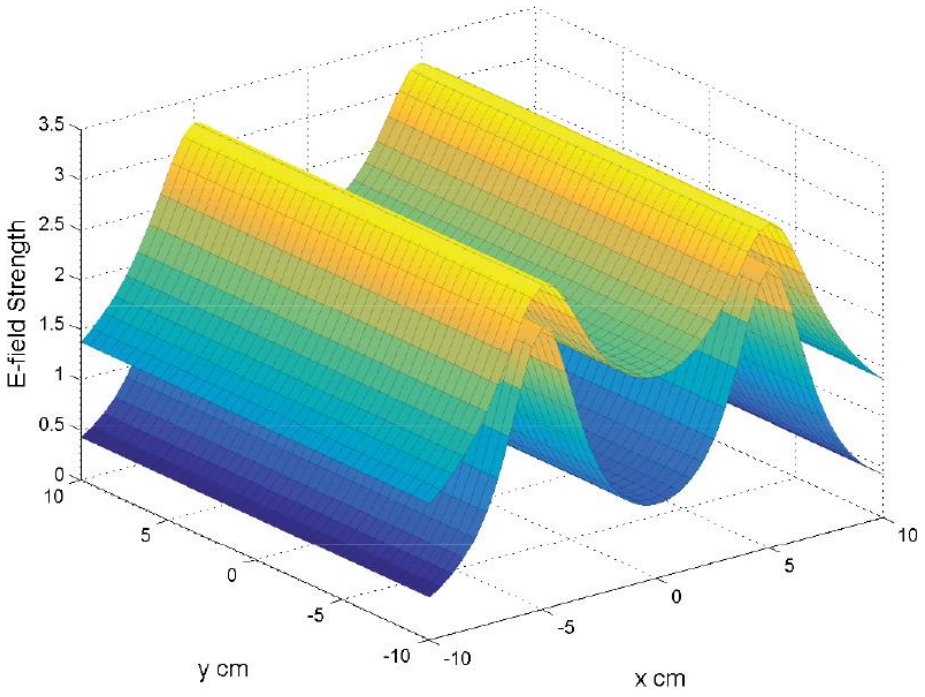

Figure 30: Electric field distributions of two wires 10 cm apart an 2 cm above a ground plane. The multiple wire calculation (top) is compared to the sum of the independent fields (bottom).

were separated 10 cm apart from each other. The wires were 0.1 cm in diameter and energized with 10 V.

When wires are relatively far apart, the diagonal of the charge coefficient matrix is dominant. Therefore, it is a reasonable approximation, in this case, to treat the wires independently such that the total electric field is the independent average sum of the electric fields from each wire, especially in areas local to the peak and when finding general shape to detect wires.

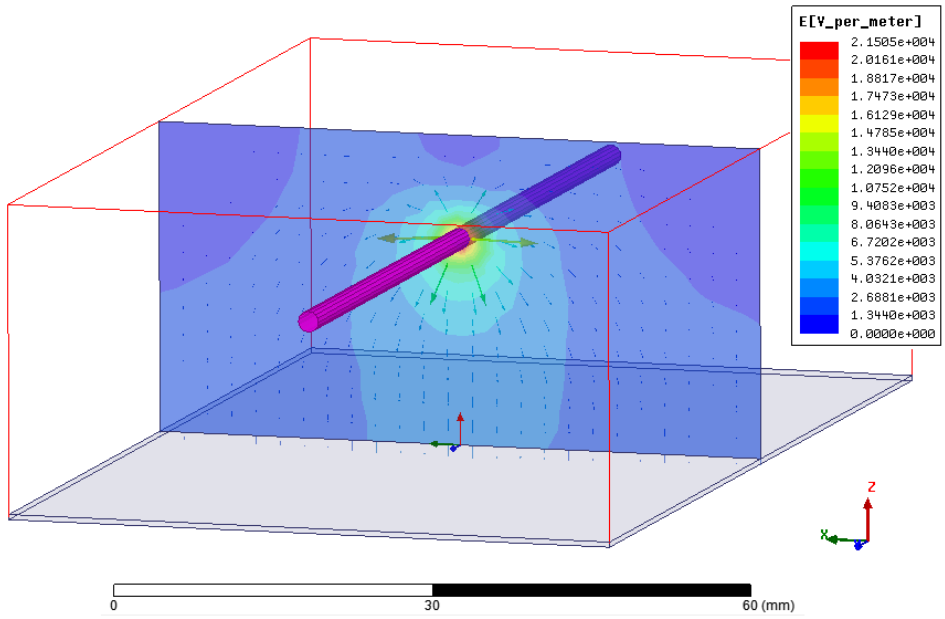

Figure 31: A cross-sectional electric field vector field and magnitude heatmap of a wire over a ground plane modeled in ANSYS Maxwell 15.0.0.

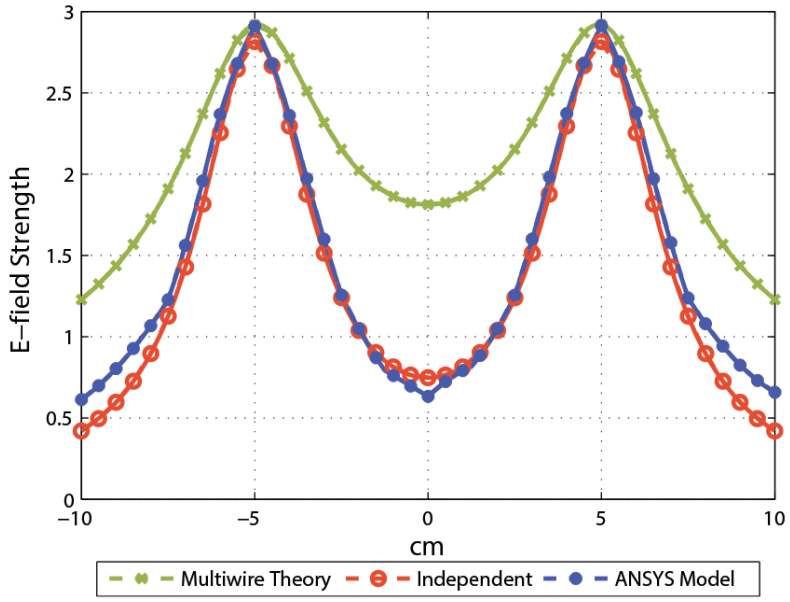

Figure 32: Comparison of cross-sectional electric field strengths when using the multi-wire theory, independence assumption approximation, and ANSYS Maxwell simulations.

5.3.3 ANSYS Simulations

The setup was modeled in ANSYS Maxwell 15.0.0, Figure 31, to verify the behavior of the electric field through a reliable physics simulation software package. For a single wire, the electric field strength was consistent with the analytical model and matched almost perfectly to the distribution of Equation 2.33.

For a multiple wire setup, simulations suggested it was a reasonable estimation to treat each wire independently. Therefore, the final electric field distribution would then be a summation of the electric field contributions of each wire if isolated. This assumption somewhat surprisingly yielded a better match to the ANSYS results than even the multiple wire derivation, Figure 32. The simulation results were further supported by experimental measurements, covered in following sections.

5.4 Experimental Results

The resulting curves from the first set of experiments were far from the expected output, Figure 33. However, there was a high level of confidence that the fields were indeed being measured since there was a slight resemblance of peaks where it was expected. More importantly, the frequency and voltage relationships, derived in Equation 2.28, were consistent with the results. The 970 Hz wire produced a signal almost exactly 10 times greater than the 97 Hz wire. Similarly, a 20 V wire produced a signal twice as strong as a 10 V wire.

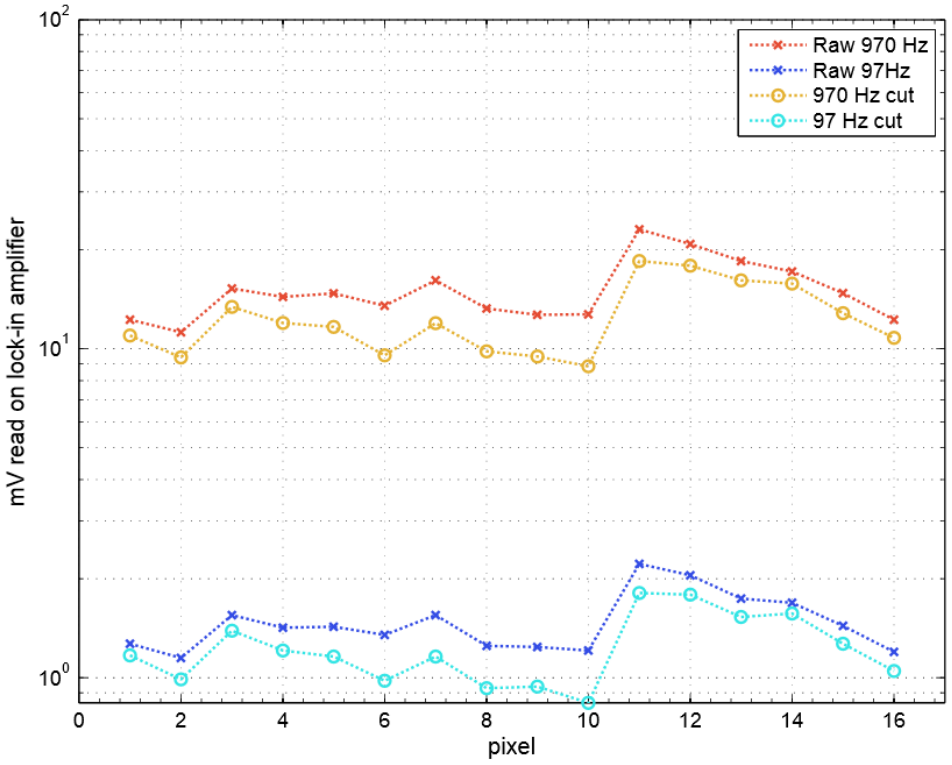

Figure 33: Plot of initial raw data (seen with the 'x' markers) along with the array output after the readlines were cut (seen with ‘o’ markers).

Furthermore, the experiment was highly repeatable, given that the setup was not disturbed. It led to the conclusion that the array was simply very sensitive and was picking up unanticipated electric fields. The main suspected culprit was the group of wires connecting the sensor heads to the amplifier.

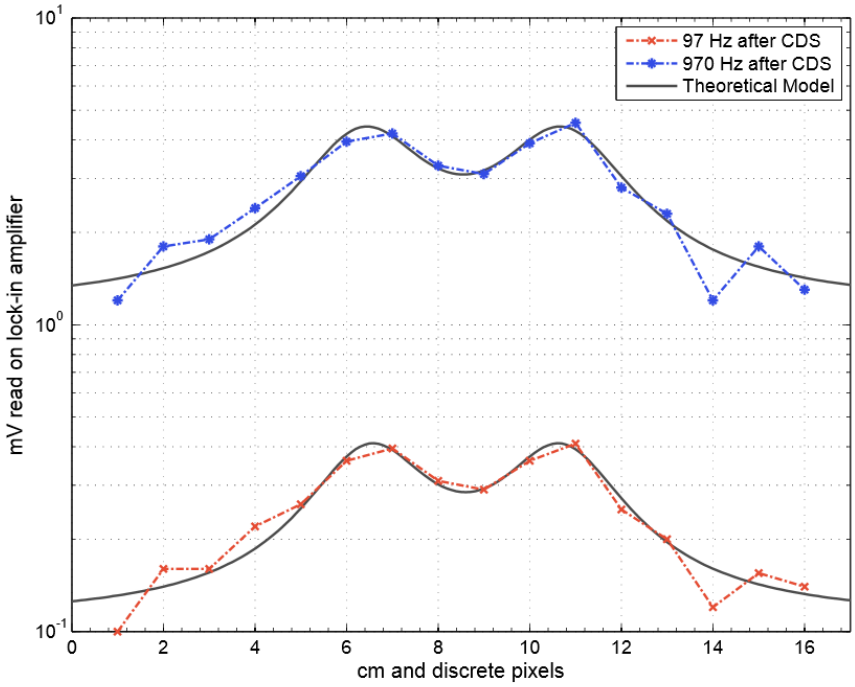

Figure 34: Plot of measurements after correlated double sampling compared to the theoretical model.

5.4.1 Correlated Double Sampling

To eliminate any potential noise from outside of the imager, the measurements were repeated with and without the D-dot sensor array. By taking the difference, only the signal directly measured from the imaging array would remain. This concept was inspired by the principles of correlated double sampling.

Since the presence of the imager itself can distort the electric fields, it was necessary to disconnect the pixels from the rest of the setup while moving as few components as possible. This was achieved by physically cutting the read lines near the pixels. A second reading was then collected.

The measurements after the wires were cut can be seen in Figure 33 and the output after correlated double sampling can be seen in Figure 34. There is clearly some offset that is collected by components outside of the D-dot array. The signal directly collected from the imaging array, however, corresponds very closely to the theoretical model, demonstrated by the clearly resolved wires.

It was concluded that a significant level of parasitic signals was obtained from any exposed connections between the sensor head to the transimpedance amplifier since in effect, the lines were extensions of the D-dot sensor head itself. In this case, there were long wires connecting the sensor heads with the multiplexer and then again from the output of the multiplexer to the amplifier. Since the wires were unshielded, the signal from the wires would capacitively couple into the read lines. This distorts the signal read at the imaging array because charge would have to be compensated for the unwanted signal in the lines which are also conductive and held at virtual ground. Further noise could also possibly be within the multiplexer box itself, though this was not explored extensively.

Any connections that stem from the output of the amplifier, however, should not have a drastic effect. This is not only confirmed by the fact that reasonable measurements were found despite not cutting any connections post-amplifier but because the output line is not held at a virtual ground and thus no compensation of charge is required. It is true that some electric flux could still couple into the output line, but with a properly shielded BNC cable, like the one used, this effect should be minimal.

Chapter 6

THE ACTIVE MATRIX 2D ARRAY (PCB)

The experimental results in the previous chapter demonstrated that the theoretical foundations of the imager were sound. Several two-dimensional counterpart arrays were then fabricated to streamline data acquisition. This chapter covers the PCB active matrix two-dimensional array in which small access transistors were mounted and connected to each pixel. It also covers ancillary features which created a more practical imaging system that did not require the correlated double sampling process.

6.1 The Active Matrix Architecture

Each D-dot sensor in the two-dimensional array had an associated access transistor to iteratively read through all the pixels when paired with a corresponding driver. The Texas Instruments CSD17381F4 N-channel MOSFET [60] was used because of its ultra-small footprint, reducing the required gap between pixels. These N-channel MOSFETS functioned in a manner similar to transistors found in dynamic random access memory (DRAM) architecture [61].

The gate of the transistor was connected to a ROW line. When a ROW line was activated with a high voltage, all of the D-dot sensors in the row then had a channel from

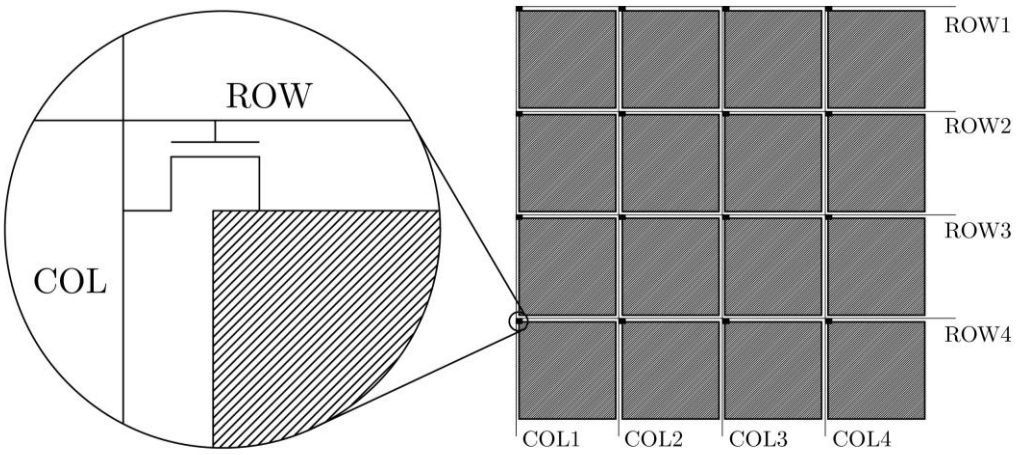

Figure 35: Diagram of the active matrix architecture with access transistors in a two-dimensional imaging array.

the sensor head (source) to a COLUMN line (drain). Each COLUMN line was iteratively read using a multiplexer and corresponding software written in MATLAB.

6.2 Dedicated Amplifiers: Cutting the Noise in Read Lines

While the Gen I imager had proved some fundamental concepts, its shortcomings made it impractical. Most notably, the electric flux was coupling into the read lines and wires had to physically be severed, rendering it a one-time-use device. Connections at the output of the transimpedance amplifier, however, should be immune from fluctuations from ambient electric fields since the output is driven by the operational amplifier to the appropriate voltage. Therefore, having the signals from the sensor head physically travel a distance as short as possible should yield a dramatic reduction in coupling of extraneous noise.

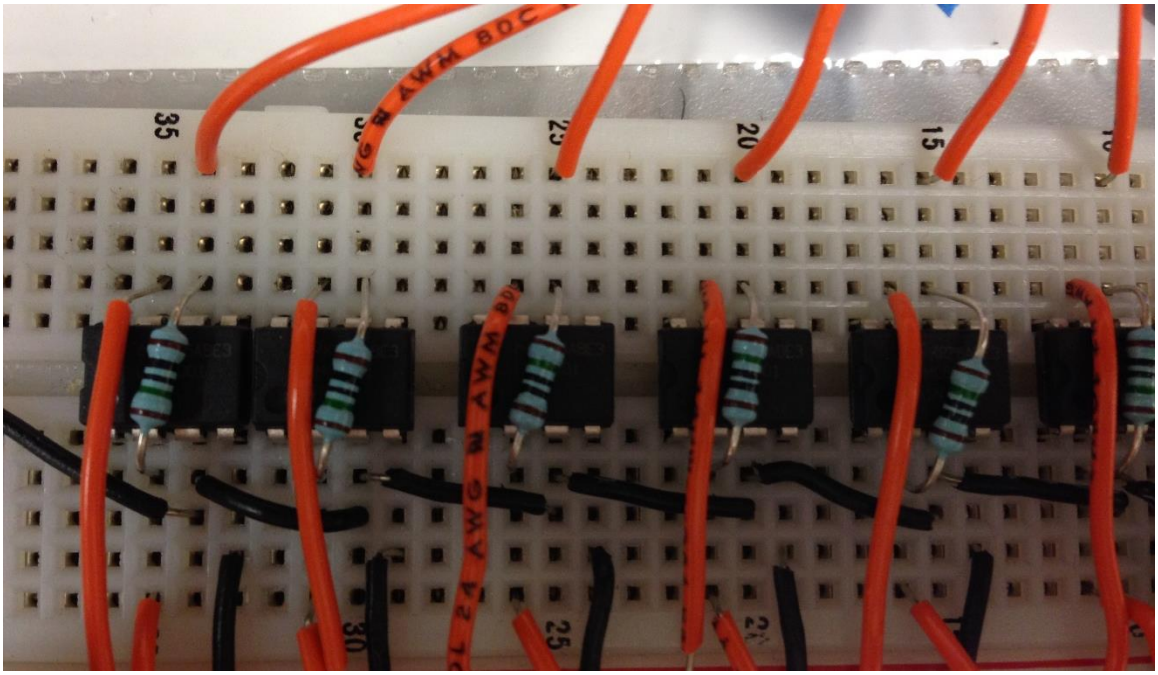

Figure 36: A close-up of the LMC6001 op-amp array.

The connection between the sensor head and the transimpedance amplifier needed to be as small as possible. However, this was difficult to do in a uniform manner when using one DLPCA 200 [54] amplifier. Instead, a 16 x 1 array of commercial off the shelf (COTS), ultra-low leakage LMC6001 operational amplifiers [62] laid on a breadboard was used, one amplifier for each column. The amplifiers were configured as transimpedance amplifiers with a 20 MΩ feedback resistors. They were arranged in a way to minimize the variance of the distance from each sensor head to its respective amplifier, Figure 36.

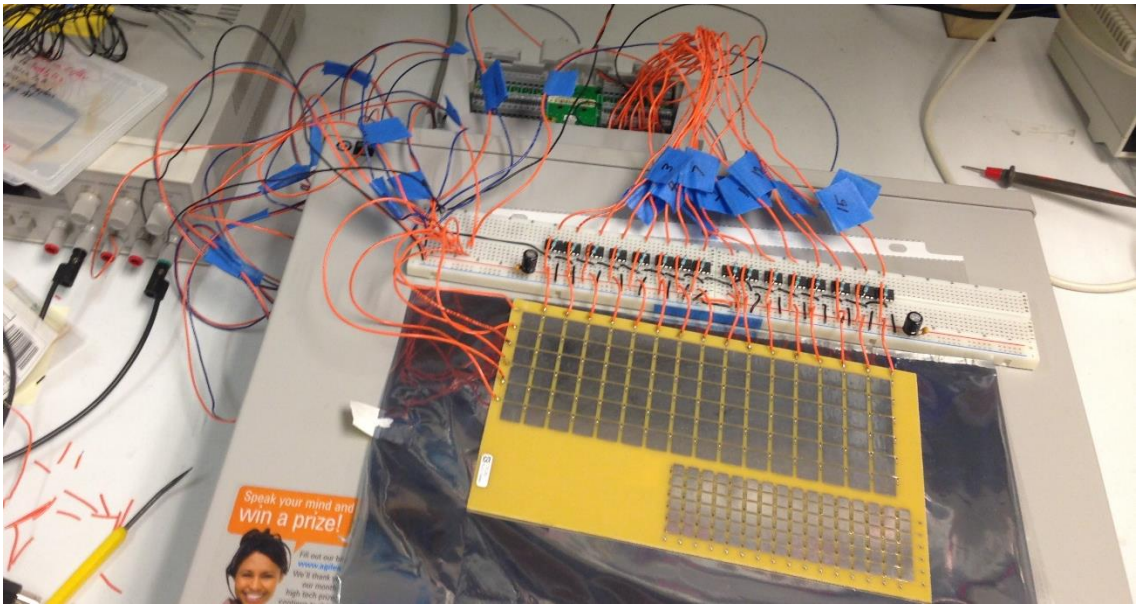

Figure 37: Image of 6 x 16 D-dot array connected to dedicated transimpedance amplifiers and multiplexing unit.

6.3 Board Layout

Two 6 x 16 D-dot arrays were assembled on a single PCB. One array was made of 1 cm x 1 cm pixels to cover larger areas while the other had 0.5 cm x 0.5 cm pixels to attain higher resolution images, Figure 37.

6.4 Test Setup

Most aspects of the test setup remained unchanged, when compared to that in the previous chapter, with two notable differences. The first was the aforementioned amplifier configuration. The second was as the mechanism added to operate the access transistors. This was done using the Agilent 34951A Digital to Analog [57] module to turn on and off

any given row of transistors with a 5 V DC signal. Once a row was activated, each column was iteratively read through the multiplexer.

6.5 Experimental Results

The arrays were capable of imaging AC electric fields from the two wires without the need of correlated double sampling. The lock-in output voltage is plotted as a function of pixel number and clearly shows two electric field peaks corresponding to the position of the wires, Figure 38. However, it was quickly realized that the imager was only imaging

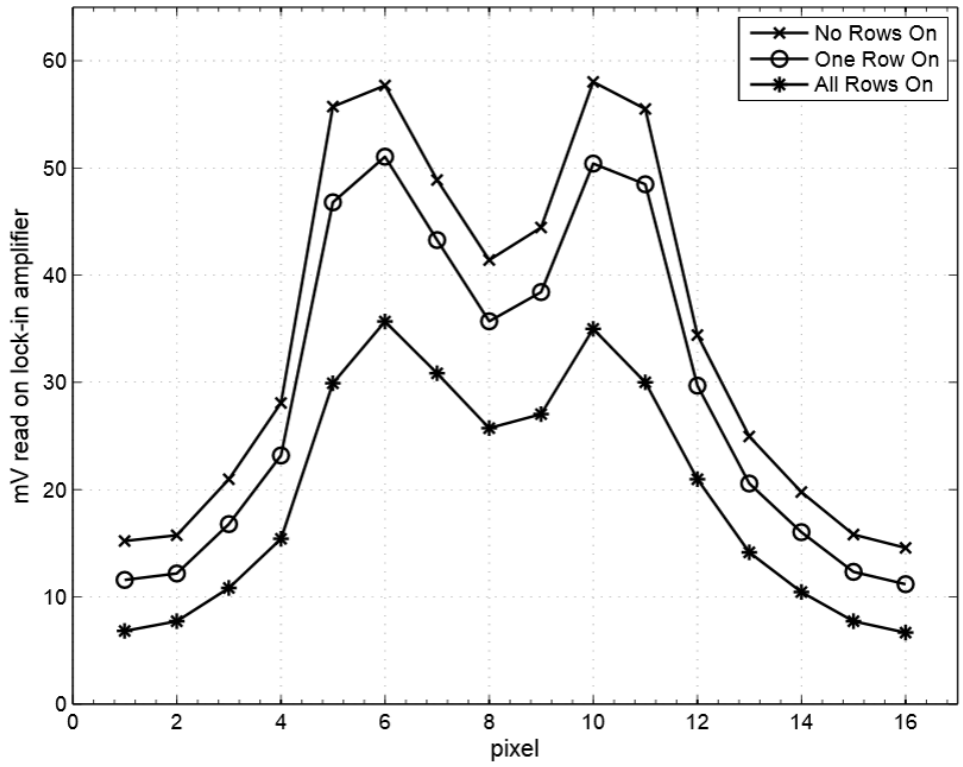

Figure 38: Electric field image obtained with the two-dimensional PCB array of two wires enerized with a 97 Hz, 20 V_{pp} signal.

in one dimension since the familiar “two-bump” image was obtained regardless of whether one row, all rows, or even none of the rows were activated.

Through SPICE circuit simulations, it was determined that even a leakage current in the nA range, typical for the silicon COTS transistors, would be negatively affect the results. Considering that our signals of interest are in the pA range, the leakage was too high to be considered “off.” Furthermore, we believe this is a fundamental and physical limitation of the intrinsic property of silicon and not a quality assurance issue.

6.6 Analysis of Results

AC current induced the D-dot sensor head, a very low impedance node, either flows through the sensor capacitance to ground or through the access transistor to the amplifying electronics, whichever impedance is less. Therefore, the off-resistance of the access transistor must be much greater than the impedance of the sensor capacitance at the frequency of interest to isolate an “off” sensor pad.

With 1 cm^2 sensor heads on a standard PCB detecting at 97 Hz, the off-resistance of the access transistor must be much greater than 600 MΩ. The off-resistance of the commercial FETs measured to only be 2-4 MΩ explaining why we observed all rows of the array to effectively be on at all times.

It is the fact that this required off resistance is so much greater that we believe it is an intrinsic limitation of silicon and that we would not be able to find any single-crystal semiconductor FET to sufficiently isolate a sensing pad from the array. Electromechanical

switches that have an air gap in the off state could prove effective, but such a device with a sufficiently small package and footprint could not be found.

Chapter 7

THE ACTIVE MATRIX TWO-DIMENSIONAL ARRAY (FLEX)

For some time, our research group had been working collaboratively with the Flexible Electronics and Display Center (FEDC) at Arizona State University. Together, there was interest in implementing an electric field imager on a flexible substrate by leveraging the in-house fabrication line. This chapter discusses the two-dimensional FLEX array that came about from this joint effort.

7.1 FEDC Thin-Film Transistor Process

The thin-film transistors (TFTs), fabricated at the FEDC and utilized for this imager, use an indium gallium zinc oxide (InGaZnO), 8 mask, low temperature (180°C) process. They have an inverted staggered tri-layer structure, Figure 39, and can be processed on flexible substrates such as metal foil and polyethylene napthalate (PEN).

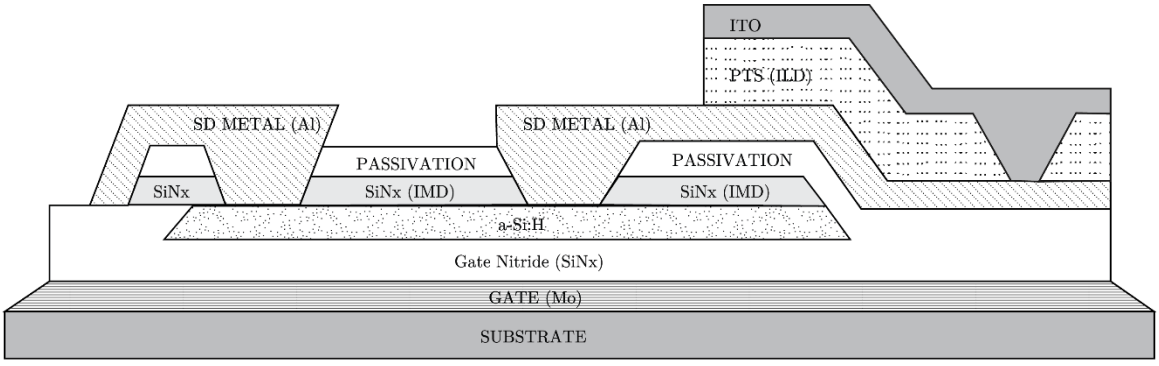

Figure 39: Basic structure of the thin-film transistor from FEDC.

Figure 40: Photographs of a wafer of flexible electronics (left) and a flexible display (right) built at FEDC.

These devices have been used to build flexible displays [63] and a variety of other flexible electronics including bio-sensors [64], x-ray radiography panels [65], [66], and backplane electronics for neutron detectors [67], [68], [69]. These TFTs are excellent low leakage switches forming an active matrix backplane [70], and so its utilization as an imaging array seemed to be a logical application. Further details of the TFT process and characteristics can be found in [71], [72], [73].

7.2 Flexible TFT Array

The motivation to develop a fully flexible imaging array is portable imaging in the field with a versatile form factor. An active matrix 4 x 4 pixel array of 1 cm^2 metallic plates was fabricated on PEN for proof of concept. The access transistors were amorphous InGaZnO TFTs with a mobility of ~20 cm^2/Vs and off-state leakage in the pA range. It was because of the amorphous InGaZnO very low leakage, that there was reason to believe that the active matrix architecture could work on FLEX, as opposed to a single-crystal material in the MOSFETS for the PCB array.

7.3 Test Setup

Many aspects of the experimental setup were very similar, if not identical, to the previous setups. The aforementioned LMC6001 operational amplifiers [62] were used. The signals were once again fed into the Agilent 34921A Multiplexer module [57] and then fed into the lock-in amplifier. Again, the two frequencies of interest were 97 Hz and 970 Hz. The voltages used however, were lower in the 1-10 V_{pp} range. The lower voltages were opted for because a wire placed directly over the sensors to accommodate the smaller array size and lower resolution, increasing the electric field strength and chance of overload.

Like the active matrix PCB, drivers were needed to operate the access transistors. When 10 V is applied to the gate to turn the transistor on, the channel resistance is approximately 100 kΩ. Negative 5 V is applied to completely turn off the transistor in which the off-resistance is approximately 10^{13} Ω with a corresponding leakage current in the range of pA. Asserting a row in the array connects the D-dot sensors in that row to the columns where transimpedance amplifiers at the base of the columns amplify the current signals.

7.4 Key Experimental Results

While a wide range of wire formations were tested, this section will provide a sample of results to exhibit the key findings. The first wire was placed a diagonal fashion

over two columns of the array, Figure 41. The goal was to see the response and ensure that pixels with no wire above them would produce little to no signal at the output.

The sensitivity of the D-dot sensor was once again recognized as it was capable of picking up even slight deviations in the height of the wire from the array. Though it is a coarse image due to the high quantization error for the relatively large pixel size, the results show how only the pixels underneath the wire have the greatest signal strength with nearby pixels possibly collecting fringing fields.

Furthermore, the close-up photo explains the disparity in signal strength such as the spike on row 3, column 2 where the wire is ~1 mm closer to the sensor head than the rest of the wire. Given that electric field strength drops 1/r, when operating so close to the D-

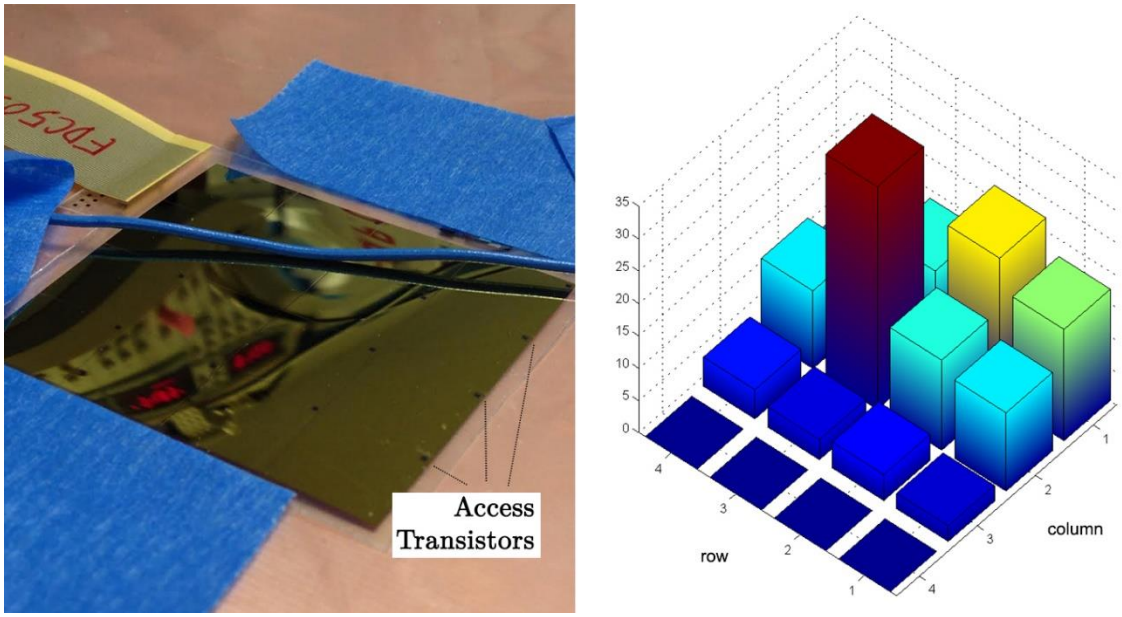

Figure 41: Close-up photo of experimental setup of flexible imager emphasizing small deviation in the height of the wire carrying 10 V_{pp} at 970 Hz (left). Histogram of corresponding output voltages (right).

dot sensor, small deviations can yield large differences. Disparities could also be accounted for the total length of wire that is covered by each pixel as it is not uniformly distributed. There is also the possible issue of pixel to pixel offset errors due to process variations, an issue that has been consistent with other arrayed electronics fabricated on the same process.

Stranded wire was also tested as opposed to solid core because it was more malleable and could more easily be laid flat over the array and hopefully smooth out the deviations in height. Figure 42 shows a much more uniform reading with the experimental run of a stranded wire over column 3. The wire, however, still could not be laid perfectly flat and may explain the kink seen in the third row. Again, the discrepancy may also be explained by pixel to pixel offset errors. Nonetheless, as a proof of concept, there is promising potential that such an imager can be implemented in a flexible form factor.

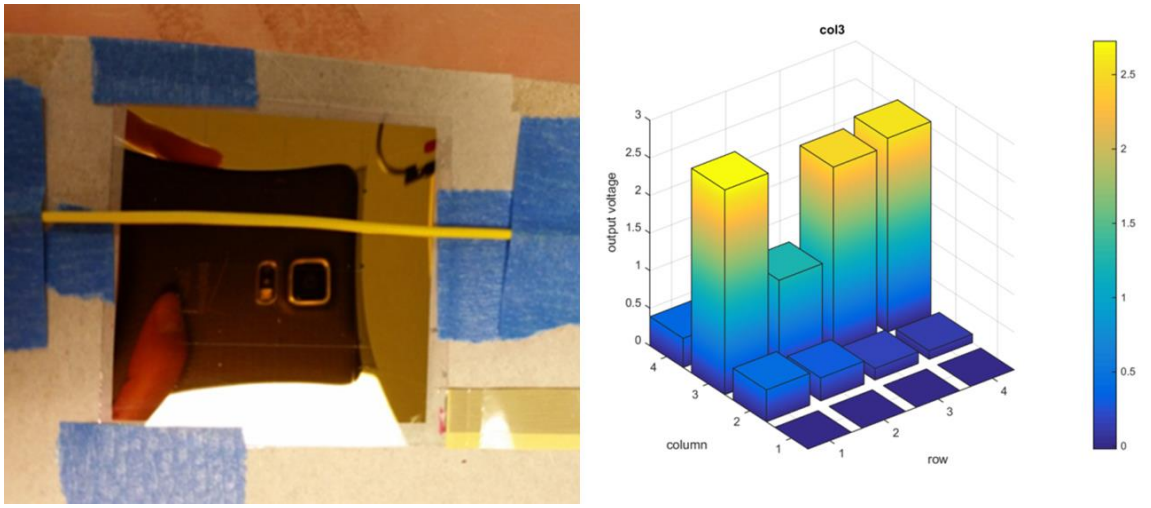

Figure 42: Close-up photo of setup of flexible imager with a wire carrying 2.5 V_{pp} at 970 Hz over column 3 (left) . Histogram of corresponding output voltages (right).

7.5 Analysis of Results

The InGaZnO TFTs demonstrated that the off-resistance was sufficiently high to operate properly as access transistors for such small signals. Because the TFTs can be fabricated on flexible substrates like PEN, it opens many possibilities to unique applications such as flexible electric field imaging blankets and EEG/ECG wearable caps. Furthermore, since it is a TFT-based array, it can leverage the cost-effective process of the display industry to make large area panels for low-cost.

Unfortunately, due to limited resources, we were unable to fabricate more devices in-house at FEDC. However, the hopes are that this 4 x 4 array will serve as a small-scale proof of concept of what is possible.

It should be noted that there were some design flaws that still had to be addressed. As previously mentioned, read lines from the sensor head to the transimpedance amplifier are highly susceptible to noise since they are low impedance nodes. This was no exception for the FLEX array as electric field sources must be kept away from the ribbon cable connecting the pixels to the multiplexer. Shielding with grounded aluminum foil did seem to have a positive effect but more standardized and thicker shields of metal will be needed to compensate for the skin depth of the electric fields at VLF.

Chapter 8

THE ONE-DIMENSIONAL STEPPER ARRAY (PCB)

This chapter covers the PCB one-dimensional stepper array. This design addresses the issues of the leakage currents found in the access transistors of the active matrix two-dimensional array while still managing to image large areas. The automated software driver, written in MATLAB, used to operate the imager is also discussed. This method was capable of clearly resolving electric fields from various wire formations, the results of which will be discussed.

8.1 Board Layout

Since the off-resistance of any single-crystal COTS transistor would not be sufficient to isolate the D-dot sensors, a "stepper" method was used in which a 16-pixel one-dimensional array was physically swept over the object of interest. The array was

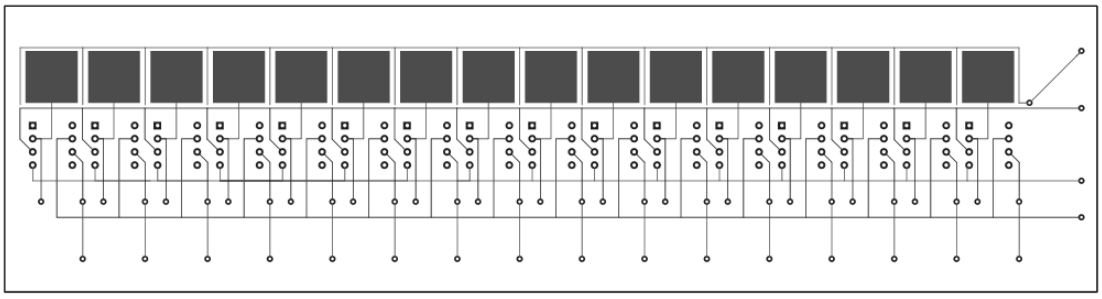

Figure 43: PCB layout of the one-dimensional stepper array.

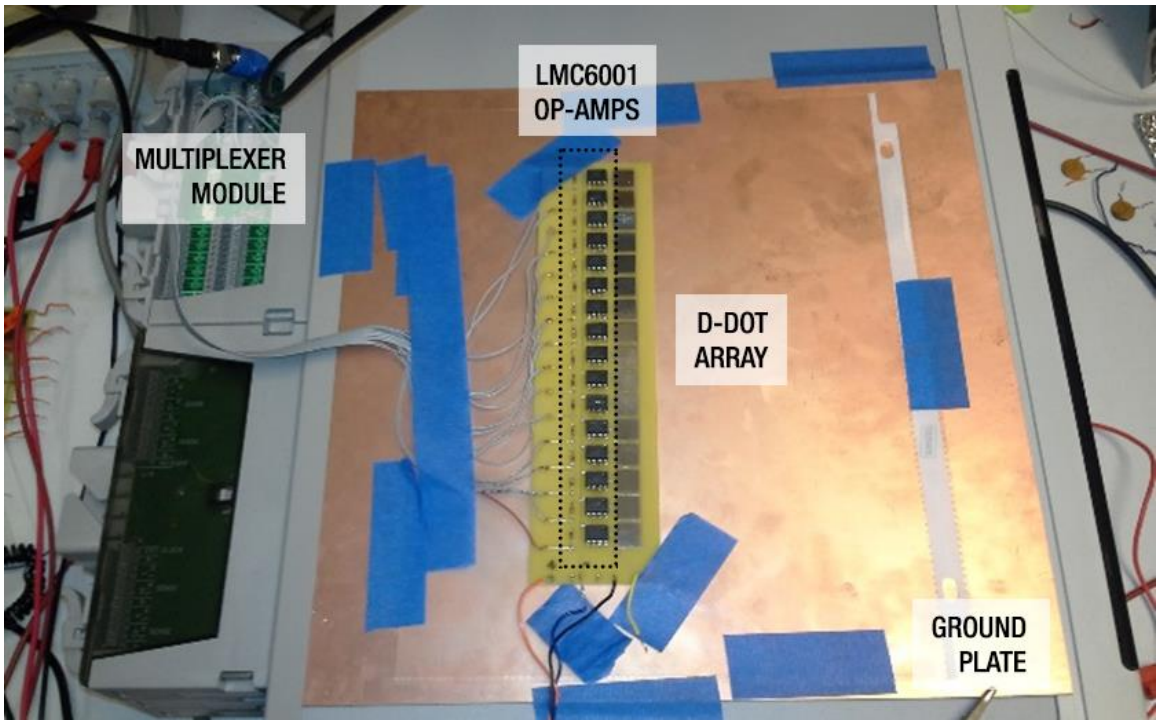

Figure 44: Photograph of the PCB stepper D-dot array.

fabricated on a two-layer PCB with 1 cm x 1 cm pixels where each pixel was connected physically close to an LMC6001 operational amplifier [62], Figure 43. By integrating the amplifiers directly into the design of the board, not only was the distance between the sensor head and the amplifier reduced, but the control of variation between pixels could be managed more precisely.

A photograph of the array can be seen in Figure 44. Immediately, it is clear how much cleaner this setup is compared to having a separate array of hardwired amplifiers in Figure 37. For initial runs, the ground plate of the D-dot sensors was simply a large copper plate that was shorted to ground. A plastic insulating sheet was placed in between so as not to short any components.

8.2 Automation

The task of manually operating the Agilent 34980A Multifunction Switch/Measure unit [57] and writing down the output values proved to be cumbersome and not scalable. In the 9 x 16 pixel images obtained, this process would require nearly 150 steps of constant attention taking well over an hour. To alleviate the task, the recording of data was automated by using a National Instruments Data Acquisition card to record and store the output of the lock-in amplifier.

Custom software drivers were written in MATLAB to communicate with both the data acquisition card and the Agilent 34980A [57]. The system could potentially be further automated by implementing a stepper motor which would automatically and mechanically shift the array. Future generations can also incorporate other sensors, e.g. gyroscopes, to utilize the one-dimensional array like a "wand" and obtain an image similar to some commercial portable scanners.

8.3 Wires in a Box Experiment

Keeping in line with previously conducted experiments, another set of measurements were made with wires in a concealed plastic box. The setup consisted of three 16-gauge wires separated by 5 cm from each other and placed 4 cm above the sensing array. The wires were placed and connected in a custom plastic box with BNC connectors

Figure 45: Setup 1: Experimental setup of a plastic box with 3 parallel wires (left). Setup 2: Similar setup but in which the top and bottom wires are connected with a jumper wire within the box (right).

for support and power. Additionally, the wires were constructed inside a plastic box to demonstrate they can be imaged through the container. Only the outer wires were charged with either a 97 Hz or 970 Hz signal at 10 V_{pp}. An unenergized middle wire was included to prove the method images only energized wires.

Both a shielded and floating connecting wire were tested. The box was placed on a slightly elevated plastic platform with engraved markings in a 0.5 cm grid, Figure 45. The wire formation was then mechanically shifted over the imager, which was fixed in position underneath the platform, at 1 cm increments to emulate a scanning wand. Over the course of nine steps, the array yielded an image of 9 cm x 16 cm.

8.4 Experimental Results

It is clear from the three-dimensional histogram, Figure 46, of the lock-in output from Setup 1, Figure 45, that the device is imaging the electric fields radiating from the

two energized wires. The source resolution of the image is approximately 4 pixels, and is roughly equal to the distance between the wires and the sensing array. The outlines of the box and wires are superimposed on top of the heatmap as a visual aid.

The electric field strength outside of the box is considerably weaker than inside. Where the signal enters, there is almost no electric field component because the incoming coaxial cable is grounded. The electric field strength outside of the box on the other end is non-trivial because the BNC connector was left open, allowing electric flux lines to leak out. Note portions of the coaxial cable with floating ground that connect the two wires on the bottom of the image.

A similar result, Figure 47, is obtained from Setup 2, Figure 45, in which the two wires were connected with an unshielded wire and alligator clips. All other factors were held constant including the voltage at 10 V_{pp}, frequency at 970 Hz, and the distance from the array at 4 cm.

Interestingly, the strongest signal for the non-shielded jumper wire configuration comes from the bottom right in Figure 47. Upon inspecting the photo of the setup, Figure 45, the spike is due to the alligator clip extending a few millimeters below the wires, creating an increased capacitance to the sensing array. This again reflects on the accuracy and sensitivity of the imager.

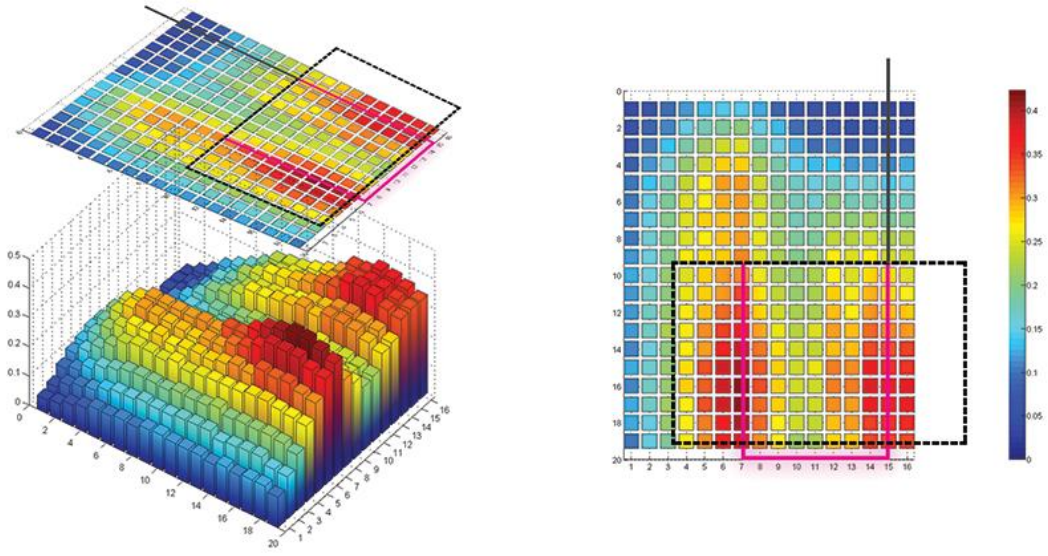

Figure 46: The electric field image for the box with a shielded connection. The outlines of the box and wires are superimposed in the angle view (left) to easily see the effect of the wires and two-dimensional heatmap is provided (right).

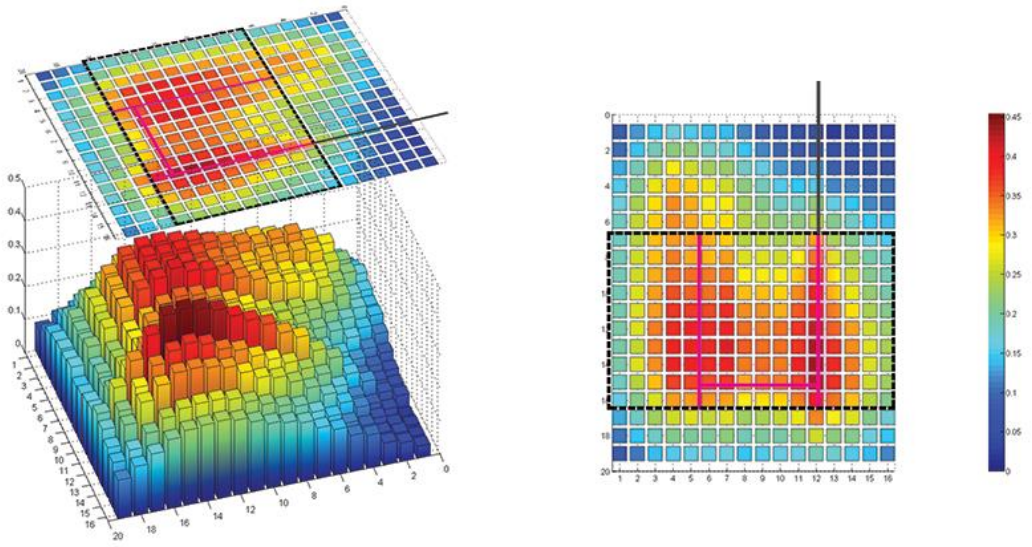

Figure 47: The electric field image for the box with a non-shielded connection at an angle view with images of the wires superimposed (left) and a two-dimensional heatmap from the top view (right).

8.5 Wires on Drywall

Another application of interest is imaging power lines behind walls. To prove its feasibility, a meandering wire was taped onto a slab of drywall, Figure 48. The frequencies tested were 97 and 970 Hz at voltages of 1, 3, and 9 V_{pp}. The wire hanging off the edge of the board was wrapped in aluminum foil and grounded in an effort to shield the portion of the wire that was not intended to be imaged.

There was also an interest to measure the wires at various heights for future reconstruction algorithms. The height was in units of drywall slabs (each slab being

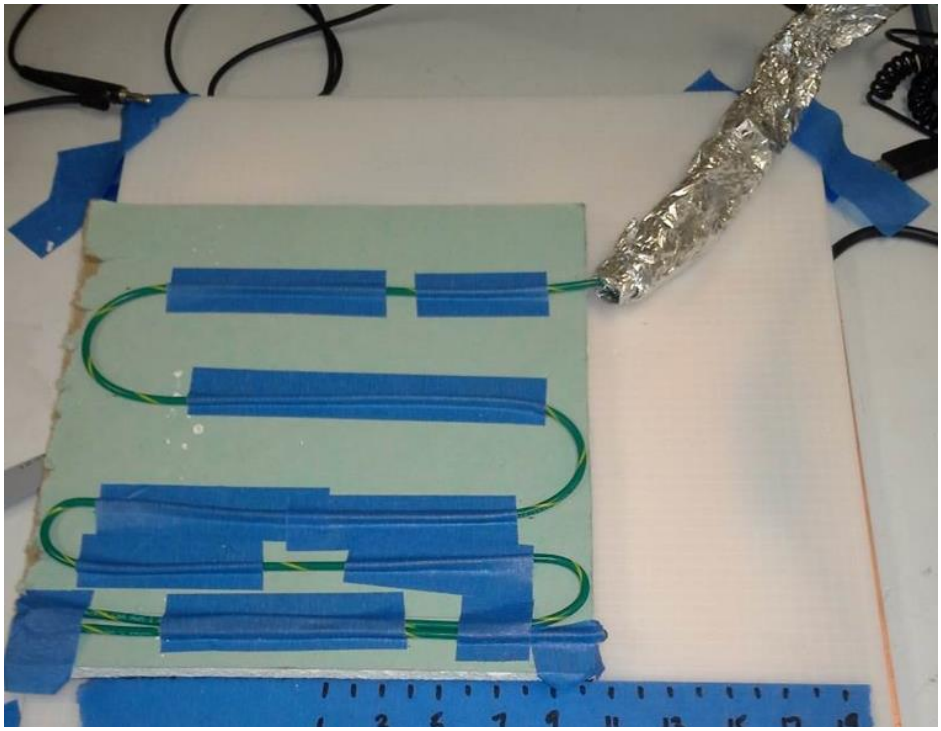

Figure 48: Photograph of the wire formation used on drywall.

approximately 1.5 cm thick) and an additional offset of 1 cm from the platform. The measurements also provided insight into the fringing effects based on height. Namely, less prominent peaks are to be expected the further the wires are from the imager.

8.6 Experimental Results

Consistent with previous measurements, the signal strength was proportional to the voltage level and frequency. Knowing this, a small sample of results is provided to observe the effect of height. When the wire was 2.5 cm from the array, Figure 49, the electric field strength is relatively high. A large signal can also be seen where the wires were closely spaced.

When adding an additional 1.5 cm, Figure 50, the presence of the wires is still apparent through not resolved as clearly. Despite the colormap being the same, the range is smaller. Additionally, the electric fields cannot be readily resolved laterally, particularly in areas where the wires are not dense.

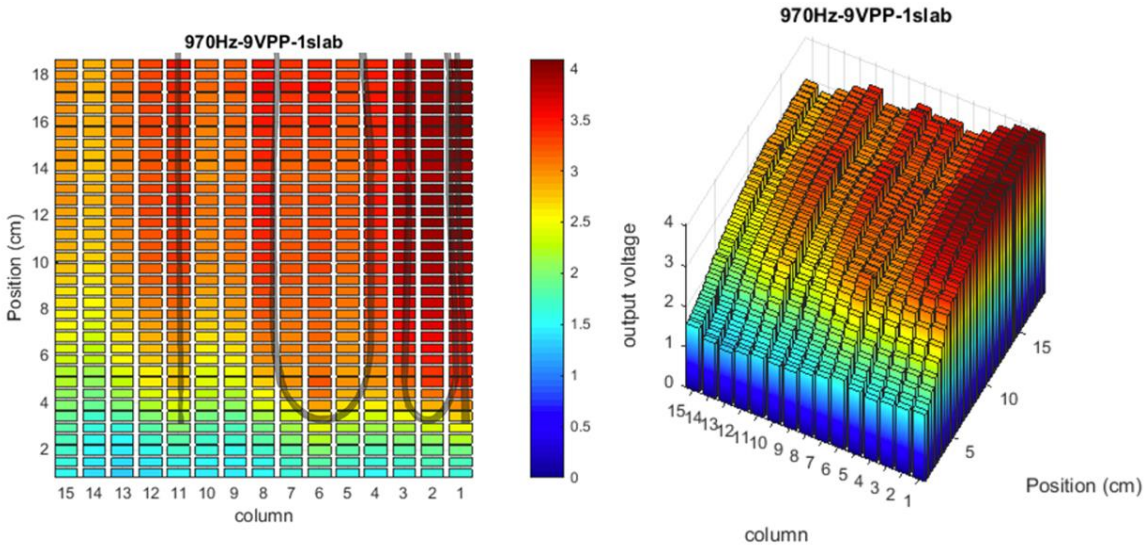

Figure 49: Electric field image of the meandering wire formation of various distances on one slab of drywall.

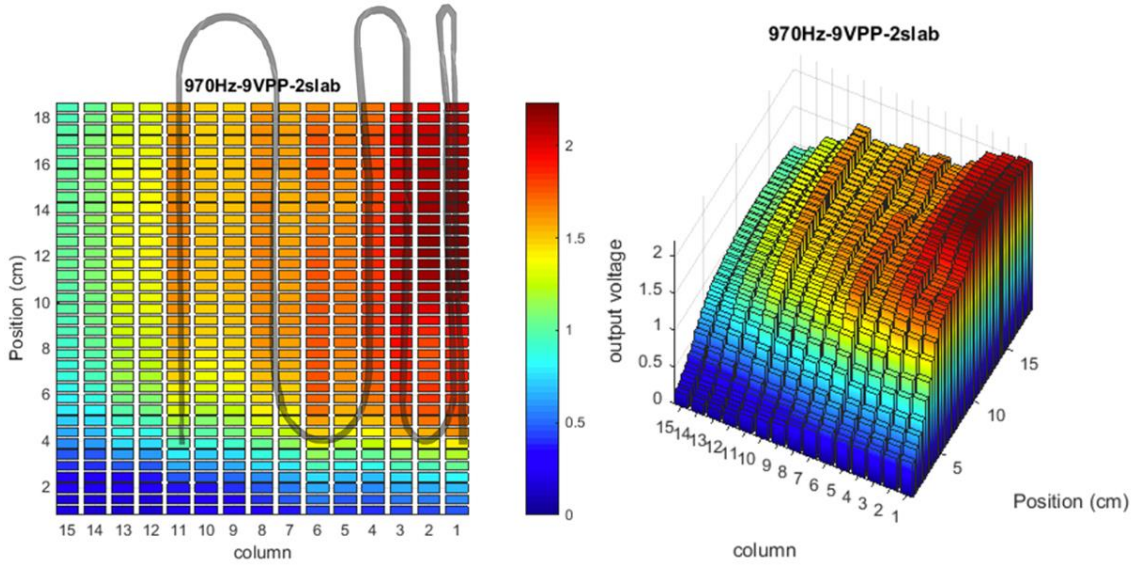

Figure 50: Electric field image of the meandering wire formation of various distances on two slabs of drywall.

8.7 EMI Detection: Buck Converter

Electromagnetic interference (EMI) is an expensive and ongoing issue that can severely degrade the performance of a circuit. The ability to detect EMI sources would help circuit designers find and rectify such portions of their design more efficiently. Power components often generate EMI due to the oscillating nature of operation. For openers, the stepper array was used to detect EMI from a 9 to 3 V DC to DC buck converter.

The buck converter was built around the Texas Instruments LM2576 simple switcher [74] with a prominent source of electromagnetic emission. Though the chip nominally operates at a switching frequency of 52 kHz, measurements with a spectrum analyzer revealed that it more closely operates at 50.25 kHz, Figure 53. Both a compact and expanded version, Figure 52, were constructed to determine if the imager would detect the buck converter in the compact configuration and see individual components in the expanded configuration. The full schematic used can be seen in Figure 51.

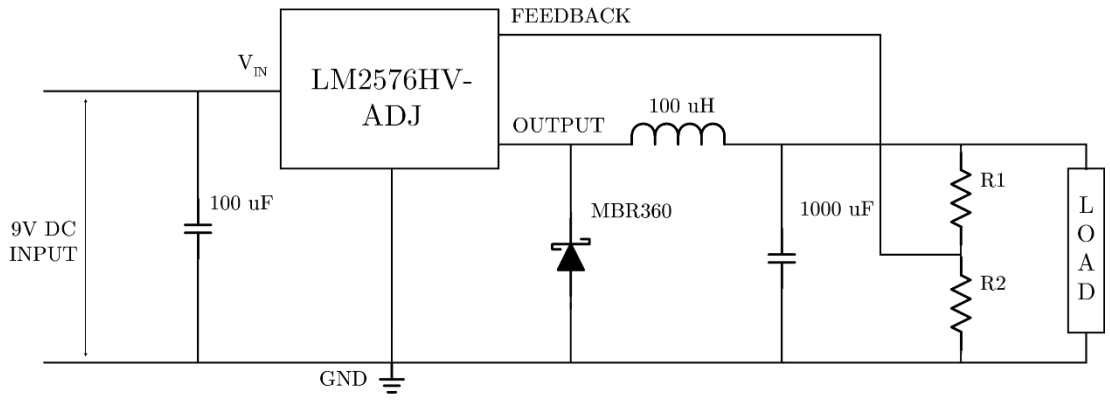

Figure 51: Schematic of the buck converter.

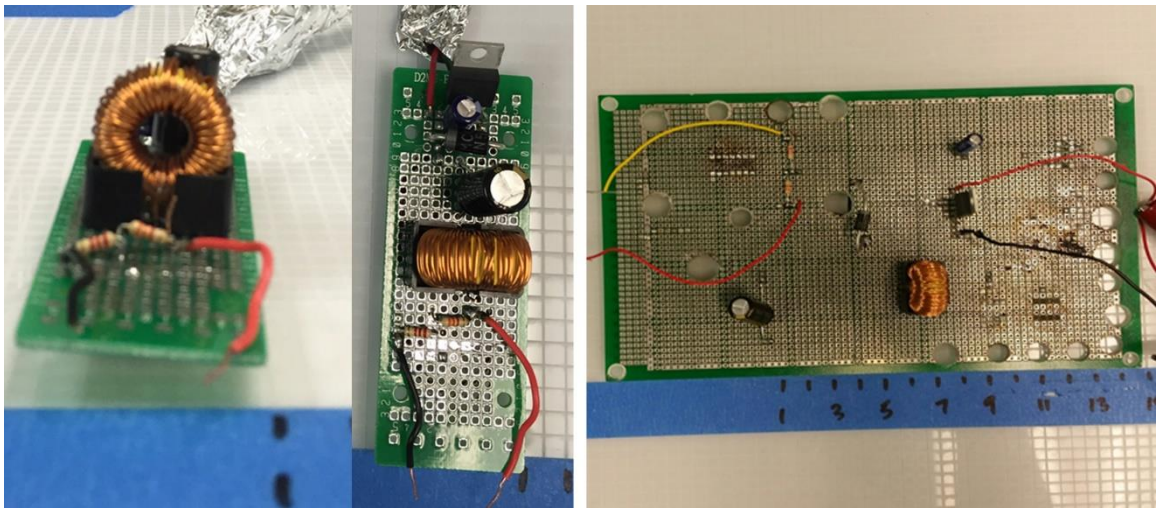

Figure 52: Photograph of the compact buck converter at an angle and with a top-view (left) and of the expanded buck converter (right).

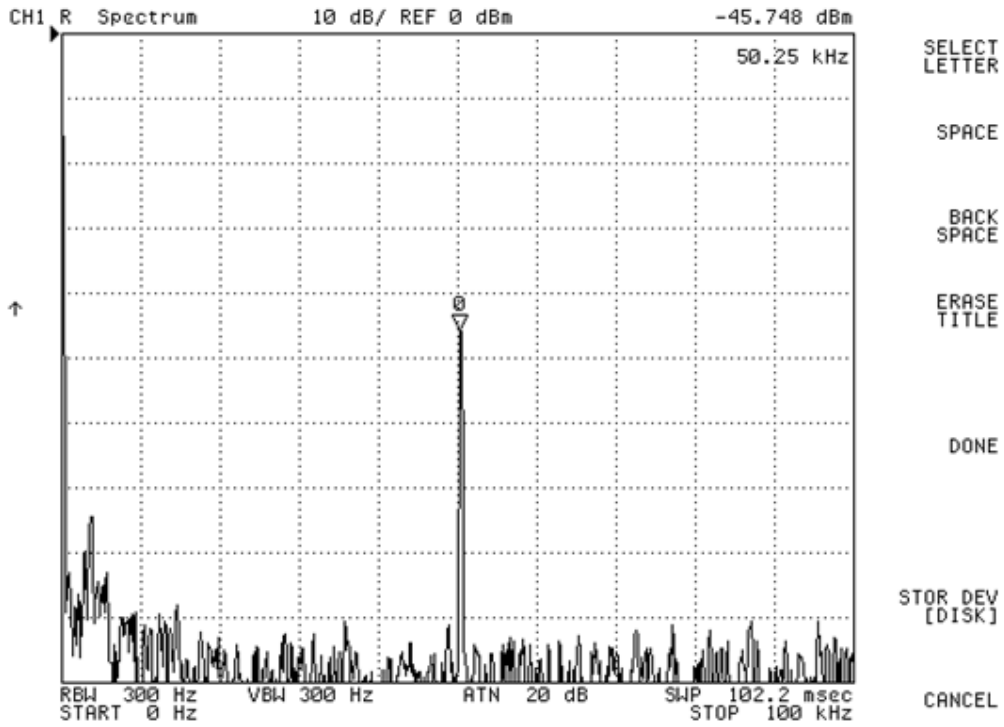

Figure 53: Frequency response of the buck converter output.

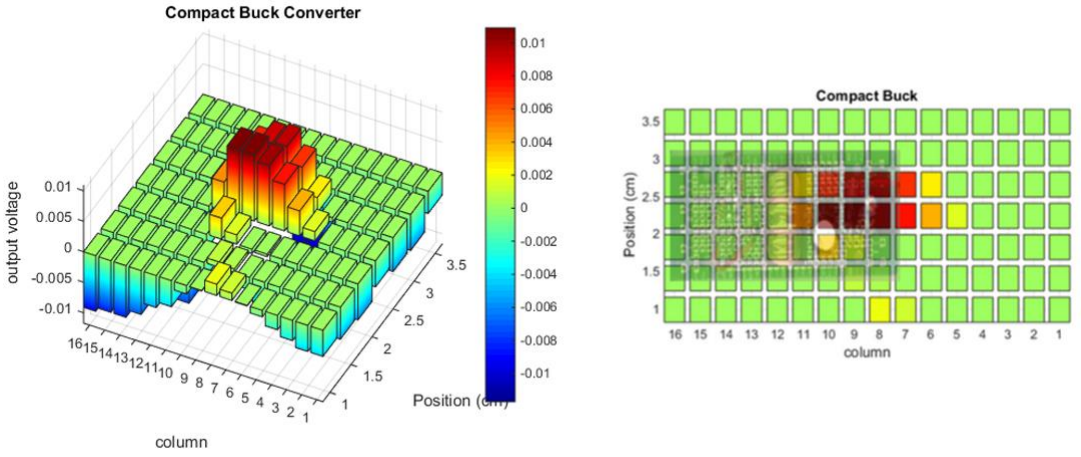

Figure 54: Electric field image of the compact buck converter (left) and a top-view with an overlay of the board (right).

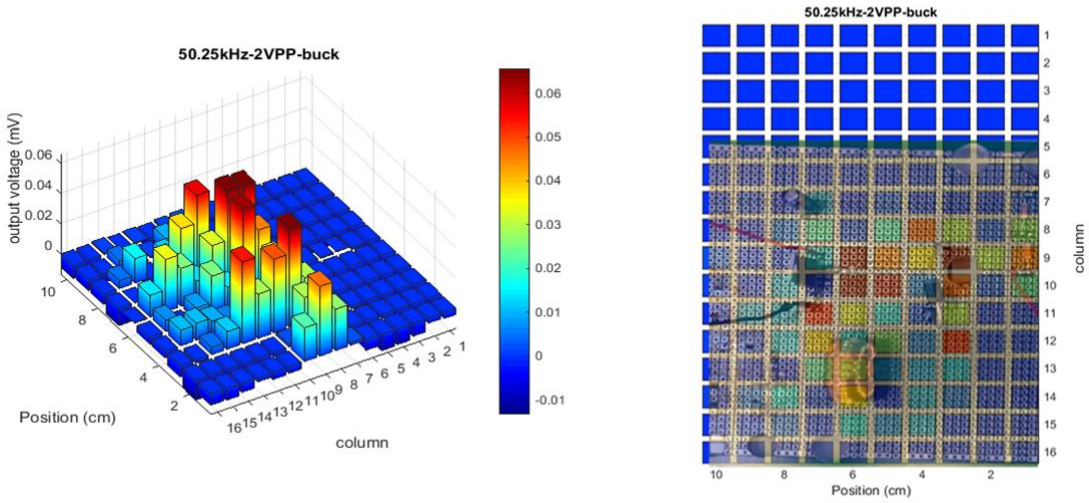

Figure 55: Electric field image of the expanded buck converter (left) and a top-view with an overlay of the board (right).

8.8 Experimental Results

It is evident from the images obtained, Figure 54 and Figure 55, that the array can image EMI sources. While the imager is capable of detecting EMI in the compact buck converter, it is difficult to resolve individual components due to the coarse resolution. With the expanded configuration, the imager managed to pick out individual sources, namely the switching unit, the output load, and the inductor.

These measurements also demonstrate that the system is capable of imaging AC signals without having direct access to the reference frequency. This is critical because the reference frequency will not always be directly available in real-world applications. Even when it is provided, such as with the LM2576 datasheet, slight deviation from the actual operating frequency can cause the signal to be outside the narrow bandwidth of the lock-in amplifier.

Chapter 9

AN ACTIVE METHOD OF IMAGING WITH AN 8 X 8 ARRAY (PCB)

Despite the positive results obtained from the one-dimensional stepper array, mechanically shifting the imager in its current state of development can introduce errors, especially when done by hand. Furthermore, this makes it very time consuming and labor intensive to image large areas since it must constantly be monitored and manipulated by a human user with each row measurement.

A fully two-dimensional imager would not only expedite measurements of larger areas but also produce more reliable measurements. In this chapter, a new two-dimensional design philosophy is covered which addressed the shortcomings seen in the active matrix architecture. Additionally, this new imaging system served as the platform in the development of new active method of imaging. This new method made it possible to image objects that were not electric field sources.

9.1 Board Layout

Since there were no available COTS transistors with a low enough leakage to serve as an access transistor, an alternative design philosophy to the active matrix architecture had to be implemented for a two-dimensional array. Given the success of the one-dimensional stepper array, it was decided to extrapolate it to two dimensions.

The through-hole components of the LMC6001 [62] proved to be problematic since they inhibited real estate for any further D-dot sensor heads. The surface mount counterpart, LMC6081 [75], was used in its place and placed on the bottom layer to provide an open area for sensor heads on layer 1. The board was also upgraded from 2 layers to 4 so that additional traces could be routed in the intermediary layers, again providing more open real-estate on layer 1. Of the four layers, layer 3 was fully filled with metal, aside from a few via gaps, to serve as a ground plate and extra shielding.

With these changes, we designed an 8 x 8 array with 1 cm^2 pixels, Figure 56. A ribbon cable interface was also integrated to avoid the need to manually hardwire 64 pixels to the multiplixer. While the traces to the multiplexing unit may have varied between pixels, it should have not affected the signal since it was assured that each operational amplifier was uniformly placed under each D-dot sensor head so that the distance from the metal pad to the amplifier was equal for all pixels.

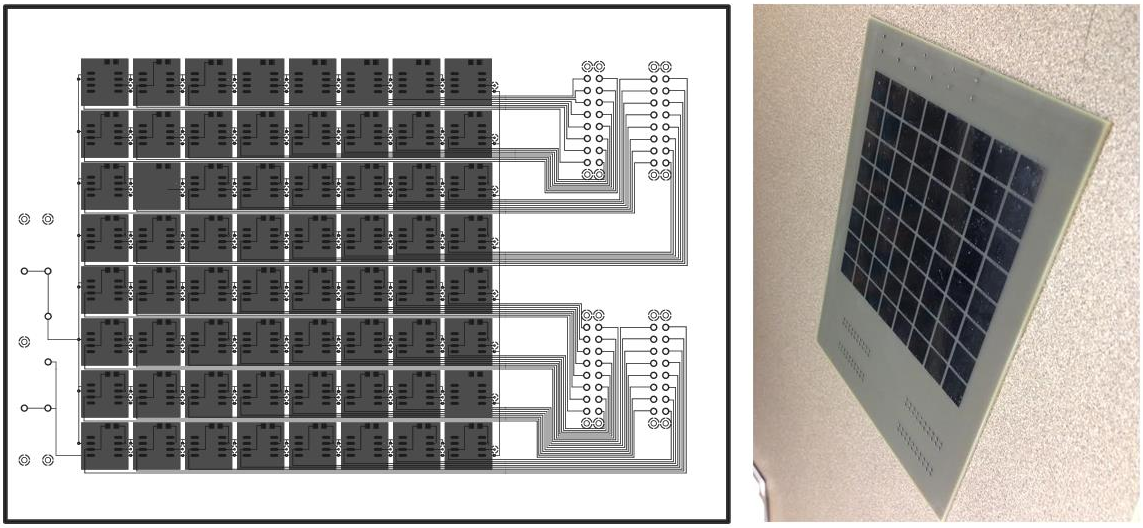

Figure 56: Schematic (left) and fabricated PCB (right) of the two-dimensional D-dot array electric field imager.

9.2 Automation Software

A fully automated system was developed. The base script, written in MATLAB, establishes communication between the Agilent Multiplexing units and the National Instruments Data Acquisition Card, locally archives the data, and assembles data visualizations. It was largely unchanged from the automation scripts described in the previous chapters aside from the expansion in the number of channels.

One of the shortcomings of the Agilent Multiplexing units, however, was that each bank had only 20 channels. Therefore, for 64 pixels, four banks were utilized in which each had 16 channels occupied. The output cable would have to physically be disconnected and reconnected when moving from one bank to another. A code block was added to the automation script which provided an interface with an Arduino Uno microcontroller. The microcontroller would then automatically control the output between the four banks.

9.3 Passive Image Sanity Check

To verify that the new two-dimensional imaging array was not experiencing any unsuspected issues (e.g. leakage in the active matrix array), a quick sanity check was conducted by passively imaging an energized wire. When a wire was placed directly over a row or column, only that nearby row or column would show an increased strength in

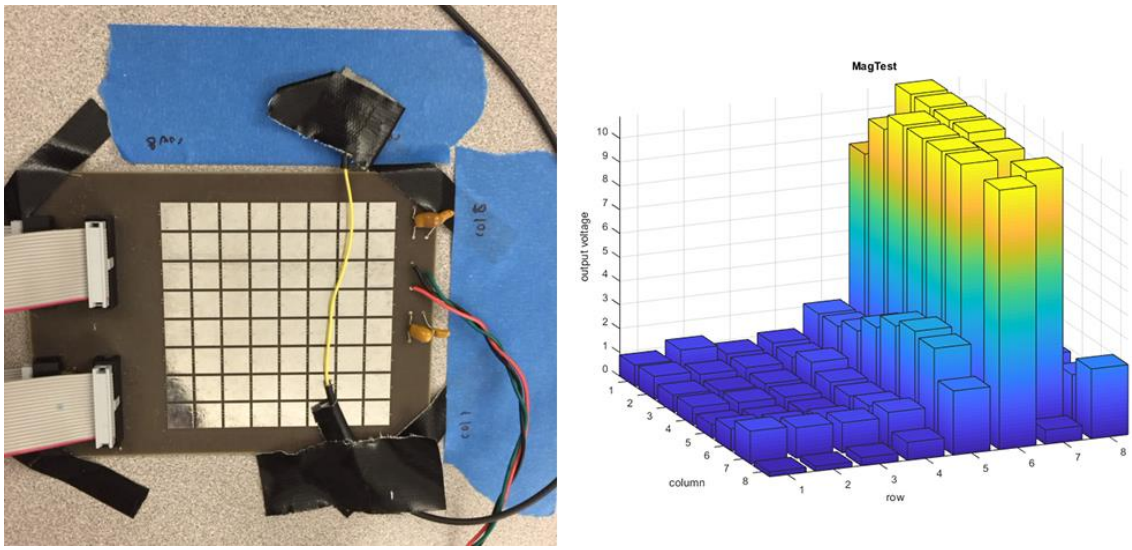

Figure 57: Photo of experimental setup of the passive electric field verification (left) on the two-dimensional array and its output (right).

signal. This verified that the array was indeed imaging the electric fields it was intended to capture and consistent with the readings acquired with the stepper array, Figure 57.

9.4 Active Imaging: Imaging Beyond Electric Field Sources

Here a new method of imaging, dubbed 'active imaging,' is introduced, which was made practical with the full two-dimensional array. To actively image, a source electrode must generate a known electric field. For ease of analysis, a parallel plate can be placed above the array of D-dot sensors to generate a uniform electric field at all points of the array. The geometry of this setup is in essence a parallel plate capacitor, Figure 58, and thus electrostatic derivations are similar. Objects placed between the plates will then distort the known uniform field which is read with the D-dot array.

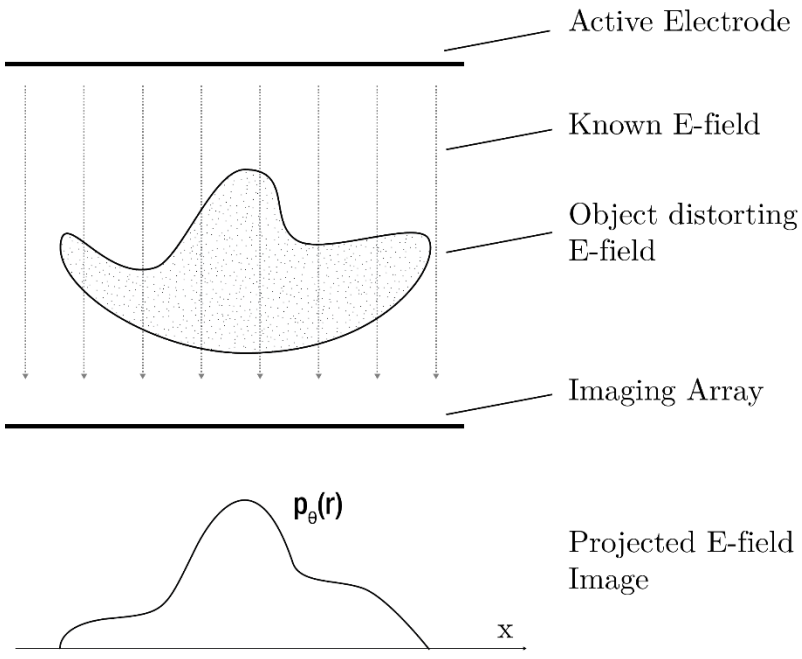

Figure 59: Diagram depicting the basic components of an active electric field imaging setup.

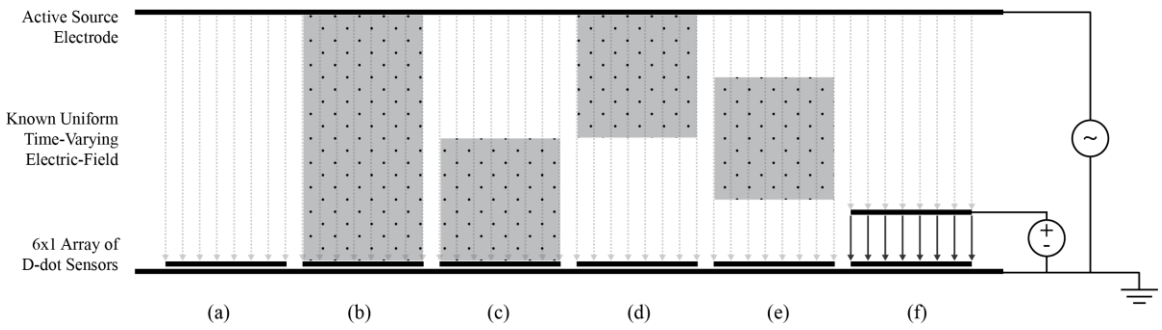

Figure 58: A 6x1 D-dot array in an active imaging setup with objects under test including (a) air, (b) a uniform dielectric consuming the entire space between the sensor and source electrode, (c) a uniform dielectric near the D-dot consuming half the space between the sensor and source, (d) the same dielectric but near the source, (e) the same dielectric but halfway between the D-dot and source, and (f) a metal plate held at a DC voltage with respect to ground.

9.4.1 Uniform Dielectric Under Test

There are various classes of objects that require different approaches in calculating their distortion effects. Several are depicted in Figure 59. We begin with the simple case of a dielectric filling the entire space between source electrode and D-dot, Figure 59b. Since the analysis is quasi-static in the VLF range and the geometry is parallel plate capacitor, the electric field can be described by

$$E = \frac{Q}{\epsilon A} = \frac{V\,t}{d} = \frac{V \sin\, 2\pi f t}{d} \qquad (9.1)$$

Placing a dielectric body between the active electrode and the D-dot array will affect the parallel plate capacitance and consequently the electric field is accordance to the capacitance relationship

$$C = \frac{k\epsilon_0 A}{d} = \frac{Q}{V} \qquad (9.2)$$

where *k* is the relative permittivity of the dielectric. It is observed that since the area and distance remain fixed, the introduction of a material with a higher dielectric constant will yield a higher capacitance. Since the voltage between the plates is held constant, Equation 9.2 also shows that the charge on the plate increases for an increase in capacitance, as does **D**, the electric flux density (C/m^2). This corresponds to an increase, or distortion, of the electric field described in Equation 8.1 which is measured by the D-dot sensor(s) directly under the dielectric medium.

9.4.2 Multiple Dielectrics Under Test

Figure 59c depicts a scenario in which the object under test does not occupy the entire space between sensor and source electrode. In this scenario, the dielectric constant of air must be considered in addition to that of the material, making it a multiple dielectric problem. The stacked dielectrics can be modeled as capacitors in series. The total charge can then be determined to find the expected electric flux density at the sensor. Notably, this model applies to a metal object placed in the uniform electric field as well which is equivalent to a material with an infinite dielectric constant.

9.4.3 Fringing Effects

The vertical position, Figure 59c-e, of the dielectric does not affect the capacitance, nor the total charge. However, due to fringing fields, the charge distribution can be affected and thus affect the D-dot signal depending on its location in the lower plane. To demonstrate, a simple parallel plate setup was modeled in ANSYS Maxwell. The ratio of the plate length to the distance was 10:1 so a relatively uniform electric field could be generated in the center. A small block of water was then placed near the center of the bottom plate, Figure 60b. The electric flux density along the surface of the bottom plate was then collected to simulate what the D-dot array would read. This was repeated with the block of water placed near the top plate, Figure 60c.

Looking at the electric flux density distribution along the bottom plate, Figure 60a, the presence of the water increased the signal response as expected since it has a higher

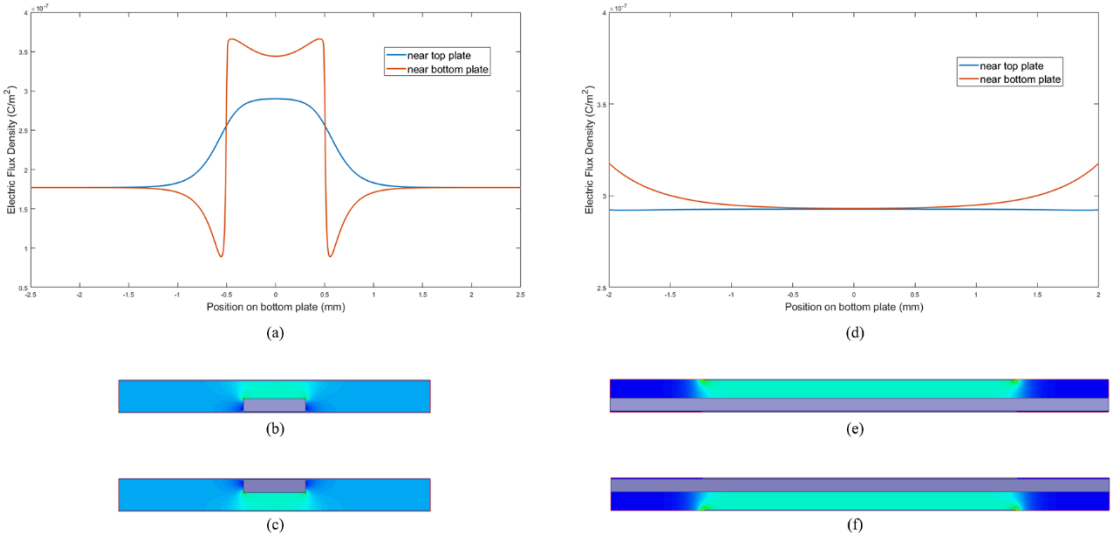

Figure 60: (a) Electric flux density distribution on the bottom plate of a parallel plate capacitor when a small block of water is under test near the (b) bottom plate and (c) top plate to exemplify when fringing is not negligible. (d) Electric flux density distribution on the bottom plate of a parallel plate capacitor when a large block of water is under test near the (e) bottom plate and (f) top plate to exemplify when fringing in minimized. These simulations were run in ANSYS Maxwell.

dielectric constant (~81) than its surrounding vacuum (1). However, fringing effects can clearly be seen depending on the position of the block of water between the parallel plates.

The setup with the block of water near the bottom plate yielded a stronger response directly under the block of water, as expected, with strong fringing effects immediately adjacent to the block. When the block of water is near the top plate and far from the D-dot sensors, the detected signals are more diffuse – weaker under the block of water but still detectable at some distance on each side. It is important to note that the capacitance and total charge are the same between the two setups exemplified by the fact that the integral of both curves are equal, i.e. the total charge on the bottom plate is constant.

When the dielectric slab is very large laterally relative to the size of the D-dot detection array, there is a negligible difference in the D-dot signals regardless of the

difference in position, Figure 60d. Since the slab is not infinitely long, fringing effects can be seen the closer to the edge one gets.

9.4.4 Fringing Effects

This conclusion is derived from the assumption that the object under test is floating. In the case that the object is held at a constant potential, e.g. DC wires and Figure 59f, the voltage described in Equation 9.2 does change. However, since the voltage is not time-varying, it does not contribute to the D-dot current and effectively "shields" those pixels. If the body is sufficiently far from the D-dot, fringing electric fields will compensate and contribute to the signal strength to some degree.

9.5 Design of Testing Apparatus for Active Imaging

The imaging board is placed on top of a large copper plate, 12" x 12", which is grounded for a reference and serves as an area for electric flux lines to terminate and maintain a uniform structure. A thin insulating layer of plastic is also placed between the imager and the large ground plate as an extra measure to prevent any shorting. An identical 12" x 12" copper plate which served as the active electrode was placed above the imaging setup using non-conducting PVC connectors, ~8.5 cm in length, as pillars to hold it up, Figure 61. The active plate was energized with an Agilent 33250A Function/Arbitrary

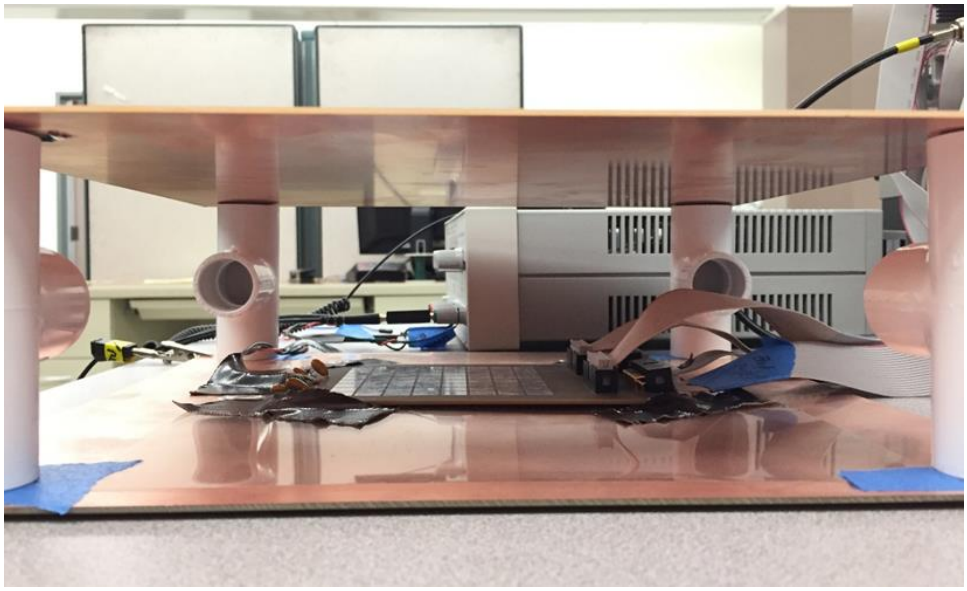

Figure 61: Side-view of testing apparatus. The two large parallel plates create a uniform electric field which is read by the two-dimensional imager. Objects can then be placed between the imaging array and the top plate.

Waveform Generator [56]. Since we directly provide the electric field source, the reference frequency can directly be tapped by splitting the function generator to the lock-in amplifier.

The two main experimental setups were the imaging of DC wires and the imaging of dielectrics. In both experiments, a large copper plate was placed above and parallel to the imaging array as an active electrode. The plate was considerably larger than the array since the electric field is relatively constant aside from the edges due to fringing. This ensured that the imaging array would not be imaging fringing fields. The active electrode had a 9.7 kHz 10 Vpp signal applied with a multifunction generator.

For the DC wire setup, the wire was bent at various points to create a unique shape that would be difficult to image by chance or environmental circumstances. By applying a DC voltage, the time-varying electric field from the active electrode was "shielded" or "blocked," producing an inverse image of the wire. Namely, wherever the sensors did not

receive a signal is where the wire was located. This is notably different from other explored mechanical methods to sense DC voltages with D-dot sensors including fluctuating the distance between the DC source and the sensor or spinning a grounded blade to "chop" the electric field, both operating at some given reference frequency [76], [77]. Our method does not require any mechanical moving parts, reducing margin of error and likelihood of failure.

For the dielectric measurements, water was the main dielectric of interest due to its high relative permittivity (~81 at room temperature), particularly when compared to its surrounding medium of air (~1 at room temperature), allowing for strong contrast. Water was contained in a plastic vial at various levels to observe its effect on electric field readings. Based on calculations in the previous section, it was to be expected that the higher the water level (i.e., the greater ratio of water to air between the D-dot and active electrode), the higher the signal reading would be.

9.6 Sensitivity Calibration

Given the new parallel plate setup, it was easy to test all the pixels with a relatively uniform field. The redundancy made it ideal to run some sensitivity calibration tests. As described, the signal strength of the D-dot sensor is theoretically linearly proportional to the frequency and voltage of the active electrode. However, there are hardware limits such

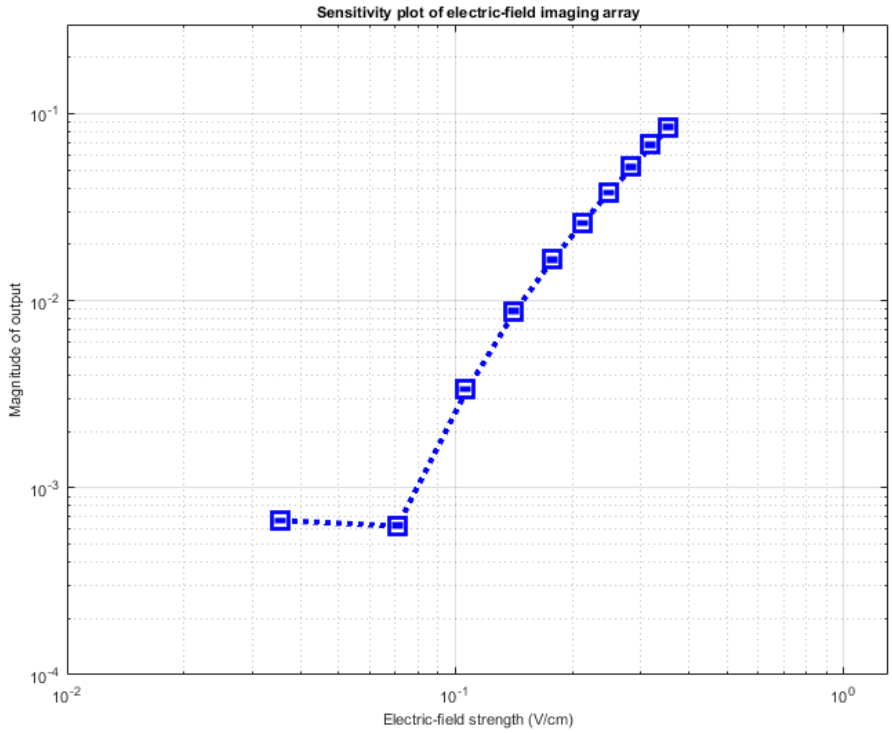

Figure 62: Log-log plot of average D-dot sensitivity measurements with respect to electric field strength (V/cm).

as the bandwidth of the transimpedance amplifier where measurements would break from the linear trend and saturate around 40 kHz, consistent with the datasheet of the LMC6081 amplifier [75].

A noise floor will also eventually be reached when dealing with very small electric fields. All 64 pixels were tested at progressively weaker electric fields, the averages of which can be seen in Figure 62. When testing the sensitivity of the pixel, it was found that linearity begins to deviate around 0.1 V/cm and that the noise floor is reached around 0.07 V/cm. This equates to a current of ~38 pA that the D-dot sensor is capable of detecting for this setup. It should be noted that these are conservative upper bound limits.

During the test, it was found that a handful of pixels, six at the time of measuring, were “dead” which was most likely attributed to blown amplifiers. The affected pixels, which are pinpointed in Table 7, were omitted from the 64-pixel average calculation. The dead pixels will be evident and appear in several of the upcoming electric field images where there will unexpectedly be either no signal or a saturated signal.

Table 7: Grid layout of dead pixels in 8 x 8 electric field imaging array, likely attributed to dead blown amplifiers.

	TOP (ribbon cable)							
Row/Col	**8**	**7**	**6**	**5**	**4**	**3**	**2**	**1**
8	8	16	28	36	8	16	28	36
7	7	15	27	35	7	15	27	35
6	6	**14**	26	34	6	14	26	34
5	5	13	25	33	5	**13**	25	33
4	**4**	12	24	32	4	12	24	32
3	3	**11**	23	31	3	11	23	31
2	**2**	10	22	30	2	10	22	30
1	1	9	**21**	29	1	9	21	29
	BOTTOM (capacitors)							

9.7 Key DC Measurements Results

When a wire was bent into the shape of a "U," the resulting electric field image was obtained, Figure 63. It is very clear that the image is topographically dependent as only the pixels directly underneath the wires see a large deviation in signal strength.

The wire was held at 10 V but this value is trivial since, as expected, the D-dot sensors directly underneath the DC wire exhibited a lower signal. This verifies the earlier electrostatic model that the D-dot will not exhibit a signal because it cannot read the necessary time-varying signal which is "shielded" by the static DC wire. It should be noted that there appears to be a handful of dead pixels, as described earlier.

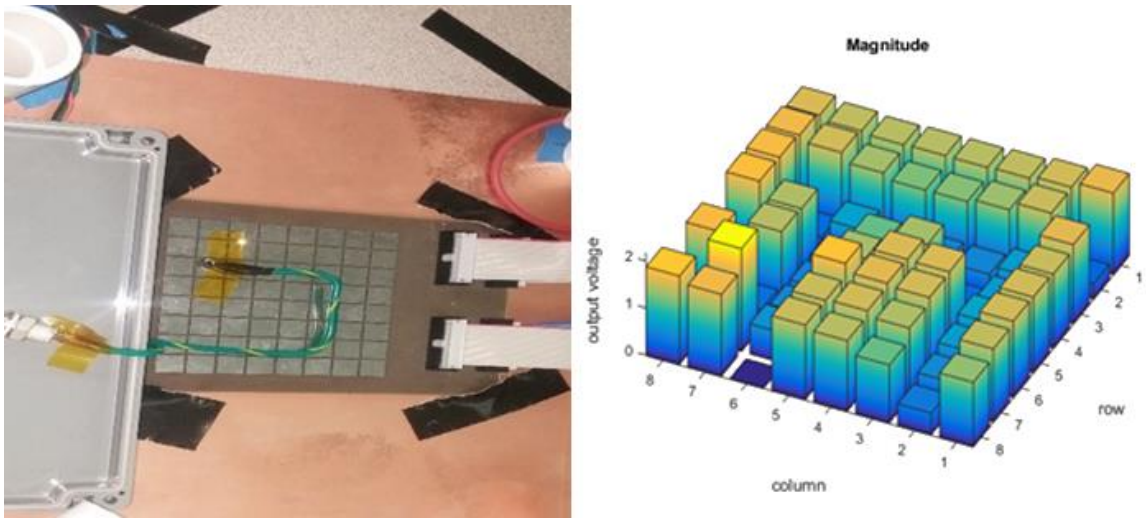

Figure 63: Experimental setup (left) and electric field image (right) of a "U"-shaped DC wire. The image experimental setup omits the top active electrode plate to better view the topology of the wire.

9.8 Floating Wire Results

Imaging a floating wire yielded a much fainter signal but could be detected nonetheless, Figure 64. Since the wire is floating, we would not expect to see a shielding effect but rather an enhancement of the electric field since the distance is now closer than the active electrode. For this test, an intervening floating wire was placed 1.5 cm above row 4 of the sensing array with a 10 V_{pp}, 97 Hz electrode driving 5.6 cm above the wire. The distortions created by the wire can be seen in rows 3-5.

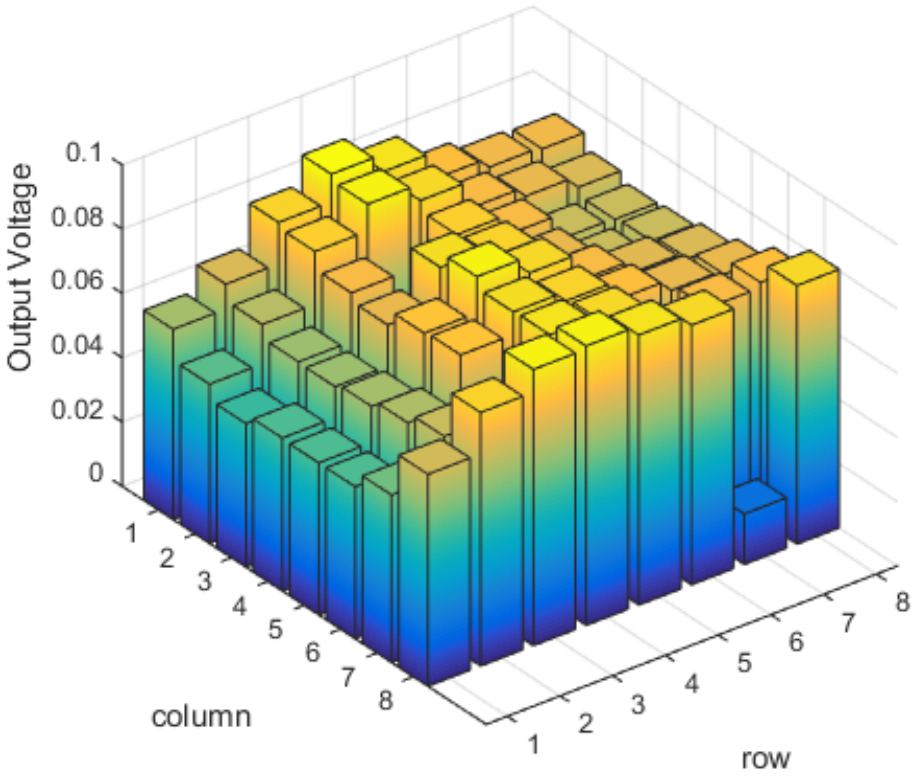

Figure 64: Electric field image of a floating wire 1.5 cm above the sensing array using the active method of imaging.

9.9 Results of Dielectric Directly on Imager

The presence of a high dielectric material would distort the electric field relative to its position. An example of a vial filled with water, Figure 65, shows that only the pixels directly underneath the water exhibited a greater signal. Pixels partially covered by the vial of water would yield a higher signal than uncovered pixels, but predictably less than pixels full covered.

The theoretical model indicates that if a greater portion of the space between the D-dot sensor and the active electrode is consumed with a higher dielectric, the charge (and thus signal strength) should also increase linearly. The results were consistent with these postulates as seen Figure 66.

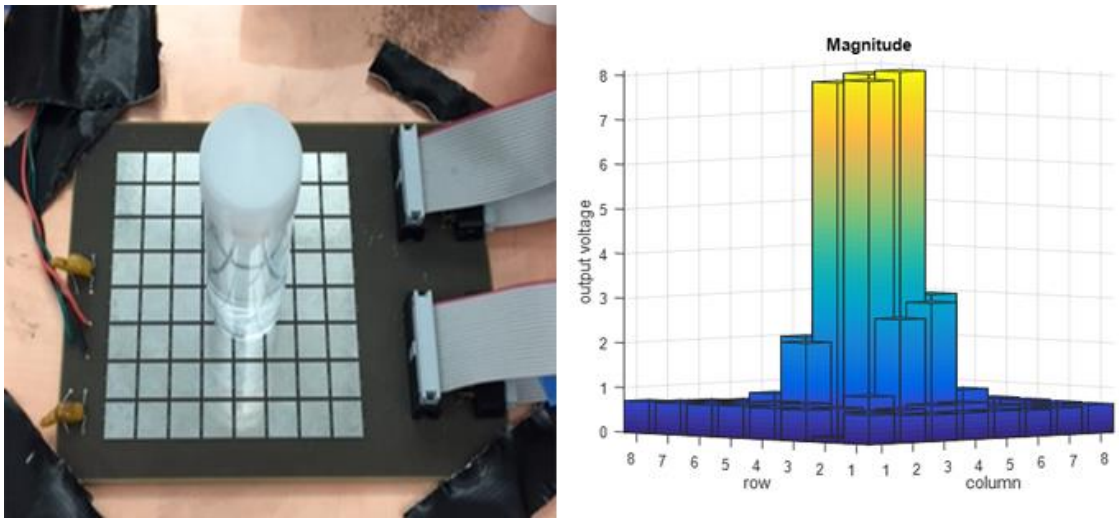

Figure 65: Experimental setup (left) and electric field image (right) of a full vial of water. The image experimental setup omits the top active electrode plate to better view the position of the vial.

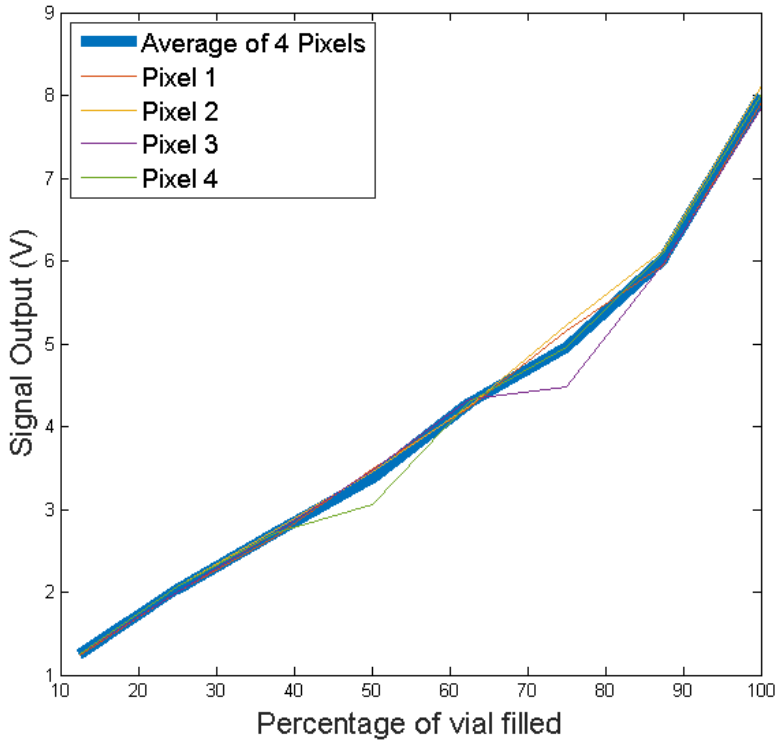

Figure 66: Signal levels for the four prominent pixels under a vial filled with water to various levels as well as the average of the four pixels in bold.

Here, the four more prominent pixels are tracked with various percentages of the vial being filled with water. Slight deviations can be attributed to the fact that the vial may not have been perfectly placed in the same location with each test, but overall a direct relationship can be seen.

9.10 Dielectric Elevated Above Imager

When the vial was elevated above the D-dot, the image became more diffused also as shown in

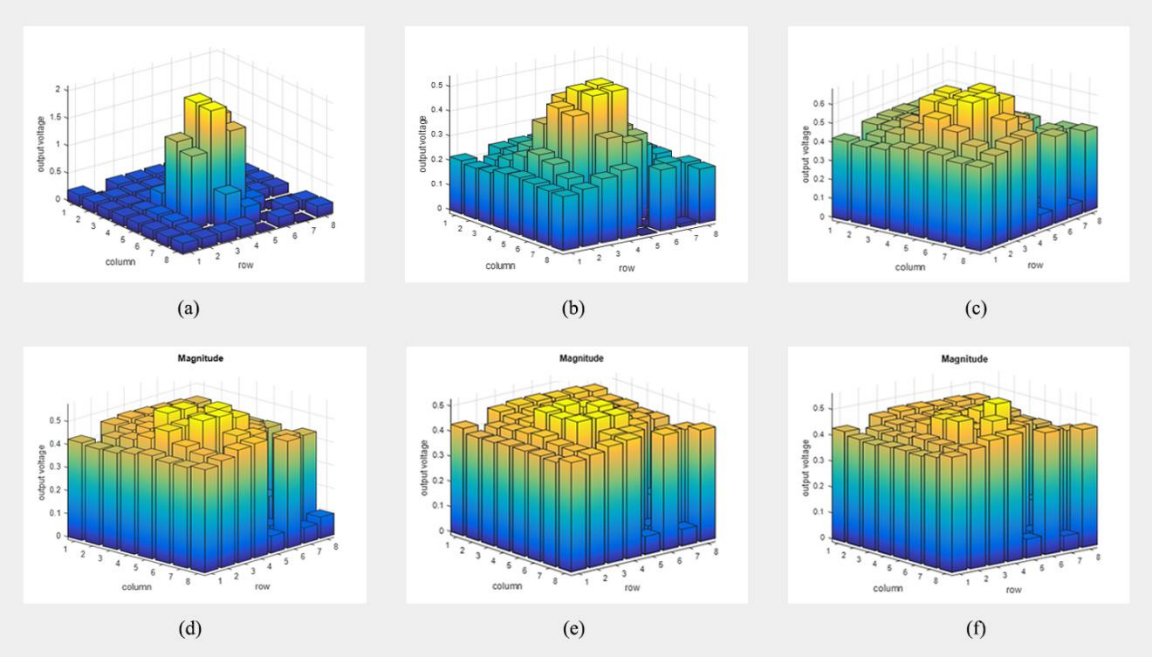

Figure 67: Electric field images of a full vial of distilled water elevated at increments of 1.25 cm from 0-6.25 cm (a-f respectively) above the imaging array.

Figure 67. The vial was completely filled with water and elevated in increments of 1.25 cm above the imaging array. The resulting electric field images,

Figure 67a-f, captures the fringing fields and shows how the peak becomes less prominent with distance, despite the overall charge and capacitance remaining the same.

9.10.1 Differing Dielectric Properties in Saline Solution

To see the effects of the differing dielectric constants in aqueous solutions, a side-by-side comparison was made with two plastic cups of water with different salinity concentrations. Prior research shows that there is an inverse relationship between the concentrations of salt-water solutions and their dielectric constant [78]. This happens because as the positive sodium and negative chloride ions dissociate, they generate an

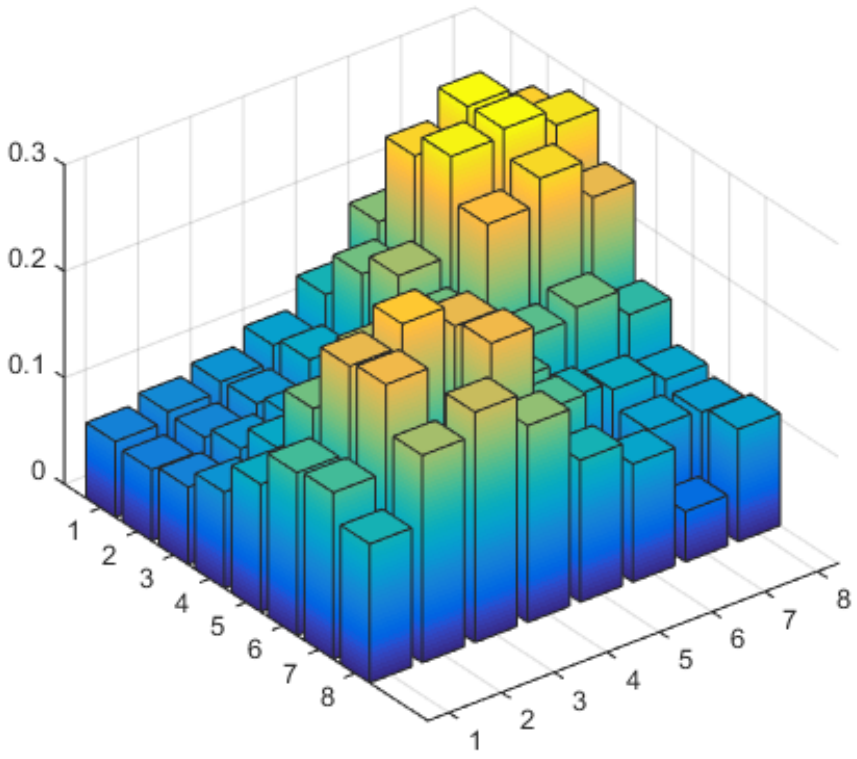

Figure 68: Electric field image of a plastic cup filled with water (upper-corner) and one of a salt-water solution (lower-corner).

electric field over a greater distance. The polar water molecules then orient themselves in a way that effectively cancels a large portion of the electric field. This "shielding" effect ultimately lowers the dielectric constant. When observing the resulting image, Figure 68, the salt-water solution did indeed exhibit a lower signal strength. This demonstrates the possibility of how electric field imaging can be used in fluid identification.

Chapter 10

INVERSE IMAGING PROBLEMS

The motive behind solving inverse imaging problems is to reconstruct an underlying original function using a collection of tangential measurements. An inverse problem normally requires that a solution exists, is unique (i.e. well-posed), and is stable [79]. Real applications, however, often violate these rules, particularly the uniqueness aspect. Several robust algorithms in the field of tomography overcome such obstacles. This chapter presents how these algorithms have been directly applied to the electric field imager. This system is the first non-contact, electric field-based solution in tomography.

10.1 Computed Tomography

Computed tomography (CT) is a procedure most prominently used in x-ray scans for medical imaging. The method takes projections at incremental angles around a target and combines the data to reconstruct an image of the object. Thus, a series of one-dimensional projections can reconstruct a two-dimensional image, and similarly two-dimensional images to a three-dimensional model.

Tomographic approaches first sparked interest after the results in the original active matrix two-dimensional PCB array. Since all of the pixels in a given column were simultaneously active, the board effectively became a 1 x N array of long parallel beams, much like x-ray beams in CT scans. CT was further extended with the development of the

active imaging method where electric fields could be used an alternative to x-rays, which are ionizing, can damage DNA, and can pose an increased risk for cancer [80], [81], [82].

10.2 Radon Transform

The forward projection in tomography, known as the Radon transform, is obtained by calculating the line integral of a function along the projection path. In two-dimensions, its mathematical depiction is

$$\begin{aligned} p_\theta\ r\ &= \int_{\theta,t\ line} f\ x,y\ \ ds \\ &= \int_{-\infty}^{\infty} f\ \boldsymbol{A}_\theta\ [\ r\quad s\ ]^T\ \ ds \\ &= \int_{-\infty}^{\infty} f(r\cos\ \theta\ - s\sin\ \theta\ , r\sin\ \theta\ + s\cos(\theta))\ ds \end{aligned} \qquad (10.1)$$

where $\boldsymbol{A}_\theta$ is the rotation matrix. Projections are made about an object with density $f(x,y)$ at every specified angle θ and displacement r, Figure 69. For x-rays, $f(x,y)$ is a function of the x-ray material attenuation properties the objects under test with respect to space. For electric fields, $f(x,y)$ is a function of the dielectric properties of the objects under test.

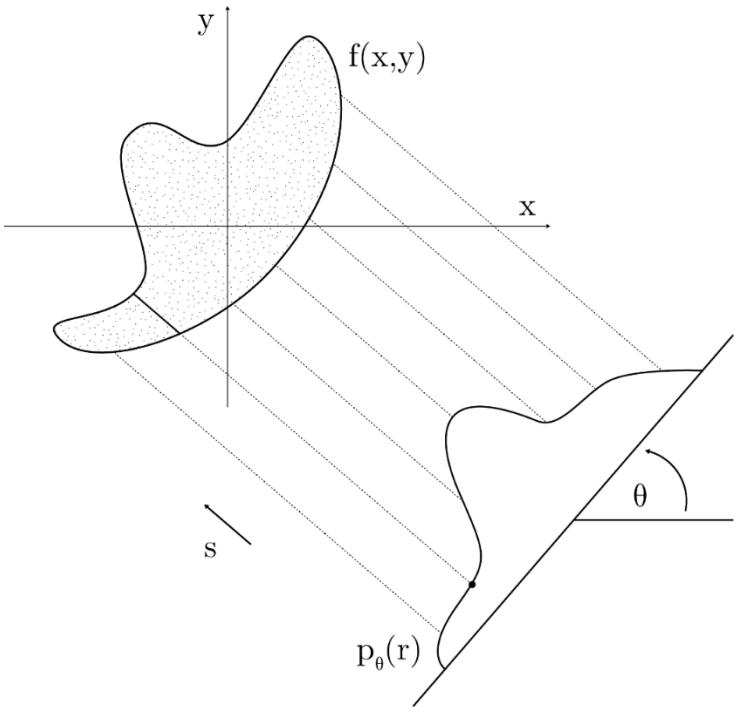

Figure 69: Diagram of the geometric representation of the Radon Transform.

10.3 Fourier Slice Theorem

The Fourier Slice Theorem provides the mathematical basis relating the Radon transform to image reconstruction. The theorem posits that the continuous time Fourier transform of a projection at angle θ

$$p_\theta\ \rho\ = \mathcal{F}\{p_\theta\ r\ \} \qquad (10.2)$$

and its corresponding path along the two-dimensional Fourier transform of the density function at angle θ

$$F\ u, v\ = \mathcal{F}_{x,y}\{f\ x, y\ \} \qquad (10.3)$$

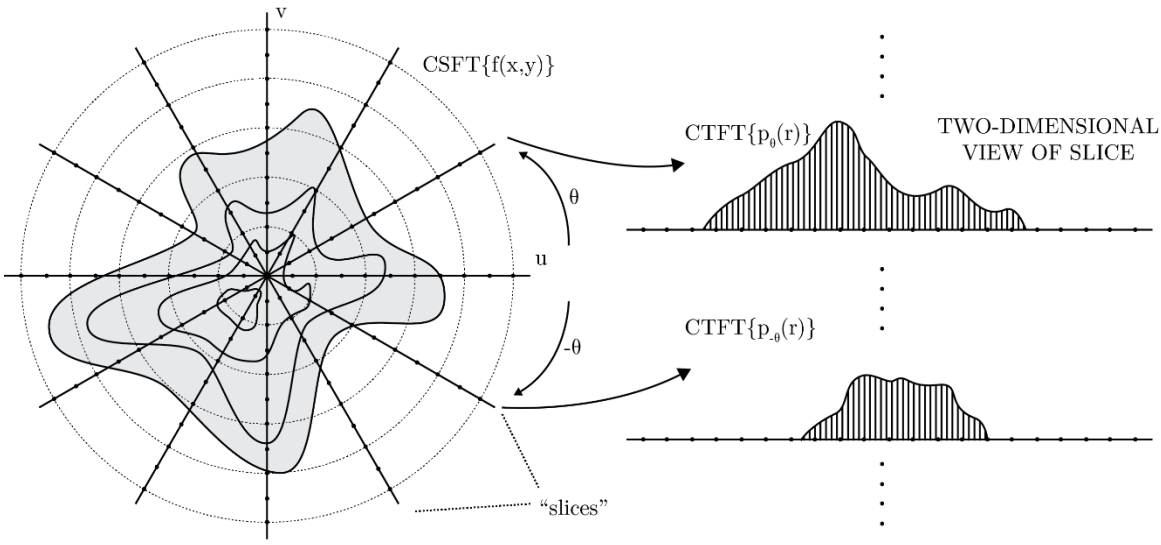

Figure 70: Geometric representation of the Fourier Slice Theorem.

are equal to one another:

$$P_\theta\ \rho\ = F\left(\rho\cos\ \theta\ , \rho\sin(\theta)\right) \qquad (10.4)$$

Figure 70 provides a visual representation of what the Fourier Slice Theorem geometrically implies. The projection of the two-dimensional Fourier transform can be thought of as a "slice," hence the name.

This rather non-intuitive conclusion can be verified with a summary of the following proof provided by Kak and Slaney [83]. First, we will make a transformation of the coordinate system to better suit the various rotations each slice is in as follows:

$$\begin{bmatrix} t \\ s \end{bmatrix} = \begin{bmatrix} \cos\theta & \sin\theta \\ -\sin\theta & \cos\theta \end{bmatrix} \begin{bmatrix} x \\ y \end{bmatrix} \qquad (10.5)$$

If the Fourier transform of a projection is made using this alternative coordinate system, we obtain the following:

$$
\begin{aligned}
S_\theta\ \omega\ &= \int_{-\infty}^{\infty} P_\theta\ t\ e^{-2\pi\omega t} dt \\
&= \int_{-\infty}^{\infty} \left[\int_{-\infty}^{\infty} f\ t, s\ ds \right] e^{-2\pi i\omega t} dt \\
&= \int_{-\infty}^{\infty} \int_{-\infty}^{\infty} f(t,s) e^{-2\pi\omega t} ds dt
\end{aligned}
\qquad (10.6)
$$

which is beginning to take the form of the two-dimensional spatial Fourier transform. By transforming the expression back to Cartesian coordinates, we obtain:

$$
\begin{aligned}
S_\theta\ \omega\ &= \int_{-\infty}^{\infty} \int_{-\infty}^{\infty} f\ x, y\ e^{-2\pi i\omega(x\cos\theta + y\sin\theta)} dx dy \\
&= F\ \omega, \theta\ = F(\omega\cos\theta, \omega\sin\theta)
\end{aligned}
\qquad (10.7)
$$

It can be seen how the Fourier transform of a projection is a slice of the two-dimensional Fourier transform of the original image. By the rotational property, with infinite rotations, we would obtain the full two-dimensional Fourier transform. An inverse Fourier function can then be applied to recover the original image.

10.4 Convolutional Back Projection

The convolutional back projection algorithm is a method of reconstruction made possible with the Fourier Slice Theorem. While it does reconstruct an image, it is the reverse projection, not the direct inverse. This is important because finding the inverse

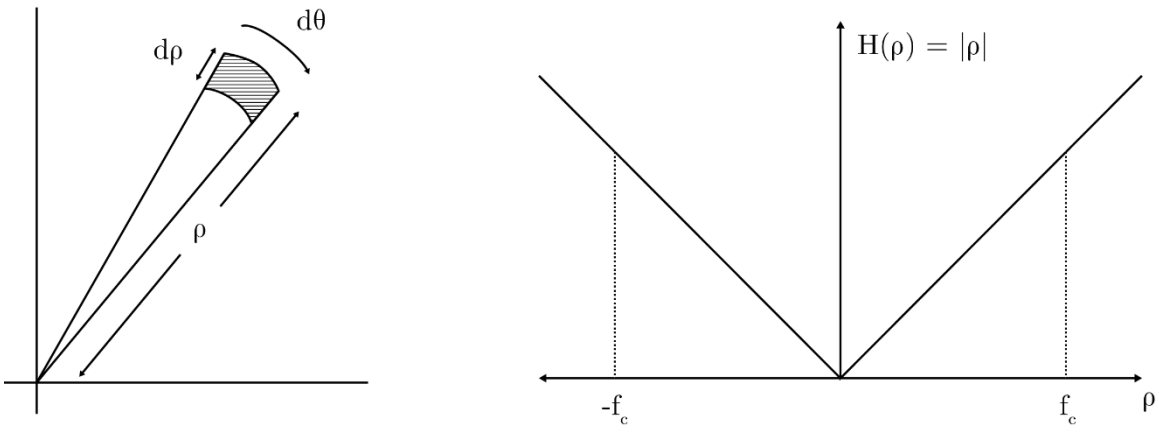

Figure 71: Visual explanation of the shape (left) of the Ram-Lak filter (right) used in convolutional backprojection.

Fourier transform of such large matrices, while also interpolating between polar and Cartesian coordinates, can prove to be very computationally expensive and impractical. At a high level, convolutional back projection takes a set of projections, applies a filter to the projections, and then uses back projection to recover the original image. The theory is as follows.

$$\begin{aligned} f\ x,y\ &= \int_{-\infty}^{\infty}\int_{-\infty}^{\infty} F\ u,v\ e^{2\pi j(xu+yv)}dudv \\ &= \int_{-\infty}^{\infty}\int_{0}^{\pi} P_\theta\ \rho\ e^{2\pi j(x\rho\cos\theta+y\rho\sin\theta)}|\rho|d\theta d\rho \\ &= \int_{0}^{\pi}\left[\int_{-\infty}^{\infty}|\rho|P_\theta\ \rho\ e^{2\pi j\rho(x\cos\theta+y\sin\theta)}d\rho\right]d\theta \end{aligned} \qquad (10.8)$$

Assuming the two-dimensional Fourier transform is given, to find the inverse in polar coordinates, the Jacobian of the polar coordinate transformation is used. This, in combination with the properties found in the Fourier Slice Theorem, allows the first and

second steps in Equation 10.8. With a simple rearrangement, we obtain the final result of Equation 10.8.

The rearrangement was done to more easily see the portion within the brackets which can be described as a function $g_\theta(t)$ where $t = x\cos\theta + y\sin\theta$. In this form, it is clear that $g_\theta(t)$ is simply the inverse continuous time Fourier transform of $|\rho|P_\theta(\rho)$:

$$\begin{aligned} g_\theta\ t\ &= \int_{-\infty}^{\infty} |\rho| P_\theta\ \rho\ e^{2\pi j\rho t} d\rho \\ &= CTFT^{-1}\{|\rho| P_\theta\ \rho\ \} \\ &= h\ t\ * p_\theta(r) \end{aligned} \qquad (10.9)$$

Here, $|\rho|$ acts as a high-pass filter, Figure 71. The further the radius, the greater the area for $d\theta d\rho$. This theoretically goes on infinitely, but for practicality, the response is bandlimited by some cutoff frequency, f_c. Knowing that the absolute value of the Jacobian is a high-pass filter and that multiplication in the frequency domain corresponds to convolution in the time domain, we obtain the final result of Equation 10.9. This finally yields the expression

$$f\ x, y\ = \int_0^{\pi} g_\theta(x\cos\theta + y\sin\theta) d\theta \qquad (10.10)$$

Therefore, for a given projection, the high-pass filter is applied. The filtered one-dimensional response is then "stretched" into two dimensions in accordance to its angle. This is repeated for all of the projections and the sum of the "stretched" responses will yield the original image.

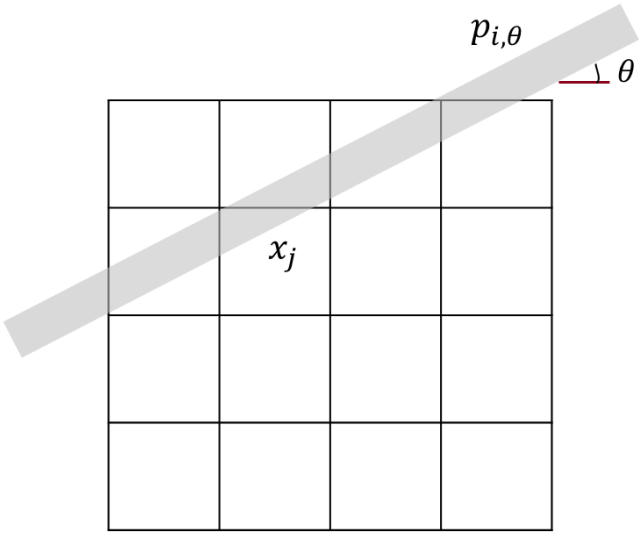

Figure 72: Discretization of a projection along pixels of the image space.

10.5 Algebraic Reconstruction

Backprojection, though not the direct Fourier inverse, is considered an analytical approach. In contrary, algebraic reconstruction discretizes an image into pixels which can be represented by a system of equations.

Any given projection $p_{i,\theta}$ will overlap with each pixel x_j with a certain weight w_{ij}, Figure 72. Therefore, the final scalar value for any projection in an image with N pixels is determined by

$$p_{i,\theta} = \sum_{j=1}^{N} w_{ij} x_j \qquad (10.11)$$

For all M projections, the measurement vector $p \in \mathbb{R}^M$ is defined by the system of equations

$$\boldsymbol{p} = W\boldsymbol{x} \qquad (10.12)$$

where $W \in \mathbb{R}^{MxN}$ is the projection matrix and $x \in \mathbb{R}^{N}$ is the unknown image to be reconstructed. Since the W matrix is often ill-posed, there is not an exact solution for x but rather a "best" solution can be obtained using convex optimization.

10.6 Sparsity Regularization

The "best" solution will be dependent on what frame, or norm, is used. The most common off-the-shelf method of optimization is least-squares, which utilizes the L2 norm. However, we know that many of the values in the matrices are zeros, so to exploit that sparsity, the L0 norm would be ideal. However, this proves to be computationally unrealistic, and we find that the L1 norm serves as a serviceable compromise.

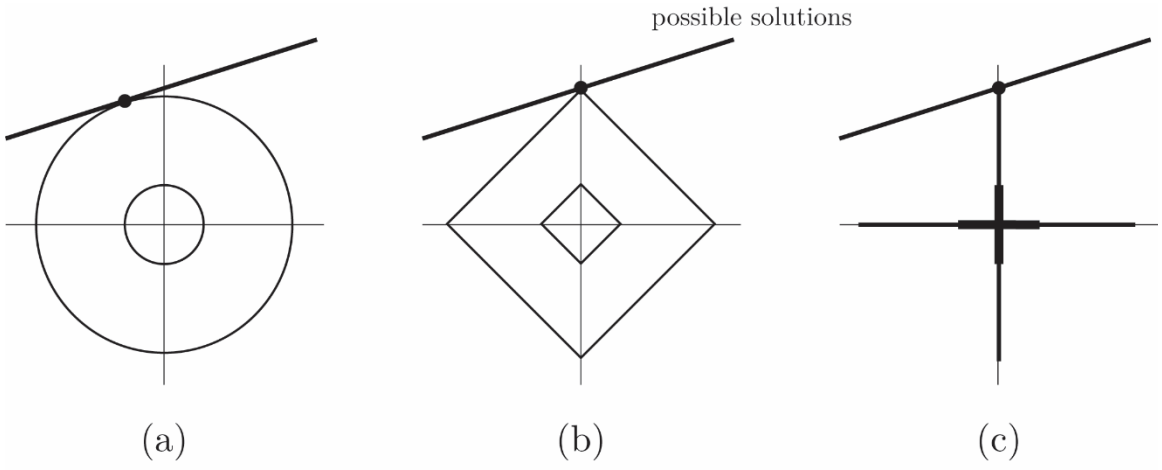

Figure 73: Visual representation of solutions obtained using the (a) L2, (b) L1, and (c) L0 norms. In this two-parameter example, the L2 solution is not sparse while the L1 and L0 solutions are sparse.

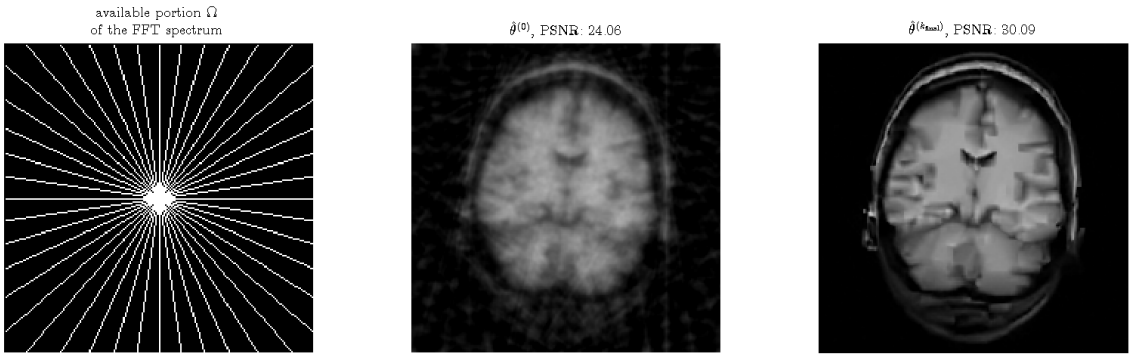

Figure 74: A computed tomography run of 22 projections with its frequency domain representation (left), a reconstruction using traditional means (middle), and a reconstruction using compressed sensing (right)

By enforcing a sparsity regularization term, CT has obtained reconstructions of equal, sometimes better, quality while using fewer measurements, Figure 74. The reduced number of projections needed will prove to be particularly valuable for the imaging system in its current form since measurements can be rather time consuming. The system enforcing sparsity regularization is simply

$$\begin{aligned} &\underset{x}{\text{minimize}} \quad \|x\|_1 \\ &\text{subject to} \quad \|Wx - p\|_2 < \sigma \end{aligned} \tag{10.13}$$

where σ is a term to accommodate non-zero noise levels.

10.7 Modified CT: Scaling Map Summation

An algorithm was developed in MATLAB to make CT computations specific to the board parameters including pad length, width, and pitch. Many aspects of this algorithm borrowed the computationally conserving method of convolution back projection. As a

first pass, an even simpler computation method was implemented in which just the pad projections (with no target) at each angle were summed on the image space. This creates a map of coefficients to scale the final image and correct for scaling offset.

The modified CT method greatly simplifies computation to simple summations which can be implemented on a peripheral interface controller (PIC) microcontroller while still being able to get reasonable images of electric fields. For the purpose of reconstructing a resemblance of the original image, it proved to be rather effective.

This algorithm was used to image an 'N' in both ideal and noisy conditions. First, simulations were run to determine the effect of high angular resolution with poor pad resolution, Figure 74, and were followed by the best-case scenario, Figure 75.

Even with very high angular resolution it was found that it was not sufficient to compensate for low pad resolution. Gaps between pads proved to particularly detrimental to image quality seen by the artifacts in the reconstruction and even the scaling coefficient map, Figure 74. Ideal simulations showed that for a given square aspect ratio, at least 32 divisions (if limited to powers of two to be consistent with typical display driver configurations) were necessary to produce images that could be reasonably recovered.

To demonstrate the algorithm is robust in noisy environments, the original images were buried in many layers of Gaussian noise, blurs, and gradients (simulating hotspots) to see if the 'N' shape could still be distinguished, Figure 77. A more practical medium pad/medium angular resolution combination was used for these simulations. The summing algorithm managed to perform admirably as it accurately reconstructs the noise but still manages to make the original image clearly detectable.

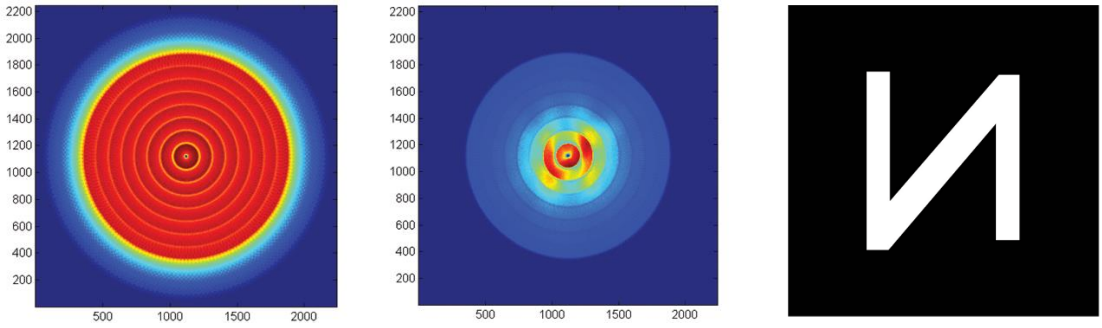

Figure 75: Scaling coefficient map (left), reconstructed image (middle), and original image (right) with low pad resolution and high angular resolution.

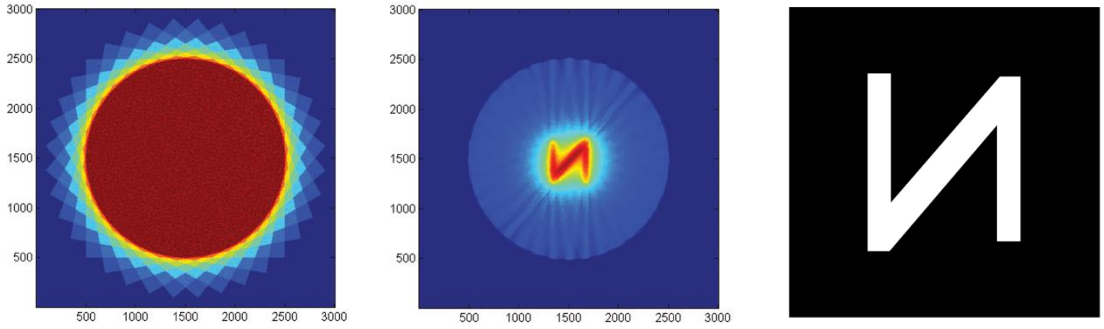

Figure 76: Scaling coefficient map (left), reconstructed image (middle), and original image (right) with high pad resolution and high angular resolution.

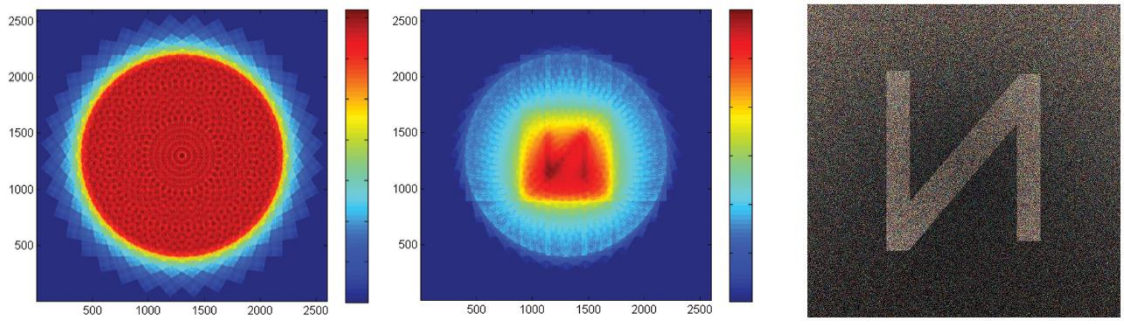

Figure 77: Scaling coefficient map (left), reconstructed image (middle), and very noisy original image (right) with high pad resolution and high angular resolution.

10.8 Analytic and Algebraic Reconstruction Results

The traditional tomography algorithms were implemented in MATLAB using the ASTRA toolbox [84], [85]. For faster computations, the CUDA platform was utilized on an NVIDIA Quadro 2000 through ASTRA [86]. The Sequential Parameter Optimization Toolbox (SPOT) [87] and the SPGL1 Toolbox [88], [89] were implemented in conjunction with ASTRA according to [90].

Projections were collected in ANSYS Maxwell simulating the parallel plate configuration in the active imaging setup in Chapter 9. Two orbs of water were placed in between the plates. The bodies of water were rotated at 10 degree increments about the center axis in which the electric flux density along the bottom plate was collected.

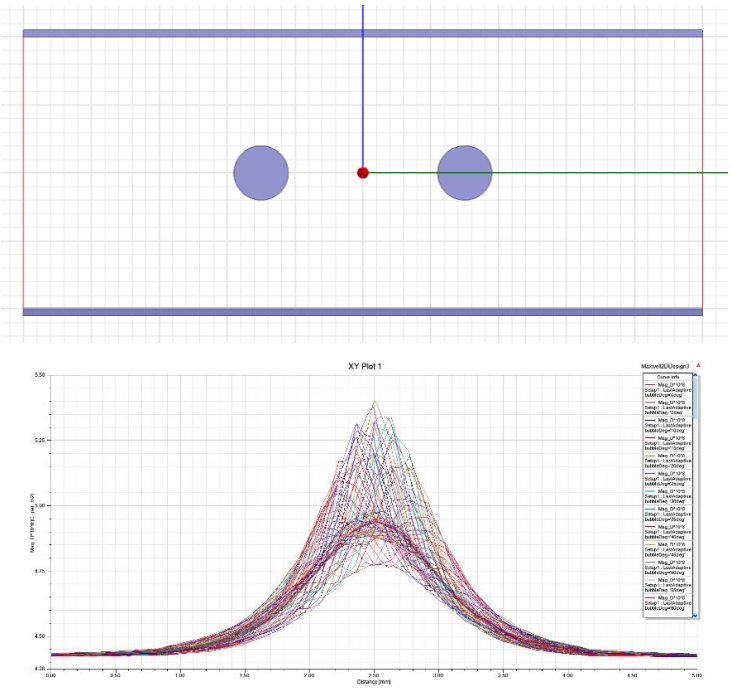

Figure 78: ANSYS model of two orbs of water rotated between two parallel plates (top) and the corresponding electric flux distributions along the bottom plate at 10 degree increments (bottom).

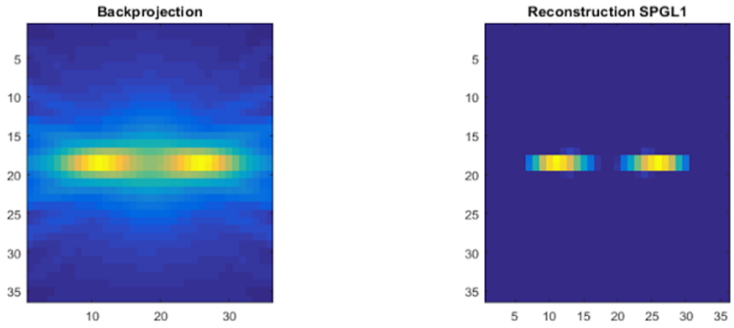

Figure 79: Electric field reconstructions of two orbs of water using backprojection (left) and sparsity enforcing L1 algebraic reconstruction (right).

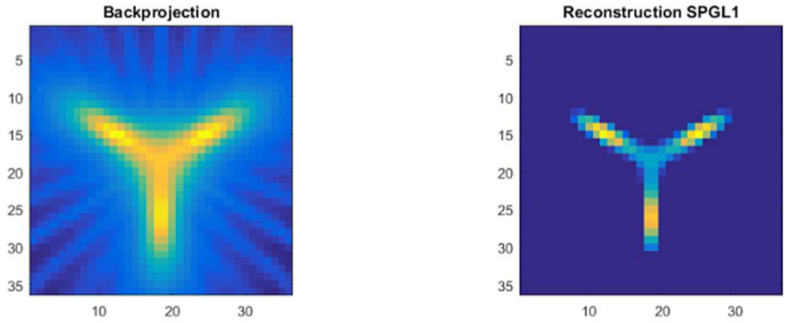

Figure 80: Electric field reconstructions of three orbs of water using backprojection (left) and sparsity enforcing L1 algebraic reconstruction (right).

The projection data was used to form a sinogram and served as the input to the CT algorithms. The backprojection analytical approach alongside an L1 regularization algebraic method were compared. The L1 sparsity regularization dramatically reduced noise in the reconstruction and gave better contrast to boundaries, Figure . The experiment was repeated with three orbs of water between the plates. Again, the L1 proved to significantly improve the image quality, Figure .

Aside from the benefit that higher quality images can be collected with fewer measurements, the sparsity method helps compensate for the fringing effects of the electric fields. While it does not completely remedy the fringing paths, it does remove a significant amount of noise and better pinpoints the locations of the objects under test.

Chapter 11

FUTURE WORK AND CONCLUSIONS

11.1 Review of Contributions

My major original contribution is a VLF electric field imaging system that uses an array of D-dot sensors to capture time-varying electric fields. It was realized in various forms including PCB and FLEX as well as one and two-dimensional arrays. It has reliably imaged concealed wires and sources of EMI.

The array provided the foundation for other imaging systems and contributions, such as the active imaging method. This method has demonstrated the ability to image objects beyond time-varying electric field sources including DC wires, floating wires, and dielectrics. It even allows for classification of objects of differing dielectric constants, e.g. distilled water vs. saline solution.

Active imaging was also used in inversion problems to reconstruct higher-dimensional images using a series of lower-dimensional projections. This provided a novel, safe alternative to non-invasive imaging by using electric fields in a non-contact form factor.

The imaging system was predicated on the work characterizing electric field noise capacitively coupling into a D-dot-based electric field sensing system. This work gave insight into optimizing the D-dot sensor for performance.

11.2 Future Work

The imaging system itself can undergo specification improvements in future generations, making not only performance improvements but also serve as a platform for other applications. Such possibilities will be given some context.

11.2.1 Greater Specifications

The current imager has a pixel size of 1 cm^2. This yields for a rather coarse image, making ways to improve the resolution one of the most obvious improvements to strive for. The pixel size is currently limited by the size of the operational amplifier as well as the trade-off between sensor head area and signal strength. Alternative architectures may be explored to sufficiently reduce the leakage current and forgo the need for dedicated amplifiers. Sensor head design may also need to be explored to improve signal strength such as a corrugated surface to increase surface area for a given footprint.

Speed is another aspect the imager can improve in seeing how the ultimate goal is for the system to operate in real-time. This could be addressed with lower-quality sensory data collection (e.g. lowering the time constant on the lock-in amplifier) compensated with post-processing techniques. It is also possible to pipeline the readout by connecting several outputs to read channels in parallel.

More components can be integrated directly into the imaging board for a more portable and possible lower-cost unit. For example, boards have already been designed with the multiplexing unit built in. This eliminates the need for the large and expensive

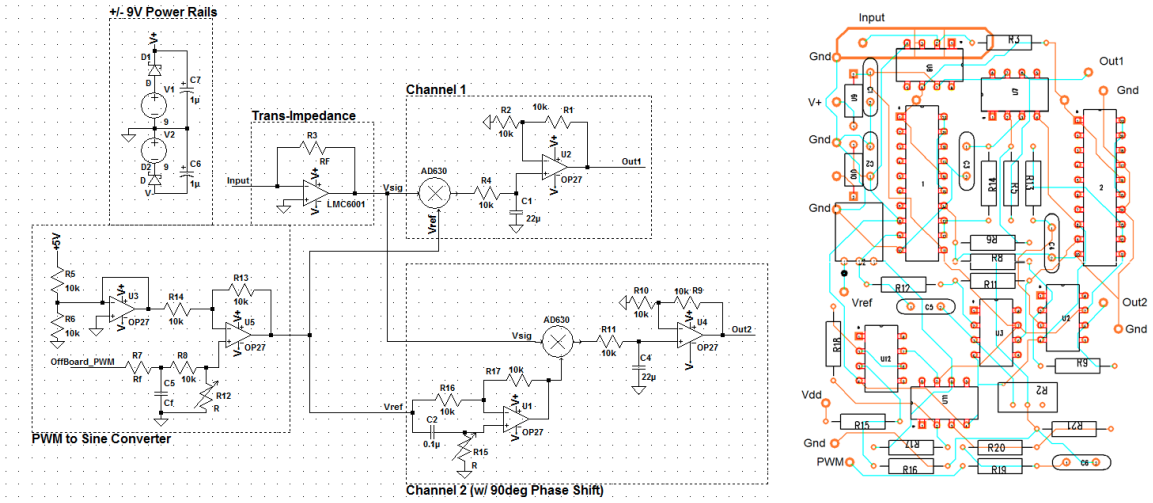

Figure 79: Schematic (left) and PCB layout (right) of a portable lock-in amplifier built with COTS components. This circuit was designed by my colleagues Jake Sciacca, Weidong Ye, Sandeep Vora, and Kegan Scowen in fulfillment of their 2015 senior capstone.

Agilent Switch/Measure Unit [57]. This can be taken a step further with a custom lock-in amplifier. One has already been assembled using COTS and has proven to fare well in performance for VLF measurements, even when compared to high-end commercial lock-in amplifiers.

11.2.2 Improved Software

As alluded to, improvements in software can help improve the accuracy of our devices as well as help make the boards run more efficiently. Post-processing will allow an extraction information from noisy signals, allowing for greater leniency on the hardware specifications. It will also allow for targeted and optimized performance for a given application. Software is also key in improving the speed of automation, a feature that will be critical if pixel resolution does improve. This will sometimes manifest in the form of

drives, which have already been written in the automation efforts and have dramatically reduced measurement times. There is still much room for improvement, however, as the current approach is very iterative rather than parallel. Drivers can also dynamically optimize parameters such as measurement times and lag times which are currently conservatively hardcoded.

11.2.3 Tomography

The next logical step in obtaining real-world electric field tomography results is to create a higher resolution array. Steps were already made in the form of a dense one-dimensional array. For the sake of continuity and limiting the number of alternate components, the imager was again fabricated in the form of a four-layer PCB in which one of the intermediary layers was a ground plane. It should be noted that the green film seen on the imager is a solder screen.

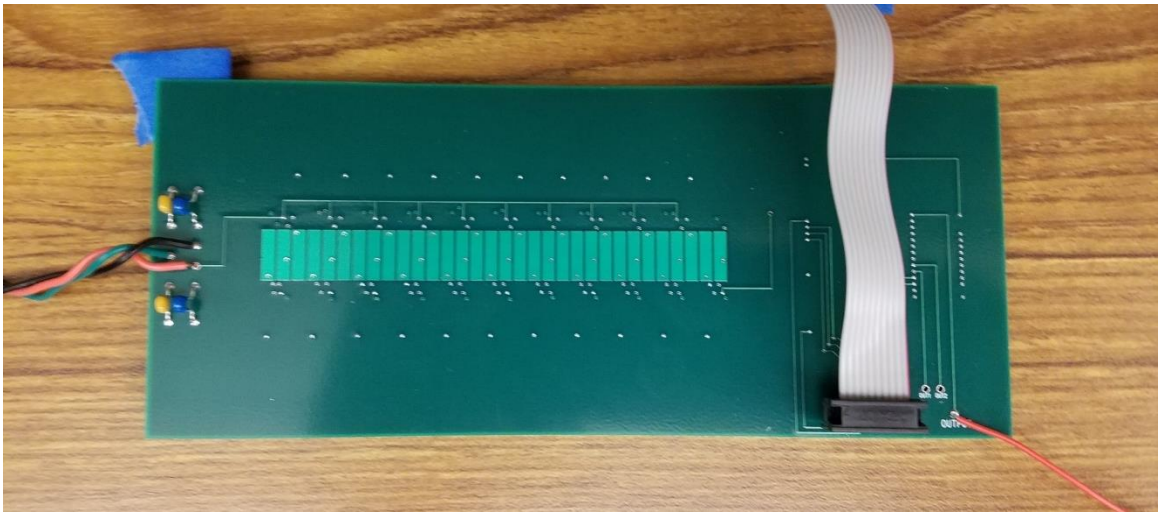

Figure 80: Photo of the dense 1 x 32 array of D-dot sensors with three 16 bit MUXs integrated into the board.

The LMC 6081 amplifier [62] was utilized again and laid out on the bottom layer. In order to employ the same design philosophy as the fully two-dimensional array, each sensor head would need a dedicated amplifier. However, the amplifiers were already nearly packed as densely as possible. By moving down to a one-dimensional array, we were capable of fitting more pixels for a given length by staggering the amplifiers along the row, Figure 82.

Furthermore, the multiplexer was directly integrated into this board in the form of the CD4067B MUX [91], eliminating the need to use the large and bulky Agilent bench multiplexing system as well as decreasing the time needed to conduct measurements. The multiplexer can be controlled using an Arduino Uno, the code for which was integrated into the MATLAB automation software.

Image quality can further be improved, in simulation and real-world, by exploring other sparsity enforcing reconstruction algorithms. A Laplacian finite element model can also be developed and used to more directly compensate the fringing effects.

11.2.4 Future Applications

The electric field imager presented in this dissertation opens a new realm of applications. This goes far beyond the grand goals mentioned in this dissertation including tomography for medical imaging, non-invasive security, EMI imaging, and power load monitoring. For example, with electric fields having such a close relationship with magnetic fields, magnetic field measurements can greatly complement the electric field

imager. With the utilization of such fields becoming more and more integral in our daily lives, it is not hard to imagine that we have only begun to scratch the surface.

REFERENCES

[1] C. S. Spiegel, "Global Electronics: High-Growth Products and New Markets," BCC Research, Wellesley, MA, 2007.

[2] Transparency Market Research, "Consumer Electronics (Television, Handheld Devices, Personal Computers, Cameras and Camcorders, Audio/Video Devices, Personal Care Products, Gaming Consoles) Market - Global Industry Analysis, Size, Share, Growth, Trends and Forecast 2014 - 2022," Transparency Market Research, Albany, NY, 2015.

[3] IC Insights, "Integrated Circuit Market Drivers," IC Insights, Scottsdale, AZ, 2013.

[4] D. Taylor, "Measuring techniques for electrostatics," *Journal of Electrostatics,* Vols. 51-52, pp. 502-508, 2001.

[5] T. Zimmerman, J. Smith, J. Paradiso, D. Allport and N. Gershenfeld, "Applying electric field sensing to human-computer interfaces," in *Proceedings of the SIGCHI Conference on Human Favtors in Computer Systems*, Denver, CO, 1995.

[6] J. Smith, "Electric Field Imaging," Ph.D. Thesis, Massachusetts Institute of Technology, Cambridge, MA, 1999.

[7] J. Smith, E. Garcia, R. Wistort and D. Krishnamoorthy, "Electric field imaging pretouch for robotic graspers," in *Proceedings of the IEEE/RSJ Intl. Conference on Intelligent Robots and Systems*, San Diego, CA, Oct. 2007.

[8] W. Heiligenberg, "Electrolocation and jamming avoidance in the electric fish Gymnarchus niloticus (Gymnarchidae, Mormyriformes)," *J. Comp. Physiol.,* vol. 103, no. 1, pp. 55-67, 1975.

[9] B. Brown, J. Hutchison, M. Hughes, D. Kellogg and R. Murray, "Electrical characterization of gel collected from shark electrosensors," *Phys. Rev. E*, vol. 65, no. 6, pp. 061903-1-5, June 2002.

[10] B. Brown, "Modeling an electrosensory landscape," *Journal of Experimental Biology*, vol. 205, no. 7, pp. 999-1007, 2002.

[11] J. Stanley and C. White, "Electric field sensing air bag danger zone sensor". United States of America Patent US5964478 A, 12 Oct 1999.

[12] B. Mayton, L. LeGrand and J. Smith, "Robot, feed thyself: Plugging in to unmodified electrical outlets by sensing emitted AC electric fields," in *IEEE Intl. Conference on Robotics and Auotmation*, Anchorage, AK, May, 2010.

[13] T. Zimmerman, J. Smith, J. Paradiso, D. Allport and G. Neil, "Applying electric field sensing to human-computer interfaces," in *Conference on Human Factors in Computing Systems - Proceedings*, Denver, CO, 1995.

[14] J. Smith, T. White, C. Dodge, J. Paradiso, N. Gershenfeld and D. Allport, "Electric field sensing for graphical interfaces," *IEEE Computer Graphics and Applications*, vol. 18, no. 3, pp. 54-60, June, 1998.

[15] Touch Technology Division, "Proximity Design Guide," Atmel Corporation, San Jose, CA, 2012.

[16] D. Wang, "Basics of Capacitive Sensing and Applications," Texas Instruments Inc., Dallas, TX, 2014.

[17] S. Bhat, "Salinity (Conductivity) Sensor Based on Parallel Plate Capacitors," University of South Florida, Tampa, FL, 2005.

[18] K. Greene, "Robots that sense before they touch," MIT Technology Review, 17 September 2007. [Online]. Available: https://www.technologyreview.com/s/408680/robots-that-sense-before-they-touch/.

[19] R. Harikumar, R. Prabu and S. Raghavan, "Electrical impedance tomography (EIT) and its medical applications: a review," *International Journal of Soft Computing Engineering*, vol. 3, no. 4, pp. 193-198, September, 2013.

[20] T. Sullivan, S. Deiss and G. Cauwenberghs, "A low-noise, non-contact EEG/ECG sensor," in *Biomedical Circuits and Systems Conference, IEEE 2007*, Montreal, QC, Canada, November, 2007.

[21] W. Telford, L. Geldart and R. Sheriff, Applied Geophysics, 2 ed., Cambridge, UK: Cambridge University Press, October 1990.

[22] B. Carlson and U. Inan, "A novel technique for remote sensing of thunderstorm electric fields via Kerr effect and sky polarization," *Geophysical Research Letters*, vol. 35, no. 22, p. 22806, November 2008.

[23] H. Jones, F. Boudreaux and W. Woodruff, "Quasi-static electric field studies of thunderstorms," *Journal of Geophysical Research,* vol. 75, no. 7, p. 1966, 1960.

[24] O. Zolotov, "Ionosphere quasistatic electric fields disturbances over seismically active regions as inferred from satellite-based observations: A review," *Russ. J. Phys. Chem. B,* vol. 9, no. 5, pp. 785-788, 2015.

[25] M. Gousheva, D. Danov, P. Hristov and M. Matova, "Quasi-static electric fields phenomena in the ionosphere associated with pre- and post earthquake effects," *Natural Hazards and Earth System Sciences,* vol. 8, pp. 101-107, 2007.

[26] M. Kamogawa, J. Liu, H. Fujiwara, Y. Chuo, Y. Tsai, K. Hattori, T. Nagao, S. Uyeda and Y. Ohtsuki, "Atmospheric field variations before the March 31, 2002 m6.8 earthquake in Taiwan," *Terr. Atmospheric Ocean, Sci,* vol. 15, no. 3, pp. 397-412, September 2004.

[27] S. Schultz, R. Selfridge, S. Chadderdon, D. Perry and N. Stan, "Non-intrusive electric field sensing," in *Proceedings of SPIE - The Intl. Society for Optical Eng.*, San Diego, CA, 2014.

[28] A. Estes, A. Abad-Santos and M. Sullivan, "Explosions at Boston Marathon kill 3 - now, a 'potential terrorist investigation'," *The Wire*, 15 April 2013.

[29] H. Chung, W. Ye, S. Vora, S. Rednour and D. Allee, "A passive very low-frequency (VLF) electric field imager," *IEEE Sensors,* vol. 16, no. 9, pp. 3181-3187, 1 May 2016.

[30] Langley Research Center, "Electric Field Quantitative Measurement System and Method," NASA Tech Briefs, 1 January 2017. [Online]. Available: http://www.techbriefs.com/component/content/article/ntb/tech-briefs/electronics-and-computers/26139.

[31] American Cancer Society, "Do x-rays and gamma rays cause cancer?," 24 February 2015. [Online]. Available: https://www.cancer.org/cancer/cancer-causes/radiation-exposure/x-rays-gamma-rays/do-xrays-and-gamma-rays-cause-cancer.html.

[32] T. Sudo, H. Sasaki, N. Masuda and J. Drewniak, "Electromagnetic interference (EMI) of system-on-package (SoP)," *IEEE Transactions on Advanced Packaging,* vol. 27, no. 2, pp. 304-314, May 2004.

[33] X. Li, V. Inclan, G. Rowe and A. Mamishev, "Parametric modeling of concentric fringing electric field sensors," in *Annual Report Conference on Electrical Insulation and Dielectric Phenomena, IEEE,* Ann Arbor, MI, October 2005.

[34] S. Ghionea, G. Smith, J. Pulskamp, S. Bedair, C. Meyer and D. Hull, "MEMS electric-field sensor with lead zirconate titanate (PZT)-actuated electrodes," in *Sensors, 2013 IEEE*, Baltimore, MD, November 2013.

[35] Z. Zhang, L. Li, X. Xie, D. Xiao and W. He, "Optimization design and research character of the passive electric field sensor," *IEEE Sensors,* vol. 14, no. 2, pp. 508-513, February 2014.

[36] H. Chung, *Radiation Detection and Imaging: Neutrons and Electric Fields,* Master's Thesis, Arizona State University, 2015.

[37] S. Heintzelman and D. Hull, "Characterization and analysis of electric-field sensors," in *2015 IEEE Industry Applications Society Annual Meeting*, Addison, TX, 2015.

[38] C. Browning, S. Vinci, J. Zhu, D. Hull and M. Noras, "An evaluation of electric-field sensors for projectile detection," in *2013 IEEE Sensors*, Baltimore, MD, 2013.

[39] D. Hull and S. Vinci, "Passive aircraft detection and noncooperative helicopter identification using extremely low frequency (ELF) electric field sensors," in *Law Enforcement and Physical Security Symposium*, Boston, MA, 1998.

[40] B. Rhoades, S. Ramsey and M. Noras, "A novel electric-field sensor for projectile detection," in *Proc. 2012 Joint Electrostatics Conference*, Cambridge, Canada, 2012.

[41] E. Generazio, "Electric Potential and Electric Field Imaging with Applications," *Materials Evaluation,* vol. 73, no. 11, pp. 1479-1489, November 2015.

[42] International Telecommunications Union - Radiocommunication Sector, "Nomenclature of the frequency and wavelength bands used in telecommunications," International Telecommunications Union, Geneva, SUI, 2015.

[43] International Telecommunications Union, "Radio Regulations," International Telecommunications Union, Geneva, SUI, 2012.

[44] A. Tronson, "Single chip VLF magnetic field receiver," Stanford University, Palo Alto, CA, May 2014.

[45] C. Altgelt, "The world's largest "radio" station," U.S. Navy, Tech. Rep., 2005.

[46] J. Tyson, "How Metal Detectors Work," How Stuff Works, 23 May 2001. [Online]. Available: http://electronics.howstuffworks.com/gadgets/other-gadgets/metal-detector.htm.

[47] International Electrotechnical Commission, "World Plugs," [Online]. Available: http://www.iec.ch/worldplugs/. [Accessed April 2017].

[48] R. Fano, L. Chu and R. Adler, Electromagnetic Fields, Energy, and Forces, New York, USA: John Wiley and Sons, 1960.

[49] S. Frei, R. Jobava, D. Karkashadze, A. Gheonjian and E. Yavolovskaya, "Calculation of low frequency EMC problems in large systems with a quasi-static approach," in *International Symposium on Electromagnetic Compatibility*, Silicon Valley, CA, 2004.

[50] P. Sandbord, D. Hull and S. Vinci, "Distortion of sensed electric field by conducting sensor platforms," in *Digests of the 2010 14th Biennial IEEE Conference on Electromagnetic Field Computation*, Chicago, IL, 2010.

[51] M. Sallin and B. Daout, "Derivative time-domain sensor and fibre optic correction factor calculation," Montena Technology, Rossens, SUI.

[52] S. Vinci, J. Zhu and D. Hull, "Analysis of electrostatic charge on small-arms projectiles," in *Proc. SPIE, Active and Passive Signatures*, Anchorage AK, May 2012.

[53] Krohn-Hite Corporation, *Ultra-Pure Sinewave Oscillator*, 2003.

[54] Femto, *Variable Gain Low Noise Current Amplifier*, 2014.

[55] J. Zimmerman, "SQUID instruments and shielding for low-level magnetic measurements," *Journal of Applied Physics*, vol. 48, no. 2, pp. 702-710, 1977.

[56] Agilent Technologies, *80 MHz Function/Arbitrary Waveform Generator*, 2000.

[57] Agilent Technologies, *Multifunction Switch/Measure Unit,* 7.

[58] Stanford Research Systems, *DSP Lock-in Amplifier,* 2011.

[59] G. Karady and K. Holbert, Electrical Energy Conversion and Transport, 2nd ed., Hoboken, NJ: Wiley-IEEE Press, 2013.

[60] Texas Instruments, *N-Channel FemtoFET MOSFET,* 2014.

[61] D. August, *Memory Technology,* Princeton University, 2015.

[62] Texas Instruments, *Ultra, Ultra-Low Input Current Amplifier,* September 2015.

[63] G. Raupp, "Flexible Display Center at Arizona State University: A Unique Industry-Government-Academic Partnership for Creating Revolutionary Information Display Technology," in *2008 17th Biennial University/Government/Industry Micro/Nano Symposium*, Louisville, KY, 2008.

[64] J. Smith, B. Katchman, Y. Lee, B. O'Brien, E. Bawolek, S. Shah and J. Blain-Christen, "Disposable point-of-use optical biosensor for multiple biomarker detection," in *2014 IEEE Biomedical Circuits and Systems Conference (BioCAS) Proceedings*, Lausanne, 2014.

[65] R. Street, J. Lu, J. Bert, M. Strnad and L. Antonuk, "TFT backplane technologies for advanced array applications," in *2015 IEEE International Electron Devices Meeting (IEDM)*, Washington, DC, 2015.

[66] J. Smith, A. Couture, J. Stowell and D. Allee, "Optically Seamless Flexible Electronic Tiles for Ultra Large-Area Digital X-Ray Imaging," *IEEE Transactions on Components, Packaging and Manufacturing Technology,* vol. 4, no. 6, pp. 1109-1115, June 2014.

[67] E. Lee, A. Indluru, D. Allee, L. Clark, K. Holbert and T. Alford, "Effects of Gamma Irradiation and Electrical Stress on a-Si:H Thin-Film Transistors for Flexible Electronics and Displays," *Journal of Display Technology,* vol. 7, no. 6, pp. 325-329, June 2011.

[68] G. Kunnen, J. Smith, H. Chung and D. Allee, "TFT-based multi-stage, active pixel sensor for alpha particle detection," *Institution of Engineering and Technology Electronics Letters,* vol. 93, no. 13, pp. 705-706, September 2008.

[69] J. Smith, A. Couture and D. Allee, "Charge emission induced transient leakage currents of a-Si:H and IGZO TFTs on flexible plastic substrates," *Electronics Letters,* vol. 50, no. 2, pp. 105-106, January 2014.

[70] J. Smith, E. Forsythe, D. Allee and J. Blain-Christen, "Adaptive digital x-ray detector for high sensitivity medical fluoroscopy imaging," in *2015 IEEE Biomedical Circuits and Systems Conference (BioCAS),* Atlanta, GA, 2015.

[71] D. Allee and et al., "Circuit-Level Impact of a-Si:H Thin-Film-Transistor Degradation Effects," *IEEE Transactions on Electron Devices,* vol. 56, no. 6, pp. 1166-1176, June 2009.

[72] M. Marrs and et al., "Control of Threshold Voltage and Saturation Mobility Using Dual-Active-Layer Device Based on Amorphous Mixed Metal–Oxide–Semiconductor on Flexible Plastic Substrates," *IEEE Transactions on Electron Devices,* vol. 58, no. 10, pp. 3428-3434, October 2011.

[73] K. Kaftanoglu and et al., "Stability of IZO and a-Si:H TFTs Processed at Low Temperature (200 C)," *Journal of Display Technology,* vol. 7, no. 6, pp. 339-343, June 2011.

[74] Texas Instruments, *Simple Switcher 3-A Step-Down Voltage Regulator,* May 2016.

[75] Texas Instruments, *Precision CMOS Single Operational Amplifier,* March 2013.

[76] B. Zhang, W. Wang, J. He, R. Zeng and H. Yin, "Calibration of field-mill instrument for measuring DC electric field," in *2012 International Conference on High Voltage Engineering and Application,* Shanghai, 2012.

[77] "Electric field mill," [Online]. Available: http://a-tech.net/ElectricFieldMill/. [Accessed 15 3 2014].

[78] J. Hasted, D. Ritson and C. Collie, "Dielectric Properties of Aqueous Ionic Solutions. Parts I and II," *Journal of Chemical Physics,* vol. 16, no. 1, 1948.

[79] V. Isakov, "Inverse Source Problems (Mathematical Surveys and Monographs)," American Mathematical Society, 1990.

[80] S. Boodman, "Should you worry about the radiation from CT scans?," *The Washington Post,* 4 January 2016.

[81] National Cancer Institute, "Computed Tomography (CT) Scans and Cancer," 16 July 2013. [Online]. Available: https://www.cancer.gov/about-cancer/diagnosis-staging/ct-scans-fact-sheet.

[82] Food and Drug Administration, "What are the Radiation Risks from CT?," 2 February 2017. [Online]. Available: https://www.fda.gov/Radiation-EmittingProducts/RadiationEmittingProductsandProcedures/MedicalImaging/MedicalX-Rays/ucm115329.htm.

[83] A. Kak and M. Slaney, "Principles of Computerized Tomography Imaging (classics in Applied Mathematics).," Society for Inustrial and Applied Mathematics, 2001.

[84] W. Van Aarle, W. Palenstijn, J. Cant, E. Janssens, F. Bleichrodt, A. Dabravolski, J. De Beenhouwer, K. Batenburg and J. Sijbers, "Fast and Flexible X-ray Tomography Using the ASTRA Toolbox," *Optics Express,* vol. 24, no. 22, pp. 25129-25147, 2016.

[85] W. Van Aarle, W. Palenstijn, J. De Beenhouwer, T. Altantzis, S. Bals, K. Batenburg and J. Sijbers, "The ASTRA Toolbox: A platform for advanced algorithm development in electron tomography," *Ultramicroscopy,* vol. 157, pp. 35-47, 2015.

[86] W. Palenstijn, K. Batenburg and J. Sijbers, "Performance improvements for iterative electron tomography reconstruction using graphics processing units (GPUs)," *Journal of Structural Biology,* vol. 176, no. 2, pp. 250-253, 2011.

[87] E. Van den Berg and M. Friedlanger, "Spot - A Linear-Operator Toolbox," 2014.

[88] E. Van den Berg and M. Friedlander, "Probing the Pareto frontier for basis pursuit solutions," *SIAM Journal on Scientific Computing,* vol. 31, no. 2, pp. 890-912, 2008.

[89] E. Van den Berg and M. Friedlander, *SPGL1: A solver for large-scale sparse reconstruction,* 2007.

[90] F. Bleichrodt, T. van Leeuwen, W. Palenstijn, W. van Aarle, J. Sijbers and K. Batenburg, "Easy implementation of advanced tomography algorithms using the ASTRA toolbox with Spot operators," *Numerical Algorithms,* vol. 71, no. 3, pp. 673-607, 2016.

[91] Texas Instruments, *CMOS Analog Multiplexers/Demultiplexers,* June 2003.